10-2-2015

Design, Synthesis and Applications of Layered Double Hydroxides (LDHs), Mixed Metal Oxides (MMOs) and Nanocomposites as Efficient Sorbents and Multi-Functional Catalysts

Madhavi N. Pahalagedara
University of Connecticut - Storrs, madhavi.pahalagedara@uconn.edu

Design, Synthesis and Applications of Layered Double Hydroxides (LDHs), Mixed Metal Oxides (MMOs) and Nanocomposites as Efficient Sorbents and Multi-Functional Catalysts

Madhavi Nirmani Pahalagedara, Ph. D

University of Connecticut, 2015

The research work presented here is focused on designing new synthetic techniques for LDHs, MMOs and nanocomposites for better control over surface area, particle size, morphology and catalytic activity as compared to conventional techniques. Materials synthesized via these methods were thoroughly characterized and used in various model chemical reactions. This thesis is delineated into three parts.

The first part describes the synthesis of ordered mesoporous NiAl mixed metal oxides (MMOs) from NiAl layered double hydroxides (LDHs) through a soft template method using pluronic-F127 as the structure directing agent. Ordered mesopores were obtained by the thermal decomposition of as-synthesized LDHs at different temperatures. The effects of the pluronic-F127 amount and the calcination temperature on the pore size distribution of the MMO were investigated. NiAl MMOs exhibited excellent catalytic activities in the Knoevenagel condensation of benzaldehyde with acidic methylene group-

containing malononitrile. Finally, the dependence of catalytic activity on the surface properties of NiAl MMOs was investigated. The pore diameter and the pore volume of NiAl MMOs were well correlated with catalytic performance of the catalysts. MMO obtained from the calcination of NiAl-F127$_{3\%}$LDH at 750˚C for 5 hours gave the highest conversion (> 99%) in the Knoevenagel condensation in 30 minutes. Optimum pore diameter for the model reaction described here was 7.7 nm, which gave rise to more than 99% conversion with 100% selectivity. Ethanol gave the best conversion at 60˚C. The regenerated catalyst showed 93.0%, and 89.0% of the initial catalytic activity after the first and the second regeneration cycles, respectively.

In the second part, a sonochemical method was employed in the synthesis of nickel aluminum layered double hydroxides (NiAl-LDH) and the materials were used as adsorbents for the removal of the reactive azo dye, Remazol Brilliant Violet (RBV-5r). The experimental data obtained for microstructure were compared and both the arrangement and orientation of the intercalated dye species were examined using Molecular dynamics (MD) simulations. The obtained materials were characterized by X-ray diffraction (XRD), nitrogen sorption (BET), scanning electron microscopy (SEM), transmission electron microscopy (TEM), thermogravimetric analysis (TGA) and Fourier transformation infrared spectroscopy (FTIR). The adsorption characteristics were studied in a batch process by optimizing different parameters such as calcination temperature, contact time, initial dye concentration, solution pH, and solution temperature. NiAl-LDH material synthesized by sonochemical (SC) methods and

calcined at 250˚C (NiAl-C250SC) showed the best dye removal efficiency (100% removal in 6 minutes) with an adsorption capacity of 150 mg/g at 25˚C and at pH=6. The reusability of the dye loaded material was investigated by replicating the adsorption-desorption cycle. The results show that the material could be regenerated without significant loss of the adsorption capacity. The regenerated adsorbent showed 95.9%, and 95.7% of the initial adsorption capacity after the first and the second regeneration cycles, respectively. XRD and FTIR results for LDH before and after the dye adsorption showed that removal of the dye is due to intercalation of the organic dye molecule into the LDH structure where a net increase in the basal spacing from 7.48 Å to 8.71 Å is observed. Molecular dynamics (MD) simulations further suggest that the dye molecules arrange in the interlayer space as a monolayer with the main axis horizontal to the layer plane. The calculated d-spacing values were in good agreement with the experimental results.

The third part demonstrates the synthesis of activated carbon templated Copper Aluminum mixed oxide (CuAl MO) catalysts for the direct imine formation by oxidative coupling of alcohols and amines under solvent free conditions. Among the catalysts, CuAl $MO_{20\%C}$ (catalyst synthesized by adding 20% activated carbon) shows the best activity and selectivity for this reaction. Here, air is used as the oxidant which is considered as the most economical and green oxidant among different oxidizing agents. Pyridine adsorption results confirmed that the presence of higher number of Lewis acidic sites enhance the catalytic activity of the material. Various alcohol and amine substrates were smoothly

converted into the corresponding imines in good to excellent yields. According to catalytic activity studies and TG-MS data, surface oxygen availability and facile reversibility of oxygen readsorption on the surface account for the superior activity and high durability of the CuAl $MO_{20\%C}$ catalyst. The regenerated catalyst showed 92% conversion with 100% selectivity even after the 4^{th} reuse.

In the fourth part, magnetically recyclable Ni/Graphene nanocomposites were synthesized via an in situ reduction growth process for selective reduction of nitroarenes into corresponding azoxybenzene at room temperature and under atmospheric pressure. Here, hydrazine hydrate ($N_2H_4.H_2O$) is used as the reducing agent which generates N_2 and water as byproducts. The catalyst exhibits a 100% conversion and selectivity to the target product without the use of any external additives. Under the optimized conditions, a variety of structurally different nitroarenes were selectively transformed to their corresponding azoxy products in high conversions. Furthermore, a high stability and recyclability of the catalyst were also observed under the investigated conditions.

Design, Synthesis and Applications of Layered Double Hydroxides (LDHs), Mixed Metal Oxides (MMOs) and Nanocomposites as Efficient Sorbents and Multi-Functional Catalysts

Madhavi Nirmani Pahalagedara, Ph. D

B.Sc., University of Peradeniya, 2010

A Dissertation

Submitted in Partial Fulfillment of the

Requirement for the Degree of

Doctor of Philosophy

At the University of Connecticut

2015

APPROVAL PAGE

Doctor of Philosophy Dissertation

Design, Synthesis and Applications of Layered Double Hydroxides (LDHs), Mixed Metal Oxides (MMOs) and Nanocomposites as Efficient Sorbents and Multi-Functional Catalysts

Presented by

Madhavi Nirmani Pahalagedara, B.Sc.

Major Advisor _____
Dr. Steven L. Suib

Associate Advisor _____
Dr. Christian Bruckner

Associate Advisor _____
Dr. Alfredo Angeles-Boza

Associate Advisor _____
Dr. Jose Gascon

Associate Advisor _____
Dr. Fatma Selampinar

University of Connecticut

2015

DEDICATION

To my parents, my husband Lakshitha and my sister

for the amazing support you have always provided

ACKNOWLEDGEMENTS

Foremost, I would like to express my sincere gratitude to my advisor Dr. Steven L. Suib for his guidance and continuous support throughout my graduate studies. His motivation, enthusiasm, and immense knowledge of multidisciplinary research were critical to me as a research scientist. He also gave me great opportunities to grow in other areas such as communication, administration, and leadership. I would also like to extend my gratitude to my associate advisors, Dr. Christian Bruckner, Dr. Alfredo Angeles-Boza, Dr. Jose Gascon, and Dr. Fatma Selampinar for their generous help, motivation, and advice.

My sincere appreciation is extended to Dr. Jose Gascon and Milinda Samaraweera for their collaborative work on molecular dynamics simulations studies. I would also like to express my gratitude to Drs. S. Darmarathne, Chung-Hao Kuo, Aparna Iyer and Yashan Zhang for their help and support. My appreciation also goes to current group members David Kriz, Curt Guild, Sheng-Yu Chen, Zhu Luo, Wenqiao Song, Junkai He, Ran Miao, Saiful Seraji, Sourav Biswas, Becca Gottlieb, Wei Zhong, Andrew Meguerdichian, Wimalika Thalgaspitiya and Dinithi Rathnayake for their support in my projects.

I would like to extend my heartiest gratitude to my husband Lakshitha, who has been the most patient and supportive person who stood beside me during my academic journey over the past few years. I am highly indebted to my parents W.M. Ranasinghe and A.K. Tennakoon, for their continuous support in my education. Finally I would like to express my deepest gratitude to my sisters and brothers who motivated and supported me throughout my life.

TABLE OF CONTENTS

LIST OF FIGURES

LIST OF SCHEMES

LIST OF TABLES

CHAPTER I. ORDERED MESOPOROUS MIXED METAL OXIDES: REMARKABLE EFFECT OF PORE SIZE ON THE CATALYTIC ACTIVITY.

1.1. Introduction

Synthesis of ordered porous materials has attracted a great deal of attention due to their intensive applications in shape/size-selective catalysis,[1] gas storage,[2] drug storage and delivery,[3] adsorption based gas/vapor separation,[4] photonic crystals,[5] as well as in low-dielectric constant materials.[6] Their highly ordered structures with unique pore shapes and narrow pore size distributions directly facilitate to perform their functions in a particular application. Materials such as zeolites,[7] aluminophosphates,[8] carbon,[9] mixed metal oxides,[10] and silica nanofibers,[11] with hierarchical structures have been synthesized in recent years. Among them mixed metal oxides can be considered as promising materials in heterogeneous catalysis due to their tunable surface compositions. Mixed metal oxides with high surface area, and good metal dispersion can be obtained by a controlled thermal treatment of the corresponding layered double hydroxide (LDH) precursor.

Due to the biocompatibility and interlayer anion exchange capacity, LDH materials show a vast applicability.[12-16] Various synthetic routes such as, co-precipitation,[17] hydrothermal method,[18] ion-exchange method,[19] rehydration/ reconstruction,[20] and ultrasound irradiation[21] can be used to synthesize LDH

materials with different physicochemical properties. When LDHs are thermally decomposed at different temperatures, the materials will be converted into the corresponding mixed metal oxide (MMO) with the collapse of the layered structure. According to previous reports, the calcined LDH materials (cLDHs) show higher catalytic activities and selectivities than their uncalcined counterparts as they contain a higher number of basic sites,[22] regular pore structure including pore sizes and their distribution, pore volume, and surface area.[27] Among them, base catalyzed condensation and addition reactions are extremely significant as they are the key steps for the formation of large and complex molecules.[23]

The base catalyzed Knoevenagel condensation of carbonyl-containing compounds with active methylenes is one of the most primary, useful, and widely employed methods for the formation of carbon-carbon bonds.[24] This has been used as a general route for the preparation of several chemicals and chemical intermediates, bioactive materials, therapeutic drugs and pharmacological products.[25] This reaction is considered as a major step in natural product synthesis.[26] In general, alkali metal hydroxides (NaOH and KOH), and organic bases such as aliphatic amines, urea, pyridine, or piperidine are known to be effective homogeneous catalysts for the Knoevenagel condensation,[24] and several other Lewis bases and acids have also been reported. [27-30] Although effective, the use of such materials at a large scale has led to severe environmental problems due to the formation of huge amounts of organic waste.[27] To alleviate this problem, other modified inorganic solids,[31] cation-

exchanged zeolites,[31] hydrotalcites,[32] diamino-functionalized mesoporous materials,[33] and alkali containing MCM-41,[34] have been introduced as new heterogeneous catalysts. The use of new and less hazardous, environmentally friendly heterogeneous catalysts is receiving much attention due to several advantages such as mild reaction conditions, simplified product isolation, high yield and selectivity, ease in removal, and reuse of the heterogeneous catalyst.[28] Since the normal calcination conditions offer a limited control over the particles size and pore architectures, it is difficult to synthesize MMOs directly with highly ordered structures containing unique pore shapes and size distributions. The soft templating method is the most effective and the most widely used route for the synthesis of ordered structures.[35,36] In this method, organic surfactant molecules are considered as structure directing agents as they are used to create porosity within the material.[37] Therefore, the synthesis of porous MMOs can be carried out via the surfactant templating strategy by controlling the texture of materials at the nanometer scale.[38] Among various soft templates, pluronic tri block copolymer which is a non-ionic surfactant has been widely studied in this field. This copolymer has the $(PEO)_x-(PPO)_y-(PEO)_x$ structure with a central block of poly(propylene oxide), PPO, and end blocks of poly(ethylene oxide), PEO. The temperature, concentration and the block length have major effects on the aggregation behavior of the surfactant.[39] After the synthesis, the template can be removed by a calcination process to obtain the MMO with a unique porous structure.[37]

In the present study, we report the synthesis of ordered mesoporous MMOs with NiAl LDH using pluronic-F127 ($(PEO)_{100}$−$(PPO)_{65}$−$(PEO)_{100}$) as the structure directing agent and its application as a promising base catalyst in the Knoevenagel condensation. Here, a sonochemical technique was used to synthesize the NiAl LDH material. Subsequently, to liberate the porosity, the template was removed by thermal treatment. A series of NiAl MMOs with different pore size distributions were prepared by controlling the F127 concentration, and calcination temperature. Finally, the dependence of catalytic activity on the surface properties of the NiAl MMOs was investigated. This soft templating method can be used to synthesize materials with tunable surface properties with uniform pore size distributions. Therefore, this preparation method can be used to synthesize different ordered mesoporous mixed metal oxides with controlled pore sizes, acting as selective catalysts for various reactions. Hence, our study sheds light on the remarkable effect of pore size on the catalytic activity.

1.2. Experimental Section

1.2.1. Materials

Nickel nitrate hexahydrate ($Ni(NO_3)_2{\cdot}6H_2O$), aluminum nitrate nonahydrate($Al(NO_3)_3{\cdot}9H_2O$), sodium hydroxide (NaOH) and pluronic-F127 ($(PEO)_{100}$-$(PPO)_{65}$-$(PEO)_{100}$) were purchased from Sigma-Aldrich and were used without further purification. Double distilled water was used in all experiments.

1.2.2. Synthesis of pluronic-F127 templated NiAl LDH and mesoporous MMOs

The precursor NiAl LDH (Ni/Al molar ratio = 3) was synthesized through a co-precipitation followed by ultrasound irradiation process, in the presence of F127. Synthesis was done by adding 1.5 mmol of $Ni(NO_3)_2 \cdot 6H_2O$, 0.5 mmol of $Al(NO_3)_3 \cdot 9H_2O$, and a known amount of F127 into 30 mL deionized water under vigorous stirring at room temperature. The final pH value of the reaction mixture was adjusted to 10.0 with sodium hydroxide solution. The resultant suspension was immediately exposed to ultrasonic irradiation in a Branson 3210 ultrasonic bath equipped with a heater for 1 h at 65°C. After irradiation, the resultant apple green colored solid was filtered and washed with distilled water several times until the pH of the filtrate was 7. The washed precipitate was then dried under vacuum at 60°C for 12 h. The entire procedure was repeated, changing the amount of F127 (1%, 3%, 5% and 7%-% w/v) added while keeping other reaction conditions constant, to obtain a series of F127-templated LDHs. The resulted product was named NiAl-$F127_{X\%}$ where x presents the amount of F127. The dried powder was further calcined at various temperatures in air in order to remove the template. The obtained calcined materials were denoted NiAl-$F127_{X\%}CY_Z$(Y = 320,450,550,650,750,850,1000 and Z = 5), where Y stands for calcination temperatures in degrees Celsius and Z stands for the calcination period in hours. Controlled experiments were also carried out by repeating the

whole process in the absence of the soft template. Synthesized MMOs were named NiAl-CY_Z.

1.2.3. Structural characterization of pluronic-F127 templated NiAl LDH and mesoporous MMOs

1.2.3.1. X-Ray Powder Diffraction Studies

Powder X-ray diffraction patterns (XRD) of pluronic-F127 templated LDHs and MMOs were obtained using a Rigaku Ultima IV diffractometer with Cu Kα(λ = 0.15406 nm) radiation with a beam voltage of 40 kV and a beam current of 44 mA. Continuous scans were taken in a 2θ range of 5-75° with a scanning rate of 2.0 °/min, and the phases were identified using the International Center for Diffraction Data (ICDD) database.

1.2.3.2. Scanning Electron Microscopy

Surface morphologies of the synthesized materials were studied using a field emission scanning electron microscope (FE-SEM) on a Zeiss DSM 982 Gemini instrument with a Schottky emitter at an accelerating voltage of 2.0 kV with a beam current of 1.0 mA. The samples were ultrasonically suspended in absolute ethanol and dispersed on Au-coated silicon chips and then dried overnight under vacuum.

1.2.3.3. Transmission Electron Microscopy

High-resolution transmission electron microscopy (HR-TEM) was used to examine the surface morphologies and the crystalline structures of the materials using a JEOL 2010 instrument with an accelerating voltage of 200 kV. The samples were prepared by dispersing the material in ethanol. Then a drop of the dispersion was placed on a carbon coated copper grid and allowed to dry before analysis.

1.2.3.4. N_2 Sorption Studies

The nitrogen sorption experiments were performed using Quantachrome Autosorb iQ_2 instrument instrument using N_2 gas as the adsorbate at 77 K by a multipoint method. The Brunauer- Emmett-Teller (BET) method was used to determine the specific surface area and the Barrett-Joyner-Halenda (BJH) desorption method was used to calculate the pore size distribution and pore volume. Prior to the analysis, all the samples were degassed at 150˚C for 12 h in order to remove any adsorbed species.

1.2.4. Catalytic activity: Knoevenagel condensation between benzaldehyde and malononitrile

For catalytic studies, the Knoevenagel condensation reaction between benzaldehyde and malononitrile was carried out in a batch reactor.

Benzaldehyde, malononitrile, ethanol, toluene, tetarhydrofuran (THF) and dimethylsulfoxide (DMSO) were purchased from Sigma-Aldrich and used without further purification. A mixture of 10 mmol of benzaldehyde, 10 mmol of malononitrile, and 50 mg of NiAl MMO were stirred in 10 mL of ethanol and the reaction was conducted at 60˚C for 30 minutes in an oil bath under air atmosphere (Scheme 1.1).

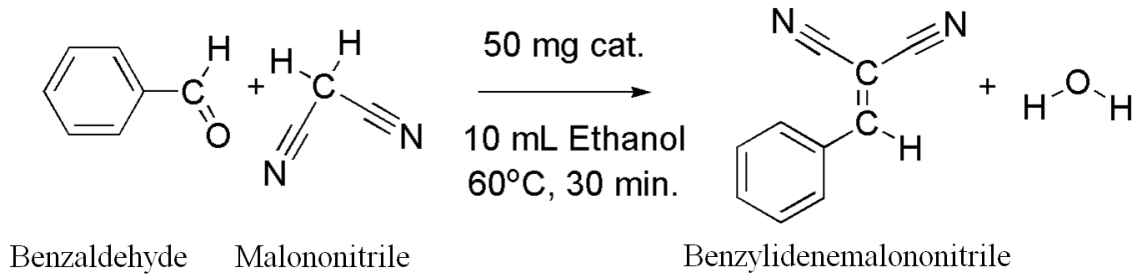

Scheme 1.1. Knoevenagel condensation reaction between benzaldehyde and malononitrile.

The spent catalyst was recovered by centrifuging the reaction mixture, washing with ethanol and drying in an oven at 120˚C for 12 h. The gas chromatography-mass spectroscopy (GC-MS) method was used for the quantitative analysis and identification of the reaction product (benzylidenemalononitrile). Analyses were performed using a HP 5971 mass selective detector coupled to a HP 5890 Series II gas chromatograph equipped with a thermal conductivity detector (TCD) through an HP-1 (nonpolar cross-linked methyl siloxane) column with dimensions of 12.5 m × 0.2 mm ×0.33 μm.

1.3. Results

1.3.1. Structural characterization of pluronic-F127 templated NiAl LDH and mesoporous MMOs

The XRD pattern of NiAl-F127$_{3\%}$LDH material is displayed in Figure 1.1a. All the peaks observed could be attributed to the characteristic LDH-type structure with sharp, symmetric peaks at low diffraction angles and broad, asymmetric peaks in the medium range. The existence of an ordered stacking arrangement is confirmed by the presence of a series of (00*l*) symmetric peaks indexed as (003), (006), and (009) at low 2θ angle. As synthesized LDH material possesses a BET surface area of 17 m^2/g and a pore volume of 0.02 cm^3/g with a pore diameter of 3.4 nm (Table 1.1).

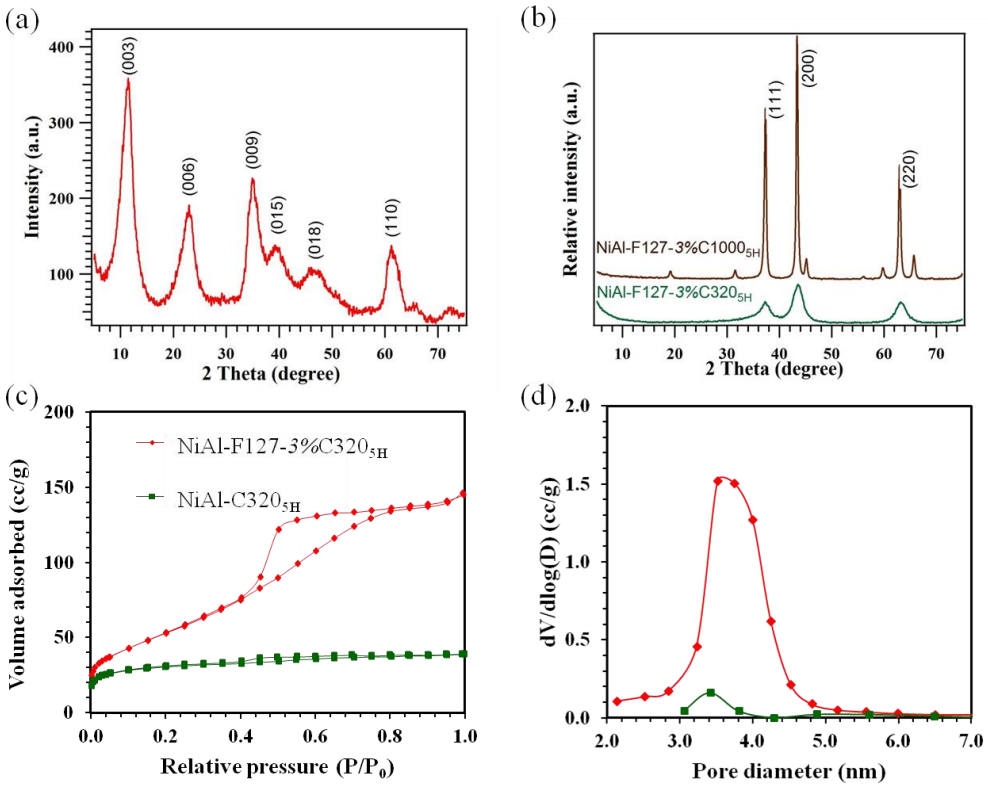

Figure 1.1. (a) X-ray diffraction pattern of NiAl-F127$_{3\%}$LDH. (b) XRD patterns of NiAl MMOs calcined at 320˚C and 1000˚C. (c) N_2 adsorption/desorption isotherms and (d) pore size distributions of NiAl MMOs synthesized with and without the structure directing agent.

Table 1.1. Crystallite sizes, specific surface areas, pore parameters, conversions and selectivities of different NiAl MMOs.[a]

Catalyst	Crystallite Size (nm) - (111) plane	BET SA (m^2/g)	BJH desorption pore volume (cm^3/g)	BJH desorption pore diameter (nm)	Conversion (%)	Selectivity (%)
NiAl-F127$_{3\%}$LDH	3.4[b]	17	0.02	3.4	15	100
NiAl-C320$_{5H}$	7.7	97	0.02	3.4	27	100
NiAl-C750$_{5H}$	14.3	99	0.12	3.4	49	100
NiAl-F127$_{3\%}$C320$_{5H}$	2.8	184	0.20	3.7	47	100
NiAl-F127$_{3\%}$C450$_{5H}$	4.4	102	0.33	5.6	78	100
NiAl-F127$_{3\%}$C550$_{5H}$	5.2	97	0.23	6.2	90	100
NiAl-F127$_{3\%}$C650$_{5H}$	5.6	102	0.20	7.1	94	100
NiAl-F127$_{3\%}$C750$_{5H}$	6.8	103	0.24	7.7	> 99	100
NiAl-F127$_{3\%}$C850$_{5H}$	7.4	75	0.18	7.1	85	100
NiAl-F127$_{3\%}$C1000$_{5H}$	22.7	19	0.07	9.4	13	100
NiAl-F127$_{1\%}$C750$_{5H}$	6.6	52	0.15	7.2	85	100
NiAl-F127$_{5\%}$C750$_{5H}$	6.2	57	0.23	12.0	88	100
NiAl-F127$_{7\%}$C750$_{5H}$	7.8	54	0.21	9.3	86	100

[a] Reaction conditions: 10 mmol of benzaldehyde, 10 mmol of malononitrile, in 10 mL of ethanol, 50 mg of NiAl MMO, 60˚C, 30 min. Conversion and selectivity determined and confirmed by GC-MS.

[b] Average crystallite size of NiAl-F127$_{3\%}$LDH.

The relationship between the calcination temperature and the catalytic activity was investigated by calcining NiAl-F127$_{3\%}$LDH samples at different temperatures. When the material is calcined at different temperatures, the

layered structure of the original LDHs is completely destroyed and indicates only NiO diffraction peaks. The peak intensities increase when the calcination temperature is increased from 320˚C to 1000˚C (Figure 1.1b).The crystallite sizes of NiAl MMOs calcined at different temperatures were calculated using the (111) reflection (Figure 1.2a), according to the Debye-Scherrer equation, L = 0.89λ/β(θ) cos θ where L is the crystallite size, λ is the wavelength of the radiation used, θ is the Bragg diffraction angle, and β(θ) is the full width at half maximum. Crystallite sizes found to increase gradually from 2.8 nm to 7.4 nm when increasing the temperature from 320˚C to 850˚C. A drastic increase in crystallite size (22.7 nm) was obtained for the catalyst sample calcined at 1000˚C (Figure 1.2b).

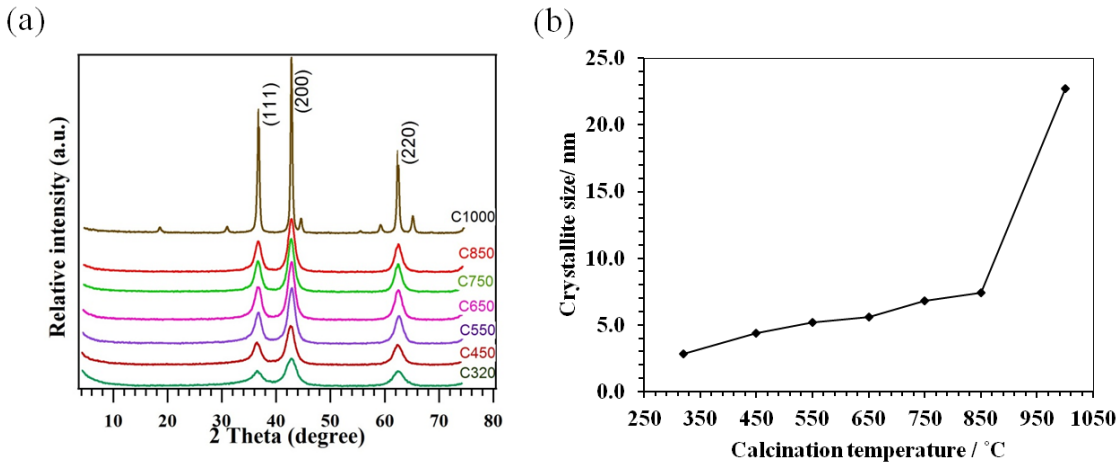

Figure 1.2. (a) XRD patterns of NiAl MMOs calcined at different temperatures. (b) Evolution of the crystallite dimension deduced from Scherrer's equation applied on the (111) diffraction peaks.

The effect of adding the soft template in the formation of an ordered porous structure was studied by nitrogen sorption analysis. Figure 1.1c shows

the adsorption isotherms of NiAl MMOs synthesized with and without F127. Compared to NiAl-$C320_{5H}$, NiAl-$F127_{3\%}C320_{5H}$ shows a steep gas uptake at low relative pressures. This hysteresis loop represents a Type-IV isotherm with H2-type indicating the presence of mesopores. The increase in the adsorption quantity in the region $0.4<P/P_o<0.8$ can be attributed to capillary condensation in the mesopores. The physico-chemical properties (specific surface area, pore volume, pore diameter) of NiAl MMOs prepared with and without F127 are compared in Table 1.1. The surface area of the material could be increased from 97 m^2/g to 184 m^2/g after adding the soft template. NiAl-$C320_{5H}$ exhibited a pore volume of 0.02 cm^3/g with a pore diameter of 3.4 nm. After adding F127, both the pore volume and the pore diameter increased up to 0.20 cm^3/g and 3.7 nm with a huge increase in the porosity. Corresponding BJH desorption pore size distributions are given in Figure 1.1d.

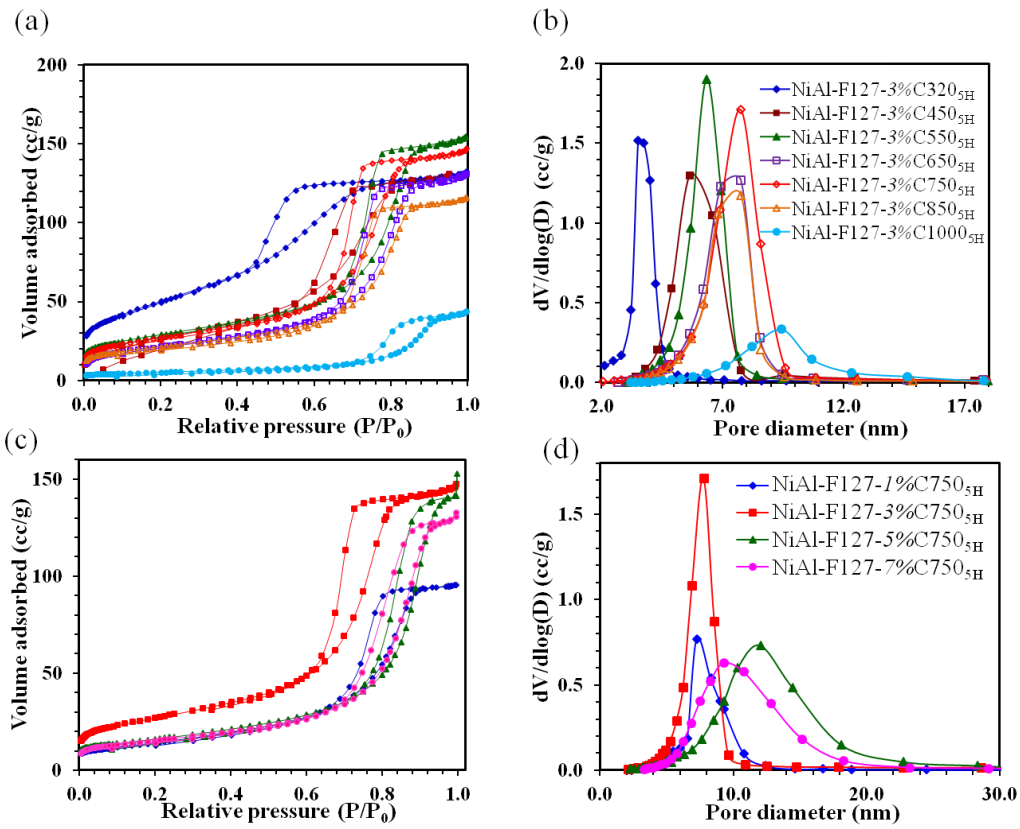

Figure 1.3. (a) N_2 adsorption/desorption isotherms and (b) BJH pore size distribution curves of NiAl MMOs calcined at different temperatures. (c) N_2 adsorption/desorption isotherms and (d) BJH pore size distribution curves of NiAl MMOs synthesized with different amounts of pluronic-F127.

Porous MMOs obtained by calcining NiAl-F127$_{3\%}$LDH samples at different temperatures were analyzed by N_2 sorption measurements to study their textural properties and pore size distributions. N_2 adsorption/desorption isotherms and BJH pore size distributions of the obtained MMOs are presented in Figures 1.3a and 1.3b. Accordingly, all the samples calcined at different temperatures contain a porous network that is accessible from the outside. NiAl-F127$_{3\%}$C320$_{5H}$ gave a

hysteresis loop which represents an H2 Type-IV isotherm indicating the presence of mesopores. When increasing the calcination temperature from 450 to 850˚C, hysteresis loops shift to a higher pressure. The result is further confirmed by the corresponding pore size distributions in Figure 2b associating narrow distributions of relatively uniform pores. NiAl-F127$_{3\%}$C320$_{5H}$ showed the highest BET surface area (184 m^2/g) among the samples. However, the increase of calcination temperature up to 1000˚C gave a very low specific surface area of 19 m^2/g with a small hysteresis loop. High temperatures lead to restrict the formation of the mesoporous structure of MMOs and the hysteresis loop shifts to a higher pressure, between 0.75 and 1.0. Highest pore volume (0.33 cm^3/g) was observed for NiAl-F127$_{3\%}$C450$_{5H}$ while NiAl-F127$_{3\%}$C1000$_{5H}$ gave the lowest pore volume (0.07 cm^3/g). A remarkable observation is that during heat treatment, the BJH desorption pore diameters increase from 3.7 nm to 9.4 nm, and regardless of the calcination temperature the materials show characteristic Type IV adsorption isotherms, implying the materials preserve the mesoporous structure. Surface area, pore size, and pore volume data for all the samples calcined at different temperatures have been tabulated in Table 1.1.

The effect of the amount of the surfactant was studied by altering the concentration of F127 in the synthesis process. Figure 1.3c shows N_2 adsorption/desorption isotherms of NiAl MMOs calcined at 750˚C for 5 hours with different amounts of F127. All of them gave Type IV isotherm with H2-type indicating the presence of mesopores. The sample with 1% pluronic-F127 showed a shorter gas uptake compared to other samples. The increase of

pluronic-F127 concentration shifts the hysteresis loop to a higher pressure. Figure 1.3d shows the pore size distribution curves of the MMOs synthesized with different concentrations of F127.

NiAl-F127$_{3\%}$C750$_{5H}$ sample gave the highest BET surface area (103 m^2/g) and the highest pore volume (0.24 cm^3/g) with a pore diameter of 7.7 nm among the compositions tested. Other samples gave wide pore size distributions. Increasing the amount of surfactant from 1% to 5% leads to an increase in the pore diameter from 7.2 nm to 12.0 nm and further increase leads to a decrease in pore diameter. Specific surface area values and pore parameters of NiAl MMOs with different amounts of F127 are given in Table 1.1. According to the obtained results, the amount of F127 plays an important role in forming the mesoporous structure.

The crystallite sizes of NiAl MMOs prepared with different amounts of F127 were calculated using the (111) reflection. Crystallite sizes were found to increase from 6.6 nm to 6.8 nm when increasing the F127 amount from 1% to 3% and a sudden drop was observed for the sample synthesized with 5% F127 (6.2 nm). NiAl-F127$_{7\%}$C750$_{5H}$ gave the largest crystallite size among the series which was 7.8 nm (Table 1.1).

1.3.2. Effect of calcination temperature and pluronic-F127 concentration on catalytic performance

Knoevenagel condensation reaction was carried out to investigate the catalytic performances of as-synthesized materials, and the results for the

conversion of benzaldehyde and malononitrile after a reaction time of 30 minutes are given in Table 1.1. NiAl-LDH synthesized with 3% F127 exhibited a very low catalytic activity (15% conversion) compared to the calcined materials. NiAl-$F127_{3\%}C320_{5H}$ gave a relatively high conversion (as high as 47%) and a 100% selectivity; however, the one synthesized without the soft template (NiAl-$C320_{5H}$) gave a very low conversion (27%) in the reaction (Table 1.1).

The effect of calcination temperature on the Knoevenagel condensation reaction was studied and the results are given in Table 1.1. When increasing the calcination temperature from 320˚C to 1000˚C, catalytic activity was increased gradually and the maximum conversion (> 99%) was observed for the material calcined at 750˚C (NiAl-$F127_{3\%}C750_{5H}$). Further increase in temperature leads to a decrease in conversion in the condensation reaction. NiAl-$F127_{3\%}C1000_{5H}$, which was calcined at 1000˚C, gave the lowest conversion (13%) among the series.

The dependence of the catalytic reactivity on pluronic F-127 concentration was studied for the samples calcined at 750˚C and the results are given in Table 1.1. All the compositions of pluronic F-127 (1%, 3%, 5% and 7% -% w/v) gave conversions above 85% after 30 minutes under same experimental conditions. When increasing the pluronic F-127 concentration from 1% to 3%, catalytic activity was increased and the maximum conversion (> 99%) was observerd for the material synthesized with 3% pluronic F-127 (NiAl-$F127_{3\%}C750_{5H}$). Further increase of F-127 amount leads to a decrease in conversion. Based on the data

obtained, NiAl-F127$_{3\%}$ C750$_{5H}$ gave the highest conversion in the reaction hence further characterization was performed on its physiochemical properties.

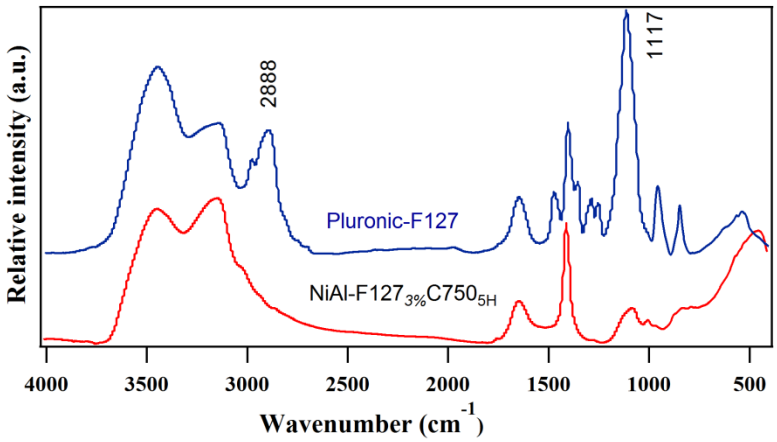

Figure 1.4. FTIR spectra of pluronic-F127 and NiAl-F127$_{3\%}$C750$_{5H}$.

The material purity and the complete removal of the surfactant residuals were confirmed by FTIR. As seen from FTIR spectra in Figure 1.4, two characteristic peaks were observed for pluronic-F127 at 2888cm^{-1} and 1117cm^{-1} which can be attributed to the C–H stretching vibrations of PEO segments and C–O–C stretching vibrations. In contrast, those two peaks are absent in the calcined material (NiAl-F127$_{3\%}$C750$_{5H}$) confirming the complete removal of the surfactant upon calcination. The effect of the addition of the structure directing agent in the formation of the mesoporous structure was studied by nitrogen sorption analysis. Figure 1.5a shows the adsorption/desorption isotherms of the best NiAl MMO catalyst calcined at 750˚C with and without F127. Compared to NiAl-C750$_{5H}$, NiAl- F127$_{3\%}$C750$_{5H}$ shows a steep gas uptake. This hysteresis loop represents an H2 Type-IV isotherm indicating the presence of mesopores and regardless of the presence of F127, the materials show very similar surface

area values. Furthermore, both the materials gave uniform pore size distributions (Figure 1.5b). However, the pore diameter was remarkably increased from 3.4 nm to 7.7 nm upon the addition of F127 giving a very high porosity and a pore volume (0.24 cm^3/g) compared to the material synthesized without F127 in the initial synthesis step. Corresponding BET surface areas, pore-size distributions, and pore volumes are shown in Table 1.1.

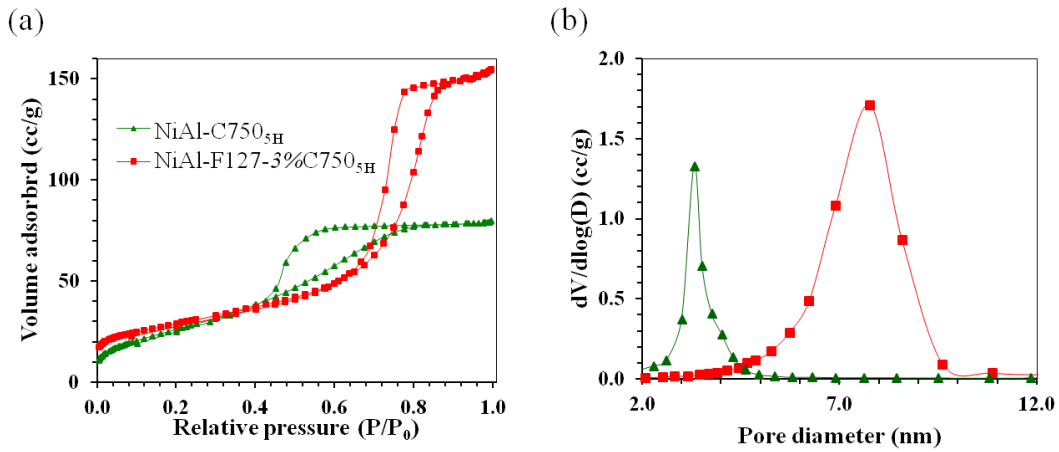

Figure 1.5. (a) N_2 adsorption/desorption isotherms and (b) BJH pore size distributions of NiAl-F127$_{3\%}$ C750$_{5H}$ and NiAl-C750$_{5H}$.

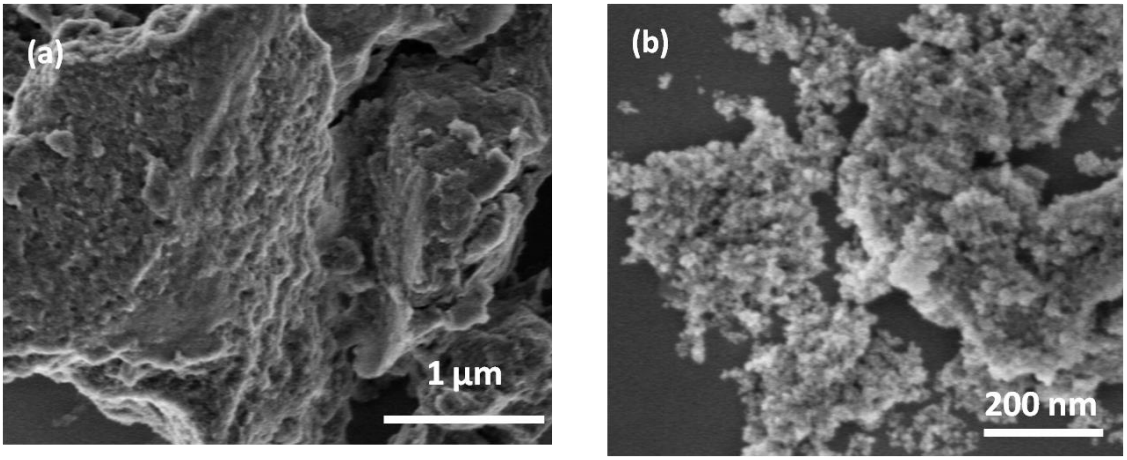

Figure 1.6. FE-SEM images of (a) NiAl-F127$_{3\%}$LDH (b) NiAl-F127$_{3\%}$ C750$_{5H}$.

The surface morphology of the NiAl-F127$_{3\%}$LDH material and the NiAl-F127$_{3\%}$C750$_{5H}$ MMO were observed by scanning electron microscopy. Figure 1.6a shows a typical FE-SEM image of the NiAl-LDH composed of aggregates of plate-like sheets which are stacked in a perpendicular fashion. Figure 1.6b shows the hierarchically porous NiAl MMO obtained by the calcination of the precursor LDH material. The porous structure is composed of aggregates of almost spherical particles.

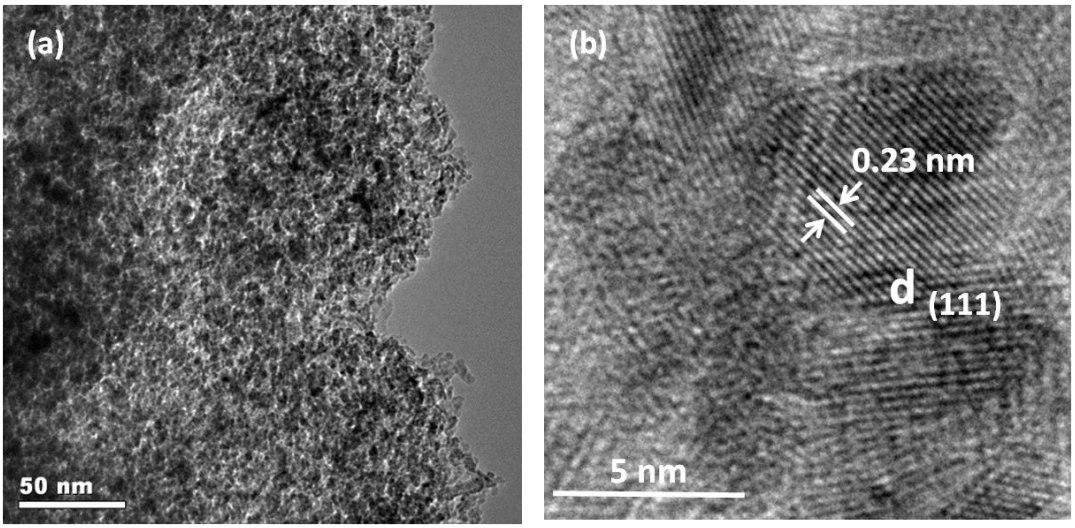

Figure 1.7. TEM and HRTEM images of NiAl-F127$_{3\%}$ C750$_{5H}$ (a) low magnification image showing the morphology (b) lattice fringes of the (111) plane.

TEM and HRTEM images of NiAl-F127$_{3\%}$C750$_{5H}$ are shown in Figure 1.7 and Figure 1.8a,b. According to the TEM image (Figure 1.7a), the material is composed of small crystalline nanosized particles that are organized and that remained stable even at elevated temperature. The HRTEM image (Figure 1.7b) shows lattice fringes that correspond to the (111) plane with a distance of 0.23

nm between the two planes, which agrees well with the XRD d-spacing value of the NiAl-F127$_{3\%}$C750$_{5H}$. From TEM images the porosity of the material arises mainly from the inter-particle separations. The material calcined at 750ºC is very crystalline and contains inter-particle voids (Figure 1.8a,b). In contrast, the LDH material is less crystalline and does not contain inter-particle spaces ((Figure 1.8c,d). Therefore, the evolution of the porosity with treatment temperature is clearly explained by Figure 1.8.

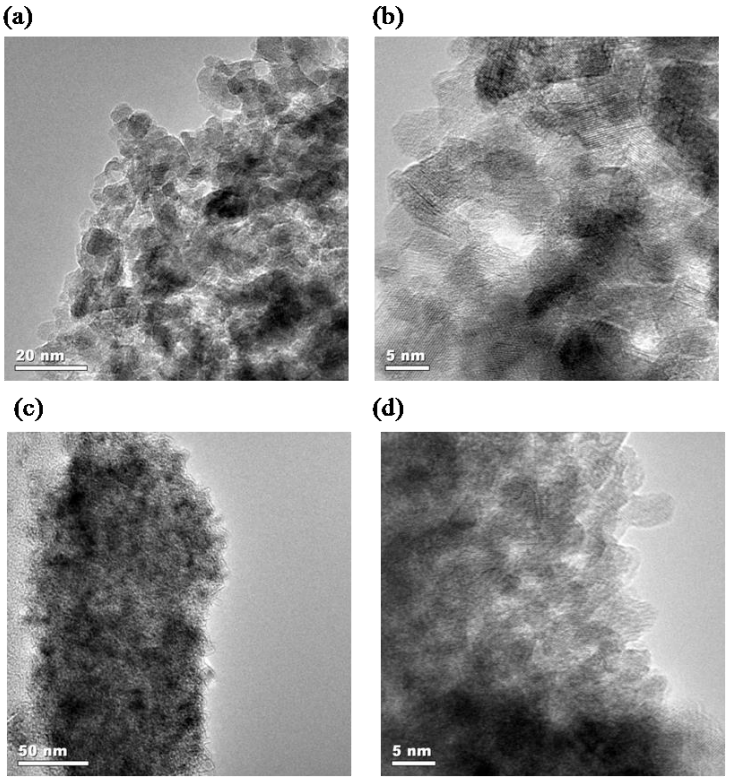

Figure 1.8. HR-TEM images of NiAl-F127$_{3\%}$C750$_{5H}$ (a and b) and NiAl-F127$_{3\%}$LDH (c and d).

1.3.3. Effect of reaction conditions on catalytic performance

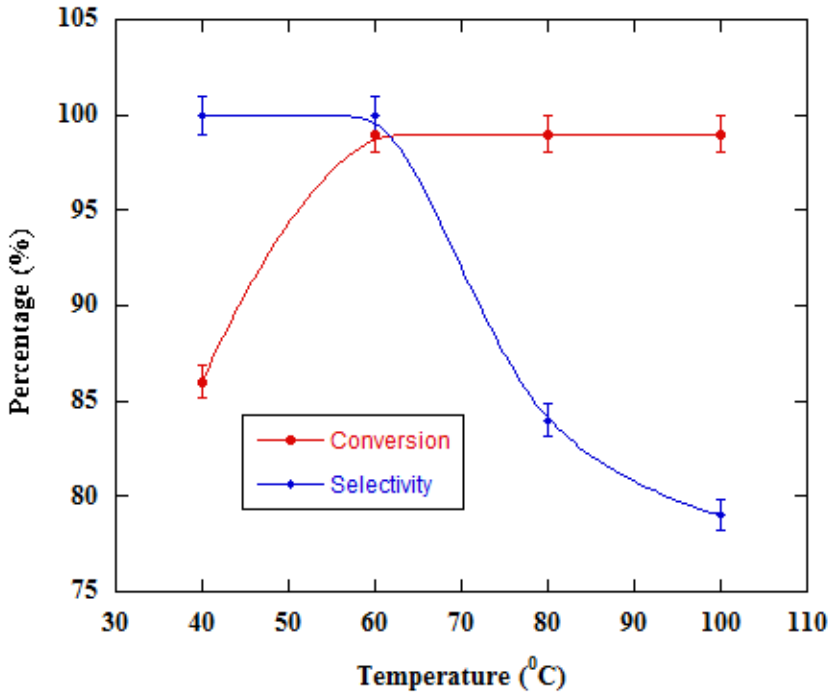

Figure 1.9. Effect of temperature on the catalytic performance.

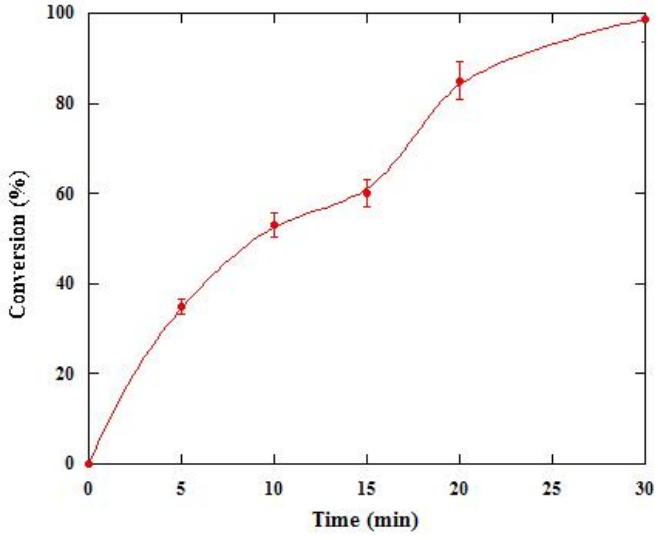

Figure 1.10. Effect of reaction time on the catalytic performance.

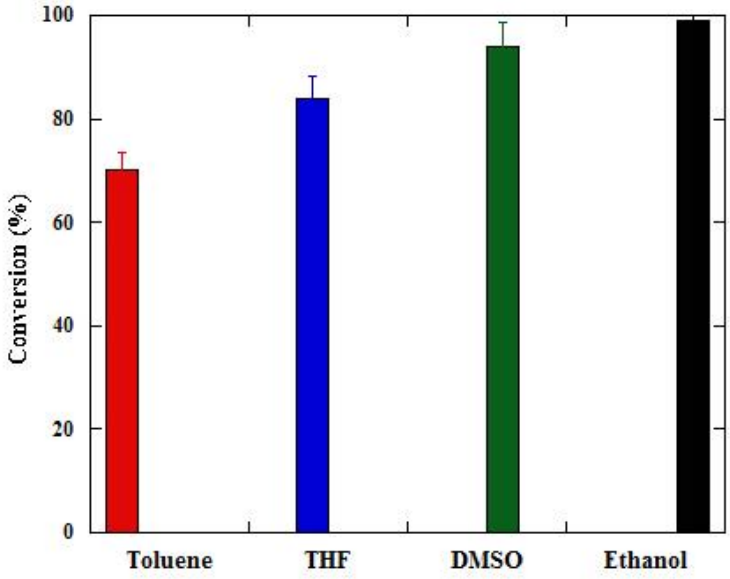

Figure 1.11. Effect of solvent on the catalytic performance .

NiAl-F127$_{3\%}$C750$_{5H}$ catalyst was used to evaluate the effect of reaction temperature, time, and the solvent since this material exhibited the highest catalytic performance. The reaction was carried out at different temperatures to investigate the effect of the temperature on the catalytic performance and the results are given in Figure 1.9. The percentage of conversion surged along with increasing reaction temperature from 86% at 40˚C to > 99% at 60˚C with a 100% selectivity for the Knoevenagel product. Any further increase in the temperature decreases the selectivity of the reaction. In Figure 1.10, the conversion of benzaldehyde and malononitrile is plotted as a function of time. Conversion increased with time and the maximum conversion of > 99% with 100% selectivity for Knoevenagel product was found at 30 minutes of reaction time. Moreover, the

reaction between benzaldehyde and malononitrile was carried out in the absence of catalyst, under the same reaction conditions and a significant conversion was not observed. These data suggest that the Knoevenagel condensation reaction described herein is entirely catalytic in nature. In order to study the effect of solvent, various solvents (toluene, THF, DMSO and ethanol) with different properties were used for the reaction in the presence of the NiAl-F127$_{3\%}$C750$_{5H}$ catalyst. According to the results given in Figure 1.11, catalytic performance was strongly influenced by the solvent used. Catalytic activity of NiAl-F127$_{3\%}$C750$_{5H}$ decreased in the order of ethanol (> 99%)> DMSO (94%) > THF (84%) > toluene (70%). Among the solvents used, toluene gave the lowest conversion.

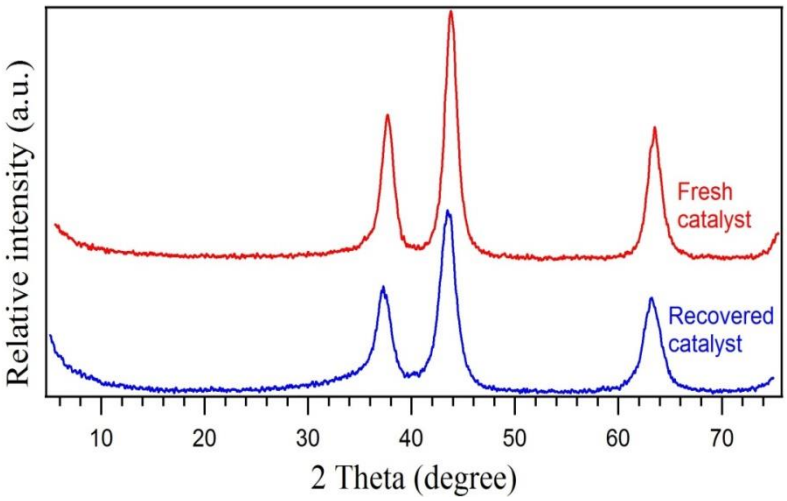

Figure 1.12. X-ray diffraction patterns of the fresh NiAl-F127$_{3\%}$ C750$_{5H}$ catalyst and the recovered catalyst.

The reusability of the NiAl-F127$_{3\%}$C750$_{5H}$ catalyst was tested in three repetitive reaction cycles for the reaction between benzaldehyde and malononitrile. The XRD patterns of the fresh catalyst and the recovered catalyst

are shown in Figure 1.12. According to XRD results, the structure of NiAl MMO does not change even after multiple repeated cycles. The durability of the catalyst during Knoevengel reaction is given in Figure 1.13. The regenerated catalyst showed 93.0%, and 89.0% of the initial catalytic activity after the first and the second regeneration cycles, respectively.

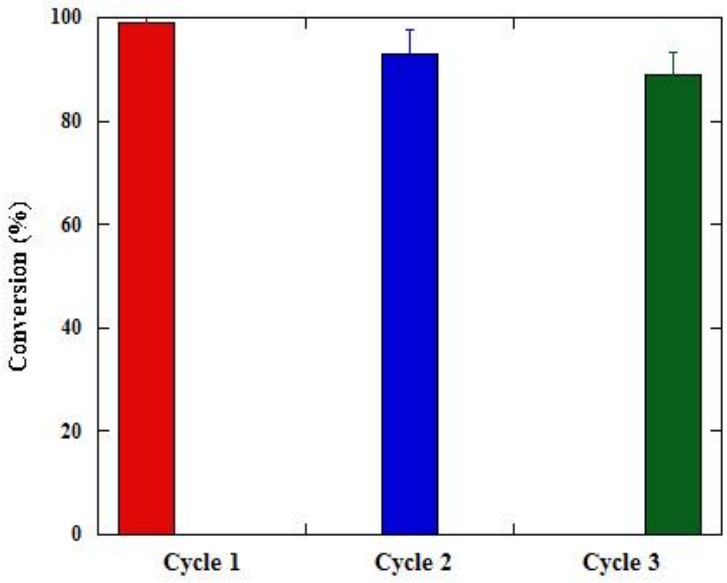

Figure 1.13. Recyclability of NiAl-F127$_{3\%}$ C750$_{5H}$ catalyst in the Knoevenagel condensation reaction.

1.4. Discussion

The relationships between catalytic reactivity and the surface properties of the catalyst have been discussed extensively in the literature.[40,41,42] In the current

study, the catalytic reactivity is very sensitive towards the surface properties of the NiAl MMO catalyst. This synthesis process perfectly illustrates the usefulness of this approach, since the crystal and the surface structures of the final material (crystallinity, surface area, pore diameter, pore volume) can be readily modified by adjusting several synthesis parameters, such as surfactant concentration and calcination temperature under the same reaction conditions.[43,44]

The effect of the presence of the soft template in the formation of a mesoporous structure was studied by nitrogen sorption analysis. Nitrogen sorption study revealed that the NiAl-F127$_{3\%}$C320$_{5H}$ sample has a higher specific surface area, pore diameter, and mesopore volume than conventional NiAl-C320$_{5H}$ synthesized without the structure directing agent. Upon removing the surfactant pluronic-F127, pores develop inside the material, leading to a high surface area and a pore volume. Combustion of the surfactant during the calcination process induces very fine pores. Furthermore, the surfactant also reduces the particle growth that might result in a higher surface area. Such an assembly is not possible in the absence of the surfactant, and there were significantly less numbers of pores in the structure. As a result, the surface area (97 m^2/g) and the pore volume (0.02 cm^3/g) are much lower for NiAl MMO prepared without pluronic-F127.[44,45] Xia *et. al*. describes the formation of mesoporous organosilica materials using alkyltrimethylammonium bromide (C*n*TAB) surfactants with different alkyl chain lengths (*n* = 12, 14, 16, 18). However, for some *n* values, they have observed broad pore size distributions. [44] In their study, Ganguly *et. al*. used the cooperative self-assembly of the silica

precursor, tetraethyl orthosilicate (TEOS), with different surfactant molecules followed by the basic hydrolysis for the formation of mesoporous silica with varying pore sizes. In contrast to our method they have created intra-particle voids. [45] Therefore, our method is advantageous, as a direct calcination step is employed for the formation of pores with uniform sizes.

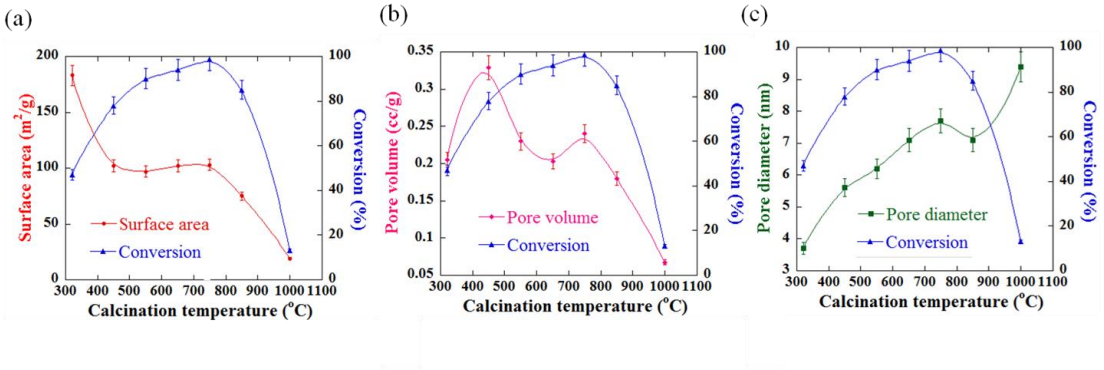

Figure 1.14. The effect of calcination temperature on (a) BET surface area (b) BJH pore volume (c) BJH pore diameter of NiAl MMOs and its catalytic activity.

The calcination temperature is an important parameter in controlling the physiochemical properties of the materials. When increasing the calcination temperature, the XRD peaks for LDHs completely disappear and only NiO peaks are indicated, signifying the decomposition of the original LDH layered structure. When increasing the calcination temperature from 320˚C to 1000˚C, peak intensities increase indicating that the crystal grains became larger forming more crystalline materials (Figure 1.2). At 1000˚C, larger particles are detected due to extensive sintering and the material shows some additional peaks signifying the formation of a $NiAl_2O_4$ spinel phase at elevated temperatures.[46] The crystallites

formed at higher calcination temperatures are larger in size, which can be attributed to thermally promoted crystallite growth.[47]

Calcination temperature exhibited a remarkable effect in determining the pore structure of the MMO material. Nitrogen sorption isotherms of samples calcined at different temperatures confirmed the porosity of NiAl MMO materials (Figure 1.3a). The total pore volume and specific surface area for samples decrease with increasing calcination temperature due to increasing the particle size and degree of agglomeration by the effect of sintering occurring in the material. The specific surface area of the samples decreases from 184 m^2/g at 320˚C to 19 m^2/g at 1000˚C suggesting significant sintering of the material at higher calcination temperatures.

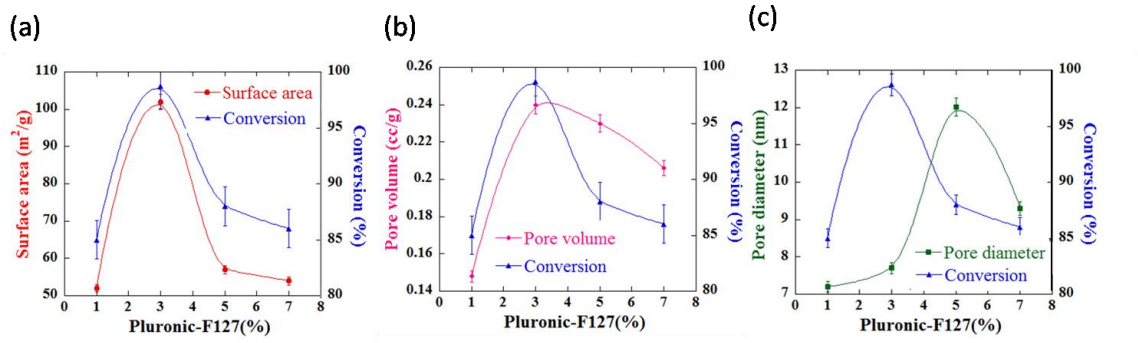

Figure 1.15. The effect of pluronic-F127 concentration on (a) BET surface area (b) BJH pore volume (c) BJH pore diameter of NiAl MMOs and its catalytic activity.

The variations of the conversions of benzaldehyde and malononitrile after 30 minutes as a function of the calcination temperature and surface properties of catalysts are reported in Figures 1.14a-c. The maximum conversion of > 99 %

was observed for NiAl-F127$_{3\%}$C750$_{5H}$ catalyst which had a moderate surface area (103 m^2/g). The materials calcined at 320˚C and 1000˚C which possessed the highest and the lowest surface area gave very low conversions (Figure 1.14a). This observation suggests that the reactivity is not entirely dependent on the surface area of the catalyst. Pore volume did not show a direct correlation with the calcination temperature. However, the BJH pore diameter increased as the calcination temperature was increased. Materials with very small or very large pore diameters gave low conversions in the reaction. The maximum catalytic activity was observed for the material with a pore diameter of 7.7 nm which was calcined at 750˚C (Table 1.1). This clearly confirms that the pore diameter of the NiAl MMO catalyst plays a crucial role in determining the conversion.

Control over the pore size and pore volume can be achieved by changing the amount of pluronic-F127 surfactant. The nitrogen sorption isotherms exhibit Type IV isotherms with a typical capillary condensation step into mesopores in the partial pressure (P/P_0) range of 0.6-1.[48,49,50] Surfactant molecules can aggregate to form micelles in an aqueous environment. Beyond the critical micelle concentration value, the self-assembly of micelles occurs to form spherical, rod-like micelles or bilayers and this self-assembly helps in the pore generation. These assemblies act as ‘placeholders’, what become void spaces to produce nanoporous material. Pluronic-F127 has large hydrophilic groups and a small hydrophobic group which can form normal spherical micelles in aqueous media. The concentration of the surfactant has a large impact on the size and

shape of the micelle and as reported, the spherical micelles undergo transitions to rod shape micelles and lamellar phases at higher concentrations. [37,51,52]

According to Figure 1.3d, NiAl-F127$_{1\%}$C750$_{5H}$ and NiAl-F127$_{3\%}$C750$_{5H}$ gave uniform pore size distributions. This may be due to the formation of spherical micelles at lower surfactant concentrations. NiAl-F127$_{3\%}$C750$_{5H}$ shows a higher porosity than NiAl-F127$_{1\%}$ C750$_{5H}$ and this clearly indicates the formation of a larger number of micelles when increasing the pluronic-F127 concentration from 1% to 3%. Further increase in the pluronic-F127 concentration gave wide pore size distributions indicating the presence of pores with different diameters. This may be due to the formation of rod shaped micelles and lamellar phases.

According to Figure 1.15a, when changing the pluronic-F127 concentration from 1% to 7%, both the surface area and the conversion are increased up to 3% and a further increase in the surfactant amount tends to lower those two factors. This indicates that the amount of pluronic-F127 determines the catalytic activity by controlling the surface area of the material. A similar trend was observed for the pore volume with the varying pluronic-F127 concentration. Pore diameter increases with increasing the pluronic-F127 amount giving the maximum diameter (12 nm) with 5% pluronic-F127. But the maximum conversion was observed for NiAl- F127$_{3\%}$C750$_{5H}$ in which the pore diameter is 7.7 nm (Table 1.1). When the pluronic-F127 concentration is 3%, a higher number of micelles with a uniform size distribution exist in the medium. Upon the

removal of the surfactant, NiAl MMO material is formed with a uniform pore size distribution and a high porosity.

Based to the above results, the catalytic activity of mesoporous NiAl MMOs was strongly dependent on the pore structure of the material. A reasonably high surface area is a requirement for an effective catalyst but, in this case, surface area alone is not the major controlling factor in determining the activity. In contrast, there seems to be a correlation between the pore diameter and the catalytic activity, and there is some dependence of activity on pore volume. The conversion is maximized where the pore diameter is 7.7 nm and smaller or larger pores offer lower activity.[53,54,55]

This observation is well-supported by the study done by Iwamoto *et al.* on remarkable effect of pore size on the catalytic activity of mesoporous silica for the acetalization of cyclohexanone with methanol. According to their study the catalytic activity was not dependant on the molecular size of the substrate but on the pore diameter of the catalyst.[56] In this respect, we suggest a few possible explanations based on the observed results. First, some synergistic effects may be involved with larger pores, but for pores less than the optimum diameter (7.7 nm), diffusion effects may determine the reactivity and second, the local orientation or concentrations of substrates may play a role.

Textural properties and surface morphology of the mesoporous material have been investigated by FE-SEM images. According to Figure 4b, the material is composed of tiny spherical particles and they are self-assembled to form large clusters. This may be due to the structure directing agent pluronic-F127

molecules used in the synthesis. Those molecules may have played the role of a capping agent, which controls the particle size growth.[57,58]

Condensation reactions were performed between 40˚C-100˚C using NiAl-$F127_{3\%}C750_{5H}$ catalysts, keeping other parameters constant. The percentage of yield surged along with increasing reaction temperature confirming the endothermic nature of the Knoevenagel condensation. With further increase in temperature above 60˚C, the conversion remained constant (> 99%) but the Knoevenagel product selectivity decreased due to the formation of more benzoic acid.[59]

The solvent choice for NiAl MMO catalyzed Knoevenagel condensation reaction was critical. The best conversion was observed with ethanol while the reaction in toluene resulted in the lowest yield. Toluene is a non-polar solvent and barely accepts any water liberated from the condensation reaction. Therefore, the reaction stops at a low product level. For the polar solvent THF, the released water is freely dissolved with the reactants giving a conversion of 84%. In DMSO, the liberated water can be bound as a hydrate and thereby is removed from the chemical equilibrium. The highest conversion was achieved with ethanol, where hydrogen bonding is used to remove liberated water from the condensation, shifting the equilibrium towards the product side. Moreover ethanol can be considered as an environmentally friendly solvent that is inexpensive, less toxic, and biodegradable.[60]

Direct reuse of the catalyst leads to a decrease in activity because the reactants and products were not completely desorbed from MMO and therefore,

the active sites were blocked. However, by washing NiAl MMO with ethanol and then drying in an oven at 120˚C for 12 hours, the catalyst could be recovered and reactivatd without considerable loss of catalytic activity. This effect can be attributed to the high stability of the NiAl MMO catalyst which effectively preserved the ordered mesoporous structure during aqueous media reactions.

1.5. Conclusion

In this study, a NiAl mixed oxide catalyst has been synthesized for the Knoevenagel condensation reaction which is one of the most primary, useful, and widely employed methods for the formation of carbon-carbon bonds. Ordered mesoporous NiAl MMOs were obtained by the thermal decomposition of pluronic-F127 templated NiAl LDHs. The effects of the pluronic-F127 concentration and the calcination temperature on the pore size distribution of the MMO were investigated by N_2 adsorption-desorption. As synthesized MMOs with different textural properties showed excellent catalytic activity in the Knoevenagel condensation of benzaldehyde with acidic methylene group-containing malononitrile for the synthesis of α,β,-unsaturated carbonyl compounds. Catalytic activities of NiAl MMO catalysts were strongly influenced by the surface properties of the material and the pore diameter played an important role in determining the catalytic performance. Among the catalysts tested, NiAl-$F127_{3\%}C750_{5H}$ material with a pore diameter of 7.7 nm showed the best conversion (> 99%) at 60˚C with 100% selectivity in 30 min. The highest

conversion was achieved with ethanol, which is an environmentally friendly solvent. The catalyst can be readily recovered and reused without significant loss of activity and selectivity. The pore size of this material is easily controllable and could be used as a potential catalyst in several other size and shape selective organic reactions. The preparation method discussed in this study could also be easily adopted for the synthesis of different mixed metal oxides for selective catalysis of various reactions.

References

(1) Chai, G. S.; Shin, I. S.; Yu, J. Synthesis of Ordered, Uniform, Macroporous Carbons with Mesoporous Walls Templated by Aggregates of Polystyrene Spheres and Silica Particles for Use as Catalyst Supports in Direct Methanol Fuel Cells. *Adv. Mater.* **2004***, 16*, 2057-2061.

(2) Morris, R.; Wheatley, P. Gas Storage in Nanoporous Materials. *Angew. Chem. Int. Edit.* **2008***, 47*, 4966-4981.

(3) Wang, S. Ordered mesoporous materials for drug delivery. *Microporous and Mesoporous Mater.* **2009***, 117*, 1-9.

(4) Morris, R. E.; Wheatley, P.S. Microporous Polyimides with Uniform Pores for Adsorption and Separation of CO_2 Gas and Organic Vapors. *Macromolecules* **2008**, 47, 4966 – 4981.

(5) Norris, D. J.; Vlasov, Y. A. Chemical Approaches to Three-Dimensional Semiconductor Photonic Crystals. *Adv. Mater.* **2001***, 13*, 371-376.

(6) Yang, C. M.; Cho, A. T.; Pan, F. M.; Tsai, T. G.; Chao, K. J. Spin-on Mesoporous Silica Films with Ultralow Dielectric Constants, Ordered Pore Structures, and Hydrophobic Surfaces. *Adv. Mater.* **2001***, 13*, 1099-1102.

(7) Christensen, C.H.; Johannsen, K.; Schmidt, I.; Christensen, C.H. Catalytic Benzene Alkylation over Mesoporous Zeolite Single Crystals: Improving Activity and Selectivity with a New Family of Porous Materials. *J. Am. Chem. Soc.* **2003**, 125, 13370-13371.

(8) Ristic, A.; Logar, N. Z.; Henninger, S. K.; Kaucic, V. The Performance of Small-Pore Microporous Aluminophosphates in Low-Temperature Solar Energy Storage: The Structure-Property Relationship. *Adv. Funct. Mater.* **2012**, 22, 1952-1957.

(9) Zhao, G.; He, J.; Zhang, C.; Zhou, J.; Chen, X.; Wang, T. Highly Dispersed Pt Nanoparticles on Mesoporous Carbon Nanofibers Prepared by Two Templates. *J. Phys. Chem. C* **2008,** *112,* 1028-1033.

(10) Carreon, M. A.; Guliants, V. V. Ordered Meso- and Macroporous Binary and Mixed Metal Oxides. *Eur. J. Inorg.Chem.* **2005***, 1*, 27-43.

(11) Zhou, L.; Hong, G.; Qi, L.; Lu, Y. Seeding-Growth of Helical Mesoporous Silica Nanofibers Templated by Achiral Cationic Surfactant. *Langmuir* **2009,** *25,* 6040–6044.

(12) Brito, A.; Borges, M.E.; Garı´n, M.; Herna´ndez, A. Biodiesel Production from Waste Oil Using Mg-Al Layered Double Hydroxide Catalysts. *Energy Fuels* **2009**, *23*, 2952–2958.

(13) Vaccari, A. Preparation and catalytic properties of cationic and anionic clays. *Catal. Today* **1998***, 41*, 53-71.

(14) Panda, H. S.; Srivastava R.; Bahadur D. In-Vitro Release Kinetics and Stability of Anticardiovascular Drugs-Intercalated Layered Double Hydroxide Nanohybrids. *J. Phys. Chem. B* **2009**, *113,* 15090-15100.

(15) Poznyak, S. K.; Tedim, J.; Rodrigues, L. M.; Salak, A. N.; Zheludkevich, M. L.; Dick, L. F. P.; Ferreira, M. G. S. Novel Inorganic Host Layered Double Hydroxides Intercalated with Guest Organic Inhibitors for Anticorrosion Applications. *ACS Appl. Mater. Inter.* **2009**, *1,* 2353–2362.

(16) Ma, R.; Liang, J.; Liu, X.; Sasaki, T. J. General Insights into Structural Evolution of Layered Double Hydroxide: Underlying Aspects in Topochemical Transformation from Brucite to Layered Double Hydroxide. *J. Am. Chem. Soc.* **2012**, *134,* 19915-19921.

(17) Lopez, T.; Bosch, P.; Ramos, E.; Gomez, R.; Novaro, O.; Acosta, D.; Figueras, F. Synthesis and Characterization of Sol-Gel Hydrotalcites Structure and Texture. *Langmuir* **1996**, *12*, 189–192.

(18) Ogawa, M.; Asai, S. Hydrothermal Synthesis of Layered Double Hydroxide Deoxycholate Intercalation Compounds. *Chem. Mater.* **2000**, *12*, 3253–3255.

(19) Morel-Desrosiers, N.; Pisson, J.; Israeli, Y.; Taviot-Gueho, C.; Besse, J.; Morel, J. Intercalation of dicarboxylate anions into a Zn-Al-Cl layered double hydroxide: microcalorimetric determination of the enthalpies of anion exchange. *J. Mater. Chem.* **2003**, 2582- 2585.

(20) Erickson, K. L.; Bostrom, T. E.; Frost, R. L. A study of structural memory effects in synthetic hydrotalcites using environmental SEM. *Mater. Lett.* **2005***, 59*, 226-229.

(21) Seida, Y.; Nakano, Y.; Nakamura, Y. Crystallization of layered double hydroxides by ultrasound and the effect of crystal quality on their surface properties. *Clay Clay Miner.* **2002***, 50*, 525-532.

(22) Zhao, X.; Zhang, F.; Xu, S.; Evans, D.G.; Duan, X. From Layered Double Hydroxides to ZnO-based Mixed Metal Oxides by Thermal Decomposition: Transformation Mechanism and UV-Blocking Properties of the Product. *Chem. Mater.* **2010**, *22*, 3933-3942.

(23) Gawande, M. B.; Pandey, R. K.; Jayaram, R. V. Role of mixed metal oxides in catalysis science-versatile applications in organic synthesis. *Catal. Sci. Technol.* **2012**, *2*, 1113–1125.

(24) Ansari, M. B.; Jin, H.; Parvin, M. N.; Park, S. Mesoporous carbon nitride as a metal-free base catalyst in the microwave assisted Knoevenagel condensation of ethylcyanoacetate with aromatic aldehydes. *Catal. Today* **2012***, 185*, 211-216.

(25) Zhang, X.; Man Lai, E. S.; Martin-Aranda, R.; Yeung, K. L. An investigation of Knoevenagel condensation reaction in microreactors using a new zeolite catalyst. *Appl.Catal. A-Gen.* **2004***, 261*, 109-118.

(26) Menezes, J. C. J. M. D. S.; Kamat, S. P.; Cavaleiro, J. A. S.; Gaspar, A.; Garrido, J.; Borges, F. Synthesis and antioxidant activity of long chain alkyl hydroxycinnamates. *Eur. J. Med. Chem.* **2011***, 46*, 773-777.

(27) Rajasekhar Pullabhotla, V. S. R.; Rahman, A.; Jonnalagadda, S. B. Selective catalytic Knoevenagel condensation by Ni–SiO_2 supported heterogeneous catalysts: An environmentally benign approach. *Catal. Commun.* **2009***, 10*, 365-369.

(28) Wen, L.; Ji, C.; Li, Y.; Li, M. Application of β-(2-Chloroaroyl)thioacetanilide in Synthesis(III): An Efficient Three-Component Synthesis of Thiochromeno[2,3-b]pyridines Catalyzed by KF/Neutral Al_2O_3 Co-operated with PEG 6000 under Microwave Irradiation. *J. Comb. Chem.* **2009***, 11, 799-805.*

(29) Reddy, B. M.; Patil, M. K.; Rao, K. N.; Reddy, G. K. An easy-to-use heterogeneous promoted zirconia catalyst for Knoevenagel condensation in liquid phase under solvent-free conditions. *J. Mol.Cat. A-Chem.* **2006***, 258*, 302-307.

(30) Bennazha, J.; Zahouily, M.; Sebti, S.; Boukhari, A.; Holt, E. M. $Na_2CaP_2O_7$, a new catalyst for Knoevenagel reaction. *Catal. Commun.* **2001***, 2*, 101-104.

(31) Reddy, T. I.; Varma, R. S. Rare-earth (RE) exchanged NaY zeolite promoted knoevenagel condensation. *Tetrahedron Lett.* **1997***, 38*, 1721-1724.

(32) Kantam, M.L.; Choudary, B.M.; Reddy, C.V.; Rao, K.K.; K.; Figueras, F. Aldol and Knoevenagel condensations catalysed by modified Mg-Al hydrotalcite: a solid base as catalyst useful in synthetic organic chemistry. *Chem. Commun.* **1998**, 1033-1034.

(33) Wada, S.; Suzuki, H. Calcite and fluorite as catalyst for the Knövenagel condensation of malononitrile and methyl cyanoacetate under solvent-free conditions. *Tetrahedron Lett.* **2003***, 44*, 399-401.

(34) Bigi, F.; Chesini, L.; Maggi, R.; Sartori, G. Montmorillonite KSF as an Inorganic, Water Stable, and Reusable Catalyst for the Knoevenagel Synthesis of Coumarin-3-carboxylic Acids. *J. Org. Chem.* **1999,** *64,* 1033-1035.

(35) Ge´raud, E.; Pre´vot, V.; Ghanbaja, J.; Leroux, F. Macroscopically Ordered Hydrotalcite-Type Materials Using Self-Assembled Colloidal Crystal Template. *Chem. Mater.* **2006,** *18,* 238-240.

(36) Halma, M.; Castro,Kelly Aparecida Dias de Freitas; Prévot, V.; Forano, C.; Wypych, F.; Nakagaki, S. Immobilization of anionic iron(III) porphyrins into ordered macroporous layered double hydroxides and investigation of catalytic activity in oxidation reactions. *J. Mol.Cat. A-Chem.* **2009***, 310*, 42-50.

(37) Pal, N.; Bhaumik, A. Soft templating strategies for the synthesis of mesoporous materials: Inorganic, organic–inorganic hybrid and purely organic solids. *Adv. Colloid Interfac.* **2013***, 189-190*, 21-41.

(38) Soler-Illia, G. J. d. A. A.; Crepaldi, E. L.; Grosso, D.; Sanchez, C. Block copolymer-templated mesoporous oxides. *Curr. Opin. Colloid In.* **2003***, 8*, 109-126.

(39) Flodström, K.; Alfredsson, V. Influence of the block length of triblock copolymers on the formation of mesoporous silica. *Microporous and Mesoporous Mater.* **2003***, 59*, 167-176.

(40) Tang, F.; Li, L.; Chen, D. Mesoporous Silica Nanoparticles: Synthesis, Biocompatibility and Drug Delivery. *Adv. Mater.* **2012***, 24*, 1504-1534.

(41) Pahalagedara, L.; Sharma, H.; Kuo, C-H.; Dharmarathna, D.; Joshi, A.; Suib, S.L.; Mhadeshwar, A.B., Structure and Oxidation Activity Correlations for Carbon Blacks and Diesel Soot. *Energy Fuels* **2012**, 26, 6757–6764.

(42) Poyraz, A.S.; Kuo, C-H.; Biswas, S.; King'ondu, C.K.; Suib, S.L. A general approach to crystalline and monomodal pore size mesoporous materials. *Nat. Commun.* **2013**, 4, 3952, 1-10.

(43) Yang, P.; Zhao, D.; Margolese, D.I.; Chmelka, B.F.; Stucky, G.D. Block Copolymer Templating Syntheses of Mesoporous Metal Oxides with Large Ordering Lengths and Semicrystalline Framework. *Chem. Mater.* **1999,** *11,* 2813-2826.

(44) Xia, Y.; Mokaya, R. Surfactant Mediated Control of Pore Size and Morphology for Molecularly Ordered Ethylene-Bridged Periodic Mesoporous Organosilica. *J. Phys. Chem. B* **2006**, *110,* 3889-3894.

(45) Ganguly, A; Ahmad, T.; Ganguli, A.K. Silica Mesostructures: Control of Pore Size and Surface Area Using a Surfactant-Templated Hydrothermal Process. *Langmuir* **2010**, 26, 14901–14908.

(46) Shih, K.; Leckie, J. O. Nickel aluminate spinel formation during sintering of simulated Ni-laden sludge and kaolinite. *J. Eur.Ceram. Soc.* **2007***, 27*, 91-99.

(47) Chen, Y.; Lee, C.; Yeng, M.; Chiu, H. The effect of calcination temperature on the crystallinity of TiO_2 nanopowders. *J. Cryst. Growth* **2003***, 247*, 363-370.

(48) J Li, X.; Xiao, W.; He, G.; Zheng, W.; Yu, N.; Tan, M. Pore size and surface area control of MgO nanostructures using a surfactant-templated hydrothermal process: High adsorption capability to azo dyes. *Colloid surface A* **2012***, 408*, 79-86.

(49) Grosman, A.; Ortega, C. Capillary Condensation in Porous Materials. Hysteresis and Interaction Mechanism without Pore Blocking/Percolation Process. *Langmuir* **2008**, *24*, 3977–3986.

(50) Alexander, S.; de Vos, W.M.; Castle, T.C.; Cosgrove, T.; Prescott, S.W. Growth and Shrinkage of Pluronic Micelles by Uptake and Release of Flurbiprofen: Variation of pH. *Langmuir* **2012**, *28*, 6539−6545.

(51) Alargova, R.G.; Danov, K.D.; Petkov, J.T.; Kralchevsky, P.A.; Broze, G.; Mehreteab, A. Sphere-to-Rod Transition in the Shape of Anionic Surfactant Micelles Determined by Surface Tension Measurements. *Langmuir* **1997,** *13,* 5544-5551.

(52) Pileni, M-P. The role of soft colloidal templates in controlling the size and shape of inorganic nanocrystals. *Nature Materials* **2003**, 2, 145 – 150.

(53) Ghampson, I. T.; Newman, C.; Kong, L.; Pier, E.; Hurley, K. D.; Pollock, R. A.; Walsh, B. R.; Goundie, B.; Wright, J.; Wheeler, M. C.; Meulenberg, R. W.; DeSisto, W. J.; Frederick, B. G.; Austin, R. N. Effects of pore diameter on particle size, phase, and turnover frequency in mesoporous silica supported cobalt Fischer-Tropsch catalysts. *Appl. Catal. A-Gen.* **2010***, 388*, 57-67.

(54) Sakatani, Y.; Grosso, D.; Nicole, L.; Boissiere, C.; Soler-Illia,G.J.; Sanchez, C. Optimised photocatalytic activity of grid-like mesoporous TiO_2 films: effect of crystallinity, pore size distribution, and pore accessibility. *J. Mater. Chem.* **2006**, 16, 77–82.

(55) Goettmann, F.; Sanchez, C. How does confinement affect the catalytic activity of mesoporous materials*. J. Mater. Chem.* **2007,** 17, 24–30.

(56) Iwamoto, M.; Tanaka, Y.; Sawamura, N.; Namba, S. Remarkable Effect of Pore Size on the Catalytic Activity of Mesoporous Silica for the Acetalization of Cyclohexanone with Methanol. *J. Am. Chem. Soc.* **2003**, 125, 13032-13033.

(57) Wong, E.M.; Hoertz, P.G.; Liang, C.J.; Shi, B.; Meyer, G.J.; Searson, P.C.Influence of Organic Capping Ligands on the Growth Kinetics of ZnO Nanoparticles. *Langmuir* **2001,** *17,* 8362-8367.

(58) Senapati, S.; Srivastava, S.K.; Singh, S.B.; Biswas, K. Capping Agent Assisted and Ag-Catalyzed Growth of Ni Nanoflowers. *Cryst.Growth Des.* 4068-4075.

(59) Parida, K. M.; Rath, D. Amine functionalized MCM-41: An active and reusable catalyst for Knoevenagel condensation reaction. *J. Mol. Catal. A-Chem.* **2009***, 310*, 93-100.

(60) Liu, Q.; Ai, H.; Li, Z. Potassium sorbate as an efficient and green catalyst for Knoevenagel condensation. *Ultrason. Sonochem.* **2011***, 18*, 477-479.

CHAPTER II. REMOVAL OF AZO DYES: INTERCALATION INTO SONOCHEMICALLY SYNTHESIZED NiAl LAYERED DOUBLE HYDROXIDE.

2.1. Introduction

Dyes can be classified into three main groups as anionic (direct, acid, and reactive dyes), cationic (basic dyes) and non-ionic dyes (disperse dyes).[1] Among these, removal of reactive dye from wastewater is very difficult since they are highly soluble in water.[2] An excessive amount of reactive dyes are widely used in different industries such as textile, printing, plastic, cosmetics, paper, leather, pharmaceutical, and food. Reactive dyes have a synthetic origin with a complex aromatic and heterocyclic molecular structure. Most of them are azo compounds that are linked by an azo bridge and this structure is responsible for the intense color and makes the dye more stable and more difficult to biodegrade.[2] Approximately 7×10^5 tons of dyes are discharged into waste streams annually and these dye contaminated wastewaters have become major environmental pollutants. When these dyes are discharged into aquatic systems without adequate treatment, they may significantly damage the plants and living beings, both aquatic and terrestrial.[1,3] The bright colors of these dyes directly affect the photosynthetic cycle in aquatic systems by reducing the light penetration capacity. In addition, many reactive dyes and their breakdown products are

toxic, carcinogenic or mutagenic to life forms.[4,5,6] Therefore it is important to develop efficient techniques to remove dye pollutants found in wastewaters.

Several techniques have been employed for the removal of colored dye from wastewater systems. The most widely used methods include biological treatment, [7] coagulation,[8] chemical oxidation, [9,10] ozonation, [11] membrane filtration, [12,13] ion-exchange methods, [14] photocatalysis,[15] and adsorption. [16,17] Although they have been widely used, these methods suffer from several limitations. Efficiency of dye degradation using biological processes is less due to their complex structures, molecular size and nature of dye molecules. Even though chemical and other advanced oxidation processes are effective for very low concentrations of organic dye wastes, these methods are too expensive and complex.[10] In addition, some of these methods can produce different by-products with carcinogenic or toxic properties.[7]

Among all these techniques for dye removal from industrial effluents, the adsorption process is very reliable due to its simplicity, ease of operation, economic feasibility, high efficiency, and recyclability of adsorbents as well as the availability of a wide range of adsorbents.[8,18,19] Therefore, adsorption can be considered as the most efficient technique for the removal of synthetic dyes due to removal of complete dye molecule from aqueous effluents, unlike other methods, which destroy only the dye chromophore leaving the harmful residues.[20] Various types of absorbents have been proposed for the removal of dyes from aqueous solutions. Adsorption on activated carbon is an effective process but is not economically desirable.[19] Fly ash,[18] zeolites,[21] polymers,[22] and

clays[23] are alternative candidates as adsorbents. However, it is important to develop effective, readily available, reusable, and economically feasible adsorbents with high adsorption capacities and removal efficiencies for practical applications.

Among all these adsorbents hydrotalcite-like compounds or layered double hydroxides (LDHs), can be considered as environmentally benign, effective adsorbents for the removal of dye molecules due to unique hydrophobic and anion exchange properties.[24,25,26] LDHs, well-known as anionic clays, are a large class of natural and synthetic inorganic lamellar compounds, which have been extensively studied in recent years due to their potential applications in different fields.[27] These materials are widely used as anion exchangers,[28] adsorbents,[29] catalysts and catalyst supports,[30] drug and catalyst carriers,[31] anticorrosion agents,[32] and electrode materials.[33,34]

Composition of the LDH materials can be represented by the general formula $[M_{1-x}^{2+}M_x^{3+}(OH)_2]^{x+}(A^{n-})_{x/n} \cdot mH_2O$, where M^{2+} and M^{3+} are divalent metal cations (Ca^{2+}, Mg^{2+}, Zn^{2+}, Cu^{2+}, Ni^{2+}, Co^{2+}, etc.) and trivalent metal cations (Al^{3+}, Fe^{3+}, Ga^{3+}, Cr^{3+}, etc) respectively. The cations occupy the octahedral sites within the hydroxide layers, *x* is the molar ratio between divalent and trivalent cations $M^{3+}/ (M^{2+}+M^{3+})$ while A^{n-} (Cl^-, Br^-, I^-, OH^-, NO_3^-, SO_4^{2-}, etc.) is the interlayer anion with charge *n*.[34,35] Since their interlayer anions can easily be replaced with other anions, LDHs are considered as good anion exchangers. The composition of these materials can also be varied over a wide range depending upon the type of metal cations and interlayer anions.[36] Various LDH materials with different

physicochemical properties can be synthesized with several preparation methods such as co-precipitation,[37] urea hydrolysis,[38] ion-exchange method,[39] rehydration/ reconstruction,[40] hydrothermal method,[41] and ultrasound irradiation.[42]

In the present work we have used ultrasonic irradiation for the preparation of NiAl-LDH with enhanced crystal qualities with a uniform size distribution and a higher surface area compared to the materials synthesized from conventional methods. Recently sonochemical techniques have been widely used for the synthesis of different organic and inorganic compounds in order to reach very high temperatures and pressures within a short period of time. When the reaction medium is irradiated with ultrasound, micro bubbles are formed due to the rapid movement of fluids. These oscillating bubbles are capable of gathering ultrasonic energy and they collapse forming high pressure and high temperature conditions in the medium.[43-45] Sonochemical synthesis lowers reaction times and temperatures significantly while controlling the particle size of the material.[46]

The objectives of this work were to prepare NiAl-LDH using ultrasonic-assisted synthesis and study the effects of as synthesized material and the calcined materials on the removal of anionic reactive dye RBV-5r from aqueous solution (Figure 2.1). The effects of various parameters such as calcination temperature, contact time, initial dye concentration, pH of the solution and reaction temperature on the degree of adsorption were examined. The reusability of the absorbent for the removal of the reactive dye has also been evaluated. The adsorption process of the dye was examined by X-ray diffraction (XRD),

Fourier transformation infrared spectroscopy (FTIR) as well as by computer simulations. The interlayer structure, arrangement, and orientation of the intercalated RBV-5r into the Ni:Al = 3:1 LDH system were studied using molecular dynamics (MD) simulations.[47]

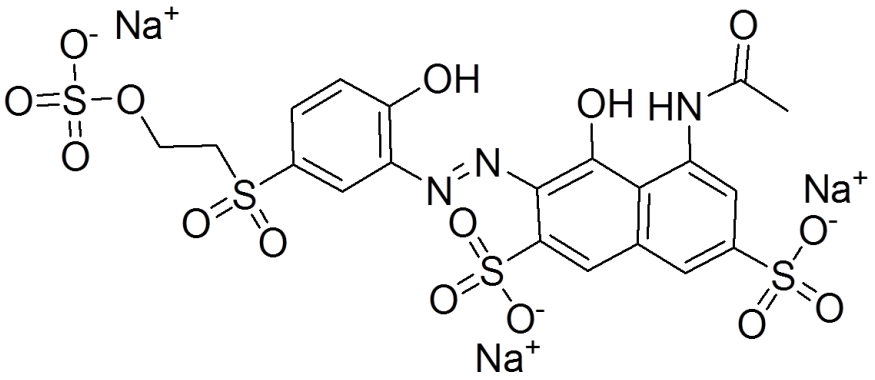

Figure 2.1. Chemical structure of Remazol Brilliant Violet (RBV-5r)

2.2. Experimental

2.2.1. Materials

Nickel nitrate hexahydrate ($Ni(NO_3)_2 \cdot 6H_2O$), aluminum nitrate nonahydrate ($Al(NO_3)_3 \cdot 9H_2O$), ammonium hydroxide (NH_4OH), sodium nitrate ($NaNO_3$), sodium hydroxide (NaOH), hydrochloric acid (HCl), and RBV-5r ($C_{20}H_{16}N_3Na_3O_{15}S_4$) were purchased from Sigma-Aldrich and were used without further purification. Double distilled water (DDW) was used in all experiments.

2.2.2. Synthesis of NiAl-LDH

A co-precipitation method was employed under controlled pH conditions, followed by ultrasound irradiation which was used to prepare NiAl-LDH with a molar ratio of Ni^{2+}/Al^{3+} = 3. The samples were synthesized by adding 1.5 mmol

$Ni(NO_3)_2 \cdot 6H_2O$ and 0.5 mmol $Al(NO_3)_3 \cdot 9H_2O$ into 30 mL deionized water under vigorous stirring at room temperature. The final pH of the reaction mixture was adjusted to 10.0 with ammonium hydroxide solution. The resultant mixture was immediately subjected to ultrasonic irradiation at 65˚C for 1 h in a Branson 3210 ultrasonic bath equipped with a heater. After irradiation, the apple green colored solid was filtered and washed with distilled water to remove excess free ions until the pH of the filtrate was 7. The washed precipitate was dried at 60˚C overnight, and the product was named $NiAl\text{-}LDH_{SC}$.

2.2.3. Structural characterization of NiAl-LDH and its calcined derivatives

2.2.3.1. X-Ray Powder Diffraction Studies

Powder X-ray diffraction (PXRD) patterns of synthesized LDHs, calcined LDHs, and dye adsorbed materials were obtained using a Rigaku Ultima IV diffractometer using Cu Kα(λ = 0.15406 nm) radiation. The beam voltage and beam current were set at 40 kV and 44 mA. Continuous scans were taken in a 2θ range of 5 to 75˚ with a scan rate of 2.0˚/min, and the phases were identified using the International Center for Diffraction Data (ICDD) database. Determination of particle sizes of the LDH materials was done using the Debye-Scherer equation for the peaks corresponding to (003) and (110) planes.

2.2.3.2. Scanning Electron Microscopy

The surface morphologies of the synthesized materials were studied using field emission scanning electron microscopy (FE-SEM) on a Zeiss DSM 982 Gemini instrument with a Schottky emitter at an accelerating voltage of 2.0 kV with a beam current of 1.0 mA. The samples were ultrasonically dispersed in ethanol and deposited on Au-coated silicon chips prior to the analysis.

2.2.3.3. Transmission Electron Microscopy

The surface morphologies and the crystalline structures of the LDH material were examined by the high-resolution transmission electron microscopy (HR-TEM). Experiments were performed using a JEOL 2010 instrument within accelerating voltage of 200 kV. The samples were prepared by dispersing the material in ethanol. Then a drop of the dispersion was placed on a carbon coated copper grid and allowed to dry before analysis.

2.2.3.4. N_2 Sorption Studies

The surface area (SA) and pore size distribution measurements were obtained with a Quantachrome Autosorb iQ_2 instrument. N_2 gas was used as the adsorbate at 77 K. The Brunauer- Emmett-Teller (BET) method was used to measure the surface area by a multipoint method and the Barrett-Joyner-Halenda (BJH) desorption method was used to calculate the pore size distribution. Samples were degassed at 120˚C for 12 hours in order to remove any adsorbed species before analysis.

2.2.3.5. Fourier Transformation infra Red (FT-IR) Spectroscopy

Fourier transform infrared (FTIR) spectroscopy experiments were performed using a Thermo-Scientific Nicolet FT-IR Model 8700 (in the range 4000−400 cm^{-1}) equipped with a DTGS detector and a KBr beam splitter. Spectra were collected with a resolution of 4 cm^{-1} using 250 scans.

2.2.3.6. Thermo Gravimetric Analysis

Thermal stability studies of the materials were studied by thermogravimetric analysis (TGA) using a Hi-Res TA Instruments Model 2950, in the temperature range between 25 and 900˚C at a heating rate of 10 ˚C/min under a nitrogen atmosphere.

2.2.4. Dye adsorption and desorption experiments

The calibration curve for the dye (RBV-5r) was prepared by measuring the absorbance values for a series of known concentrations of dye solutions at the wavelength of maximum absorbance (λ = 560 nm). Batch adsorption experiments were carried out in order to study the sorption kinetics of RBV-5r on NiAl- LDH and its calcined derivatives by adding 100 mg of each sorbent into 100 mL of RBV-5r solution with a concentration of 150 mg/ L. The mixture was stirred at room temperature and samples of the reaction mixture were withdrawn at desired time intervals ranging from 2 to 60 minutes during the adsorption process. The

adsorbent was separated from the solution by filtration and the equilibrium dye concentration was determined at 560 nm using a UV/vis spectrophotometer (Shimadzu UV/vis 2450 Spectrophotometer).

The effect of parameters such as pH of the solution, adsorption temperature, contact time, and initial dye concentration were studied. The adsorption capacity of NiAl-$C250_{SC}$ material was studied over a wide range of pH and optimum pH was selected as 6. Solutions of 0.1 M NaOH and 0.1 M HCl were used for the pH adjustments. The dye removal efficiency (DRE) and the amount of dye taken up are calculated according to equations (1) and (2), respectively.

Dye removal efficiency (%) $= [(C_0 - C_e) / C_0] \times 100\%$ (1)

Adsorption capacity (q_e) $= (C_0 - C_e) \times V / W$ (2)

where C_0 and C_e are RBV-5r concentrations in mg/L at initial and equilibrium states respectively. V is the volume of solution in L, W is the mass of the dry adsorbent in g, and q_e is adsorption capacity in mg/g.

Desorption of RBV-5r from the adsorbent was studied by subjecting the adsorbent to an anion exchange process. Dye loaded LDH material (50.00 mg) was stirred in an aqueous solution of sodium nitrate for a period of 24 h. The resulting material was calcined at 250˚C for 2 h and subjected to a new adsorption cycle in order to study the reusability of the catalyst.

2.2.5. Computational methods

All simulations were performed using DL_Poly classic (version 1.8)[48] MD code. The LDH model was constructed using atomic coordinates from the previously reported crystal structure of the hydrotalcite unit cell,[47] $Mg_6Al_2(CO_3)(OH)_{16}.4H_2O$ in the 3 2/m space group and lattice parameters $a = b = 9.44$ Å $c = 24.33$ Å. The interlayer carbonate ions and water were removed from the structure and all Mg^{2+} ions were replaced by Ni^{2+} ions. A supercell was created containing 50 hydrotalcite crystallographic unit cells. The supercell parameters were $a = b = 47.21$ Å, $c = 48.67$ Å; $\alpha = \beta = 90.0°$ and $\gamma = 120.0°$ (5 × 5 × 2 repeats in the *a*, *b* and *c* directions, respectively) .

The calculations were carried out in two steps. First an integral number of nitrate ions was introduced between the NiAl-LDH layers so that overall charge neutrality was maintained. Then water molecules were added according to the experimental TGA data. Then interlayer properties were calculated for the nitrate-NiAl-LDH system from the MD simulations.

To study the dye intercalated NiAl-LDH, eight dye molecules; two per interlayer were added by replacing the nitrate ions maintaining the charge neutrality and amount of water. The dye molecules were added in such a way that their longest axis oriented approximately parallel to the normal interlayer in a layer like arrangement. LDH and water molecules were modeled using the parameters derived in the CLAYFF[49] which has been previously used for modeling interactions between organic molecules and clays. Dye molecules and

nitrates were modeled using the OPLS-AA[50] force field. Partial charges for the dye were derived using the RESP[51] method at the DFT/B3LYP/6-31g* level of theory.

Non bonded potential interactions consisted of long range coulombic interactions and short range van der waals interactions. Coulombic interactions were computed using the ewald summation method and van der Waals interactions were treated with a cutoff radius of 12.0 Å. Molecular dynamics simulations were performed on a NPT ensemble at 298 K and 1 atm. A time step of 0.001 ps was used. PBC conditions were used to simulate the bulk nature of the clay. Nitrate NiAl-LDH system was equilibriated for 200 ps followed by a 200 ps simulation time. Dye NiAl-LDH was equilibriated for 400 ps followed by a 200 ps simulation time.

2.3. Results

2.3.1. Characterization of as-synthesized NiAl-LDH and its calcined derivatives

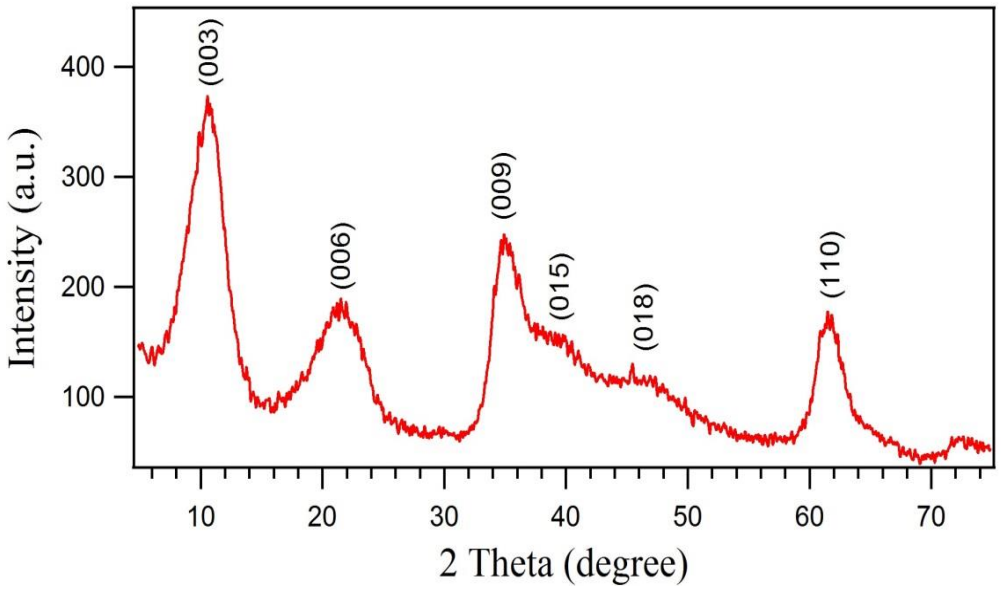

Figure 2.2. X-ray diffraction pattern of as-synthesized NiAl-$LDH_{SC.}$ A series of (00*l*) symmetric peaks indexed as (003), (006), and (009) at low 2θ angle resemble the basal spacing, indicating an ordered stacking arrangement.

The crystalline structure of the prepared NiAl-LDH was determined by XRD. Figure 2.2 shows the XRD pattern of as-synthesized NiAl-LDH_{SC}. Characteristic sharp diffraction peaks were indexed as (003), (006) and (009) and broad asymmetric peaks were indexed as (015) and (018). Peaks corresponding to (110) and (113) planes were merged into a single peak due to the amorphous nature of the material. The (003) and (006) reflections of the NiAl-LDH_{SC} crystal phase appeared at 10.9˚ and 21.1˚ respectively. A series of (00*l*) symmetric peaks indexed as (003), (006), and (009) at low 2θ angle resemble the basal spacing, indicating an ordered stacking arrangement. The basal d-spacing value of the NiAl-LDH_{SC} was calculated as 8.13 Å from Bragg's equation (Table 2.1).

Table 2.1. Unit cell parameters and average crystallite sizes of NiAl-LDH_{SC} and NiAl-LDH_{REF}.

Sample	Unit cell parameters [a](Å)		Basal d-spacing (Å)	Crystallite size [b](Å)	
	a	*c*		L_{003}	L_{110}
NiAl-LDH_{SC}	3.01	24.39	8.13	23.77	35.18
NiAl-LDH_{REF}	3.01	24.33	8.11	32.04	38.02

The average crystallite size (L) was calculated for NiAl-LDH_{SC} and NiAl-LDH_{REF} using (003) and (110) reflections, according to the Debye-Scherrer equation, $L = 0.89\lambda/\beta(\theta)\cos\theta$ where L is the crystallite size, λ is the wavelength of the radiation used, θ is the Bragg diffraction angle, and β(θ) is the full width at half maximum (Table 2.1). The lattice parameters *a* and *c* can be calculated from the positions of the (003) and (110) reflections assuming a 3R stacking of the layers, that is $a = 2d_{110}$ and $c = 3d_{003}$ (Table 2.1). The unit cell parameter *a* is the average cation–cation distance inside the brucite-like layers while the *c* parameter, which is related to the interlayer thickness, is governed by the average charge of the metal cations, the nature of the interlayer anion, and the water content.

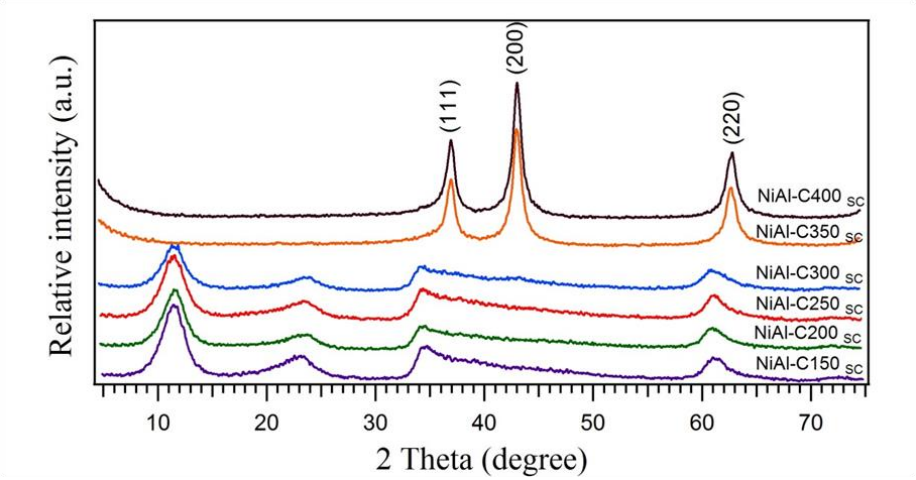

Figure 2.3. X-ray diffraction patterns of NiAl-LDH_{SC} calcined at different temperatures. After 350˚C, the layered structure of the original LDHs is completely destroyed and forms nickel oxide (NiO) peaks, signifying the decomposition of the original LDHs.

Figure 2.3 shows the XRD patterns of the samples calcined at different temperatures for 2 h. The initial layered structure is retained up to 300˚C, but (003) and (006) peaks are slightly shifted towards higher 2θ values upon increasing the calcination temperature. When the material is calcined above 350˚C, the layered structure of the original LDHs is completely destroyed and indicates only nickel oxide (NiO) peaks, signifying the decomposition of the original LDHs.

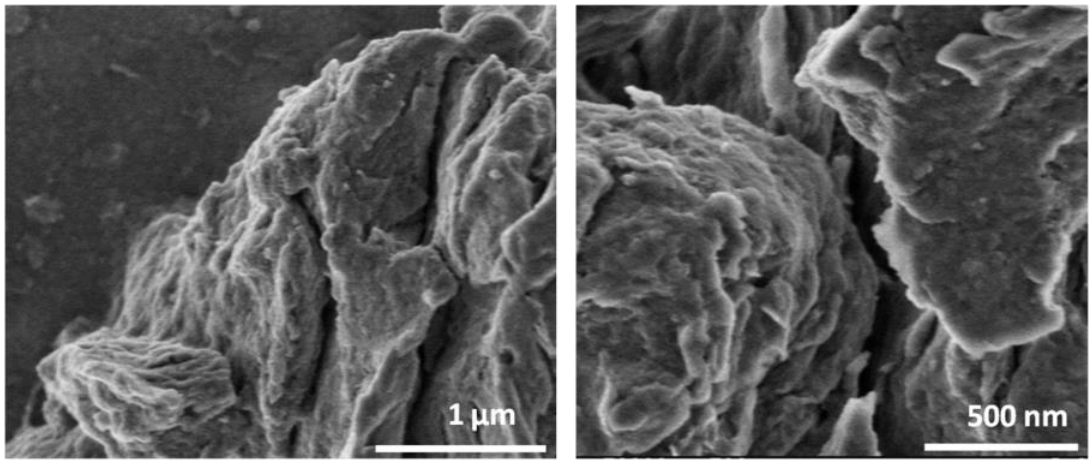

Figure 2.4. Field emission scanning electron microscopy (FESEM) images of NiAl-LDH_{SC} showing rough plate-like surface morphology with serrated edges.

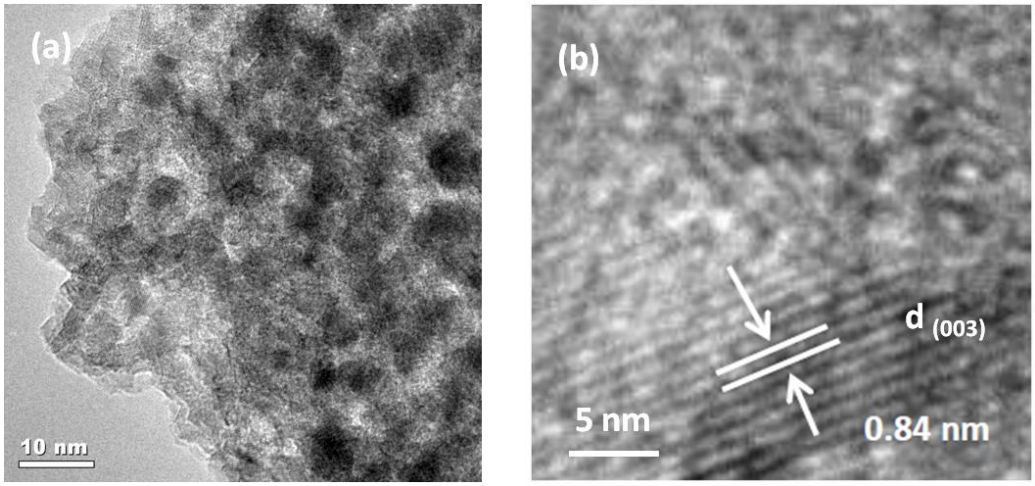

Figure 2.5. TEM and HRTEM images of NiAl-LDH_{SC} (a) Low magnification image showing the morphology of NiAl-LDH_{SC} (b) lattice fringes of (003) plane.

The morphology of the NiAl-LDH_{SC} material was examined by SEM. A rough plate-like surface morphology with serrated edges was observed and these plate-like LDH sheets are arranged perpendicularly on the surface.

Particles are appeared as fine granular agglomerates (Figure 2.4). The TEM images of NiAl-LDH_{SC} show the local ordering of the brucite-type layers giving non-uniform irregular shaped aggregates (Figure 2.5a). HR-TEM shows the lattice fringes with a d spacing of 0.84 nm, which can be indexed to the (003) plane of NiAl-LDH_{SC} material.

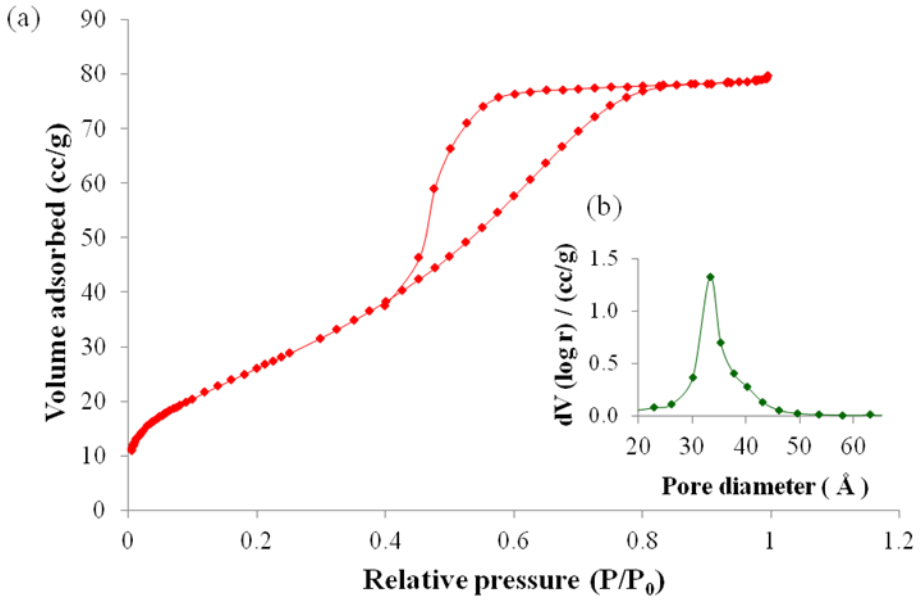

Figure 2.6. (a) N_2 adsorption/desorption isotherms of NiAl-$C250_{SC}$ (b) Barrett-Joyner-Halenda (BJH) desorption pore size distribution curve of NiAl-$C250_{SC.}$

A N_2 sorption isotherm and the pore size distribution of the NiAl-$C250_{SC}$ sample are shown in Figure 2.6. The isotherm exhibits a typical IUPAC type IV pattern corresponding to a type H2 hysteresis loop, indicating the existence of mesopores. The measurement gave a specific surface area of 97 m^2/g and an average pore diameter of 34 Å.

2.3.2. Dye removal efficiency

The experiments were carried out in order to study the efficiency of the removal of RBV-5r by NiAl-LDH_{SC} calcined at different temperatures. Effect of sorption time on RBV-5r removal by NiAl-CX_{SC} is shown in Figure 2.7a. The removal of dye by NiAl-$C150_{SC}$, NiAl-$C200_{SC}$ and NiAl-$C250_{SC}$ was rapid but the removal rate started decreasing when the calcination temperature was increased above 300 ˚C. The order of dye loading between the various sorbents was NiAl-$C250_{SC}$ > NiAl-$C200_{SC}$ > NiAl-$C150_{SC}$ > NiAl-$C300_{SC}$ > NiAl-$C350_{SC}$ > NiAl-$C400_{SC}$. The effect of the synthesis method was studied by comparing the dye removal efficiencies of NiAl-C250 synthesized by ultrasound irradiation and normal reflux methods. The adsorption rates of RBV-5r by those two materials are plotted in Figure 2.7b. The adsorption equilibrium time of NiAl-$C250_{SC}$ is shorter than that of NiAl-$C250_{REF}$. Figure 2.8 shows changes in the absorption spectra of a RBV-5r aqueous solution in the presence of NiAl-$C250_{SC}$. The removal rate is rapid and the sharp decrease indicates that NiAl-$C250_{SC}$ provided excellent removal of RBV-5r.

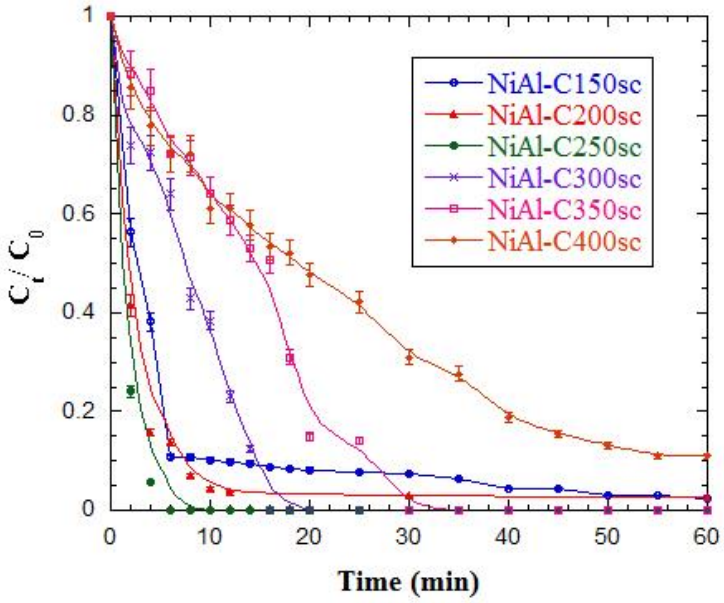

Figure 2.7a. Effect of contact time on the uptake of RBV-5r by NiAl-LDH_{SC} calcined at different temperatures. The removal of dye by NiAl-$C150_{SC}$, NiAl-$C200_{SC}$ and NiAl-$C250_{SC}$ was rapid compared to the samples calcined above 300 ˚C.

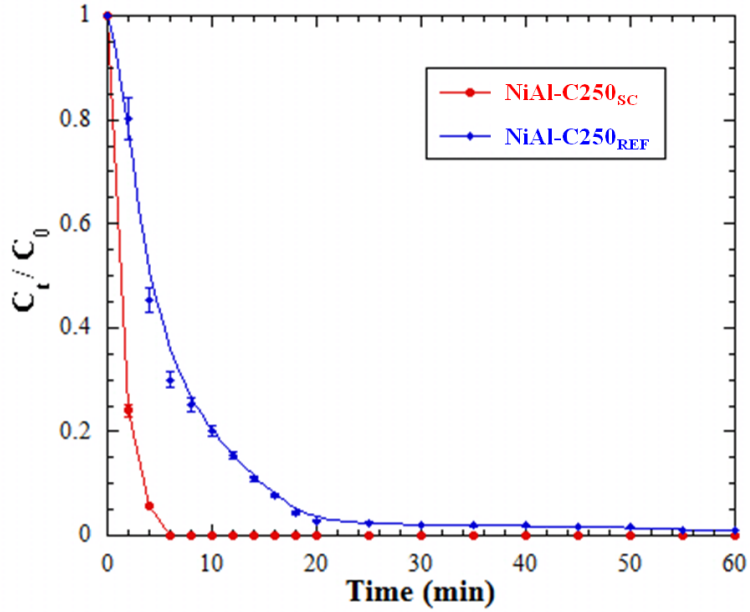

Figure 2.7b. Removal efficiency of RBV-5r by NiAl-C250$_{SC}$ and NiAl-C250$_{REF}$. The adsorption equilibrium time of NiAl-C250$_{SC}$ is shorter than adsorption equilibrium time of NiAl-C250$_{REF}$.

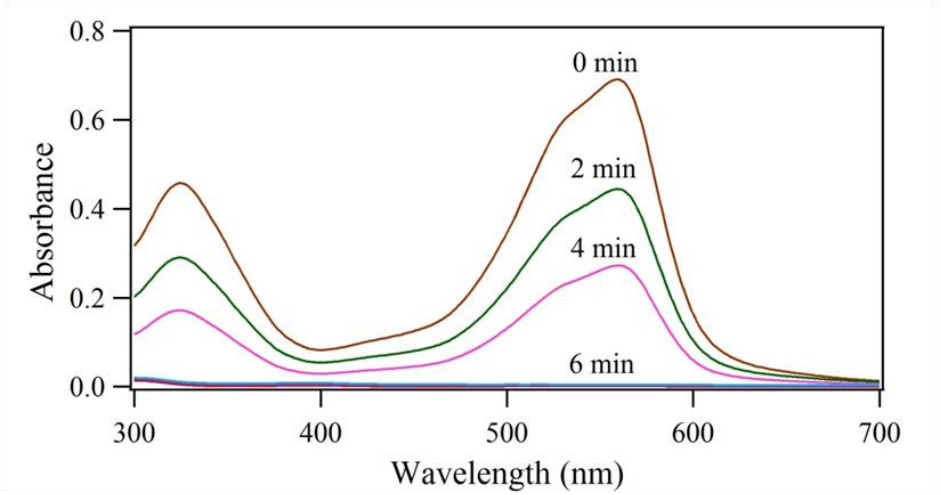

Figure 2.8. UV-Vis absorption spectral changes of RBV-5r mixed with NiAl-C250$_{SC}$. The rapid removal rate and the sharp decrease indicate the excellent activity of NiAl-C250$_{SC}$ in the removal of RBV-5r.

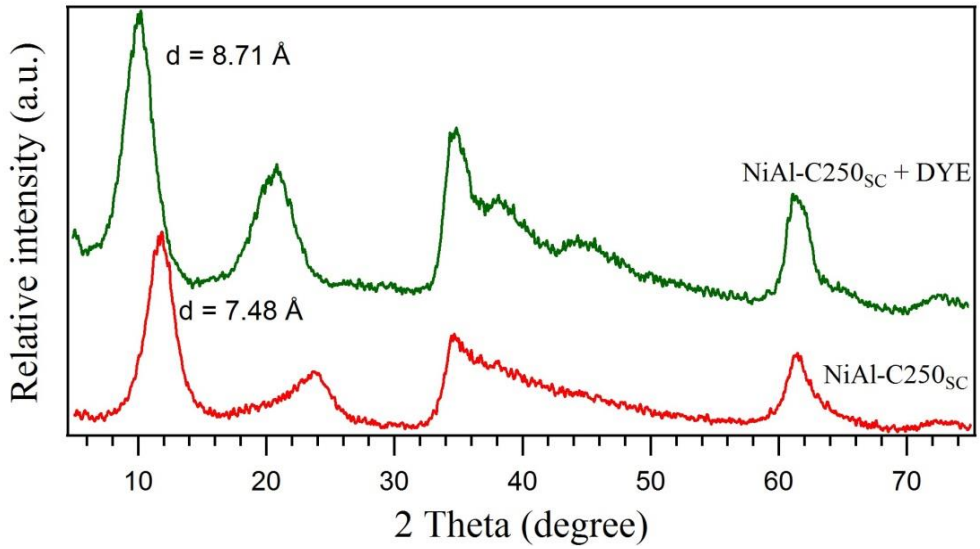

Figure 2.9. XRD patterns of NiAl-C250$_{SC}$ before and after dye adsorption. The d spacing value (d_{003}) of the material goes up from 7.48 Å to 8.71 Å after intercalation of the dye.

The XRD patterns (Figure 2.9) show the NiAl-C250$_{SC}$ before and after the adsorption of the dye. The original d-spacing value (d_{003}) of the material was 7.48 Å. After intercalation with the dye, the d_{003} spacing of the material was increased to 8.71 Å. Further evidence for the intercalation of the dye was provided by FTIR spectroscopy in the frequency range 4000-400 cm^{-1} (Figure 2.10). The broad and strong absorption peak between 3600 and 3300 cm^{-1} was due to the stretching vibration of structural -OH groups from the brucite-like layers and as well as from the interlayer water molecules. The peaks at 1150 and 1050 cm^{-1} correspond to the vibration of SO_3^{2-}. The peak at 1050 cm^{-1} resembles the intercalation of the SO_3^{2-} in the brucite-like sheets. Intercalated NO_3^- anions gave another strong absorption peak around 1386 cm^{-1} due to the bending vibrations of N-O. The intensity of the NO_3^- peak was reduced after the adsorption of the dye, indicating ion-exchange between NO_3^- and SO_3^{2-} in the dye molecule.

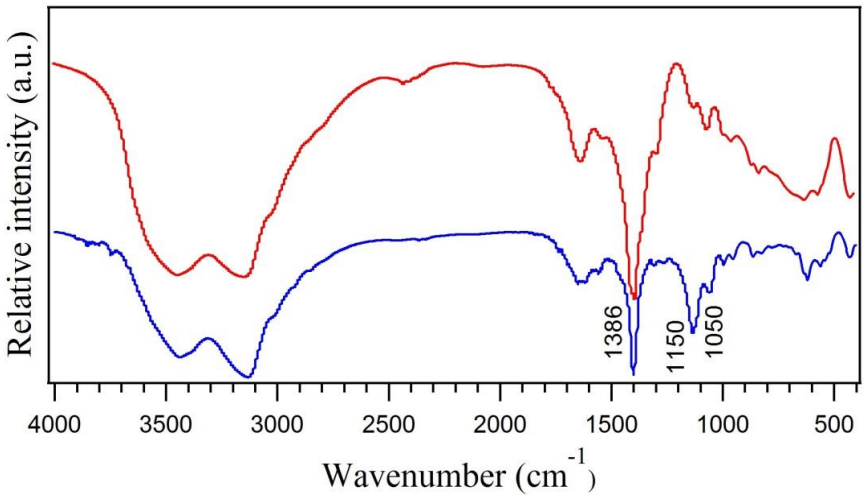

Figure 2.10 . FTIR spectra of (a) NiAl-C250$_{SC}$ (b) RBV-5r adsorbed NiAl-C250$_{SC}$. Appearance of peaks at 1150 and 1050 cm^{-1} and decrease in intensity of peak at 1386 cm^{-1} confirm the replacement of NO_3^- by SO_3^{2-} group containing RBV-5r molecules.

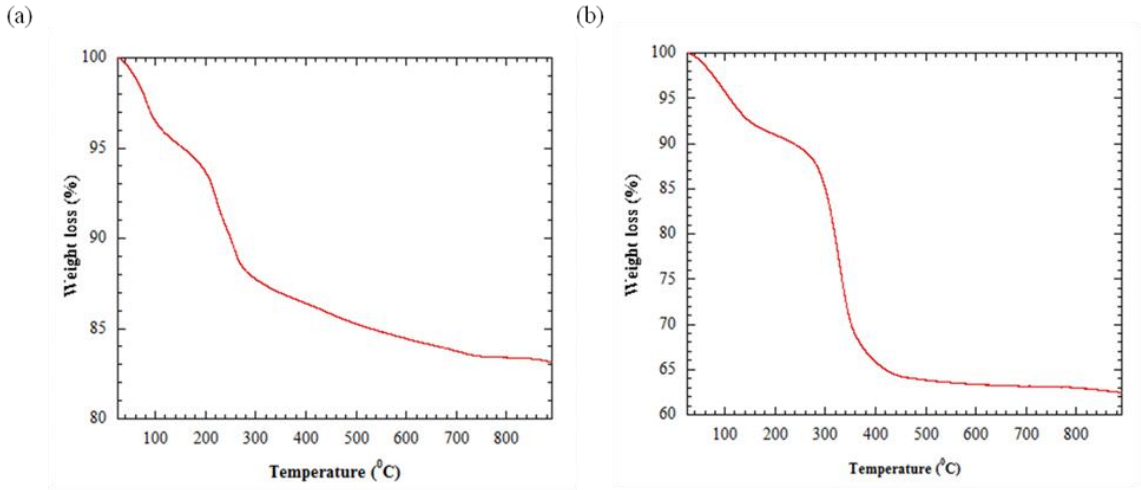

Figure 2.11. Thermogravimetric analysis profiles of (a) NiAl-LDH$_{SC}$ (b) RBV-5r adsorbed NiAl-C250$_{SC}$.

Figure 2.11 shows TGA analysis for the NiAl-LDH_{sc} and the RBV-5r adsorbed NiAl-$C250_{SC}$. Both the samples behaved similarly giving two distinct steps of weight losses. NiAl-LDH_{SC} gave the first weight loss between 50 and 150˚C and the second weight loss between 150 and 350˚C. Weight losses for RBV-5r adsorbed NiAl-$C250_{SC}$ were observed between 50 and 200˚C and 200 and 500˚C.

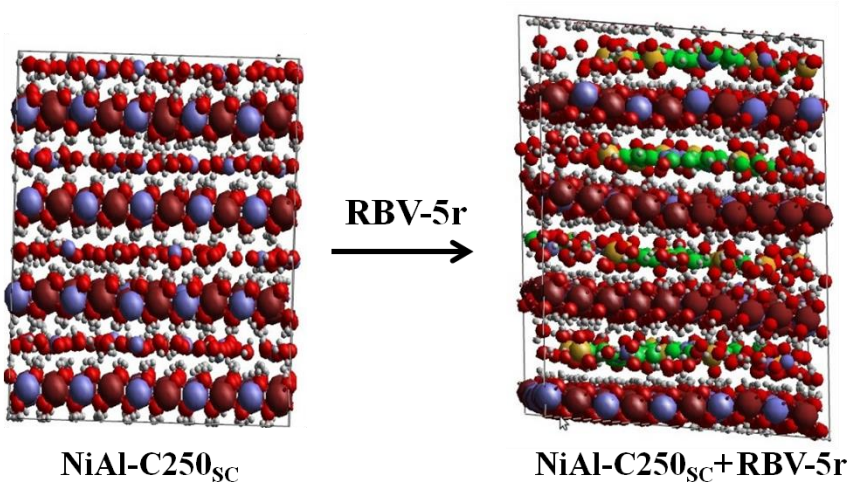

Figure 2.12a) Representative snapshots from MD simulations of NiAl-$C250_{SC}$ and RBV-5r intercalated NiAl-$C250_{SC}$ (not to scale) showing positions and orientations of the interlayer species : red-O, orange - Ni, gray - Al, white - H, yellow - S, brown - C, blue – N.

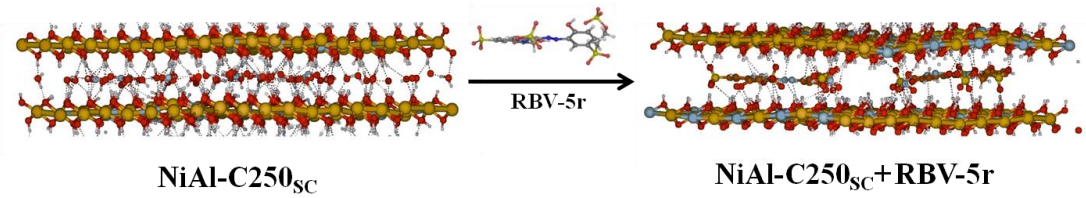

Figure 2.12b) Interlayer arrangements of NiAl-C250$_{SC}$ and RBV-5r intercalated NiAl-C250$_{SC}$ showing the orientation of dye molecules.

Molecular Dynamics (MD) simulation studies can be used to confirm the results obtained by XRD and FTIR techniques. Figure 2.12a and 2.12b give the snap shots obtained from MD simulations for the NiAl-C250$_{SC}$ before and after intercalation of the dye showing the equilibrium position of the anionic dye. According to MD simulation studies, the calculated d-spacing value was 7.59 Å for NiAl-C250$_{SC}$ material. After intercalation with the dye, the calculated d-spacing value increased to 8.75 Å, in very good agreement with the experimentally measured changes.

2.3.3. Effect of the pH, initial dye concentration and temperature on dye removal

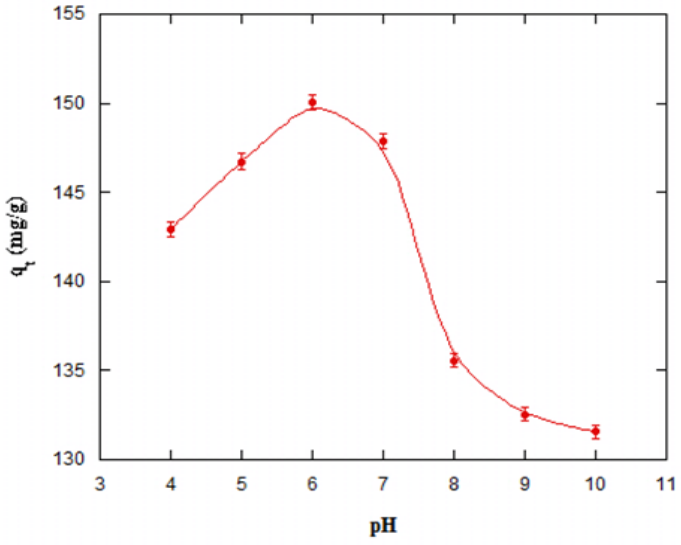

Figure 2.13. Effect of solution pH on adsorption capacity of NiAl-C250$_{SC.}$

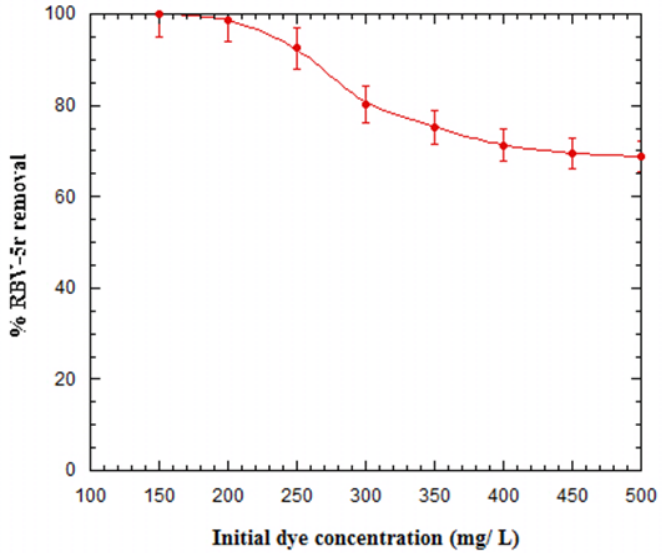

Figure 2.14. Effect of the initial dye concentration on adsorption capacity of NiAl-C250$_{SC.}$

The effect of the pH was studied for the adsorption of RBV-5r on NiAl-C250$_{SC}$ at room temperature. The study was done at different initial pH values ranging from 4.0 to 10.0 and the results are shown in Figure 2.13 for 150 mg/L solution. NiAl-C250$_{SC}$ was very efficient over a wide pH range and the removal efficiency was maximum at pH 6 with an adsorption capacity of 150 mg-dye/ g-sorbent. The removal efficiency of RBV-5r was determined by using various initial dye concentrations (150-450 ppm) in a fixed time (1 h). The results are shown in Figure 2.14. The percentage removal decreased with the increase in initial dye concentration. Removals of 100% and 98.8% were observed for 150 mg/L and 200 mg/L solutions, respectively. The rate of adsorption decreased with time until gradually approaching a plateau. The adsorption experiments were carried out at

three different temperatures 25, 45 and 65˚C, and the results are given in Figure 2.15. The adsorption capacity was increased with increasing temperature and the required time for the system to reach equilibrium was decreased. Adsorption experiments carried out at 45 and 65˚C showed the same capacity.

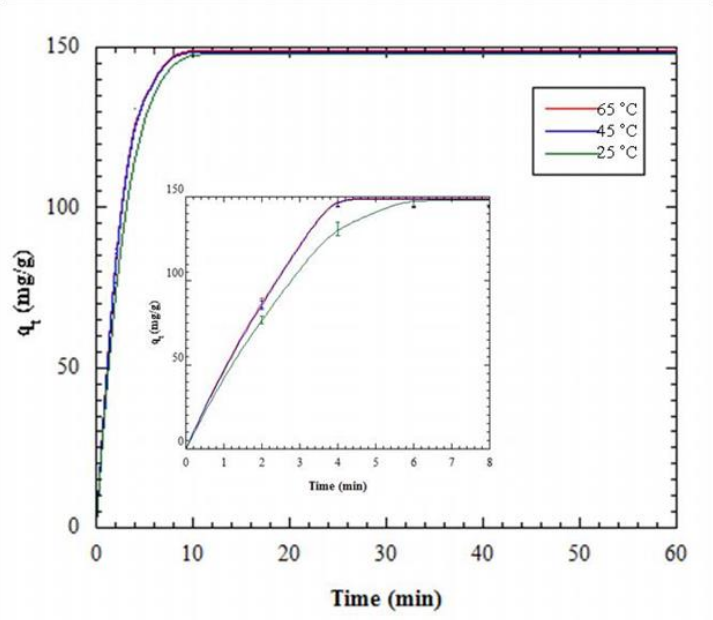

Figure 2.15. Effect of temperature on adsorption capacity of NiAl-C250$_{SC.}$

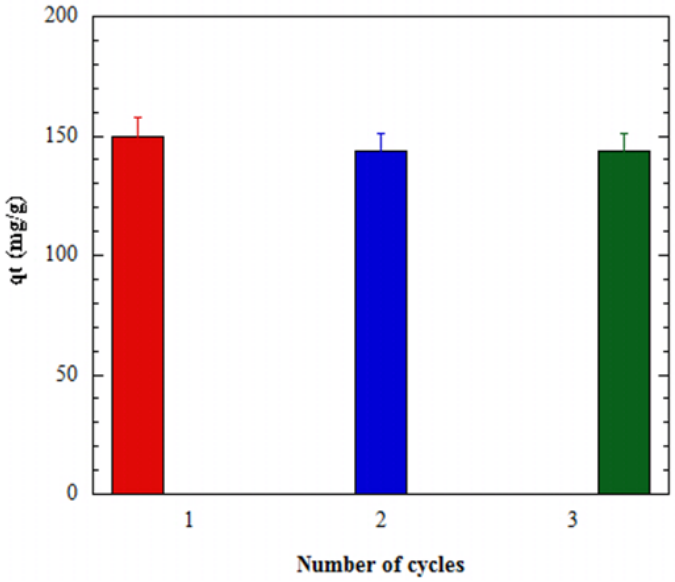

Figure 2.16. Adsorption-desorption cycles of NiAl-C250$_{SC}$ material.

Reusability of the spent adsorbent material was studied using an anion exchange process with a sodium nitrate solution. The material was tested for adsorption capacity in terms of reusability for consecutive three cycles, by applying the same calcined material at 25˚C and pH 6. According to Figure 2.16, the regenerated adsorbent showed 95.9%, and 95.7% of the initial adsorption capacity after the first and the second regeneration cycles, respectively.

2.4. Discussion

Sonochemically synthesized NiAl-LDH exhibited the XRD pattern of a typical LDH with the hydrotalcite-type structure, signifying the presence of an ordered stacking arrangement. Unit cell parameters and average crystallite sizes of NiAl-LDH$_{SC}$ and NiAl-LDH$_{REF}$ were calculated for the (003) reflection, using the Debye-Scherrer equation.[52,53] Table 1 shows a comparison of crystallite sizes for

NiAl-LDH_{SC} and NiAl-$LDH_{REF.}$ According to the observed results, NiAl-LDH synthesized in the presence of ultrasonic irradiation exhibit smaller crystallite sizes compared to the materials synthesized with regular reflux methods. Ultrasonic irradiation can lead to cavitation, in which bubbles form and collapse, creating local hot spots with extremely high temperatures and pressures. Thus, this technique can be considered as a powerful synthetic tool for the synthesis of materials with small crystallite sizes. [54,55]

When studying the efficiency of the removal of RBV-5r by NiAl-LDH_{SC} calcined at different temperatures, the sample calcined at 250˚C (NiAl-$C250_{SC}$) showed the best activity. Dye removal efficiencies of NiAl-C250 synthesized by ultrasonic irradiation and normal reflux methods were compared to study the effect of the synthesis method. According to Figure 2.7b, the adsorption equilibrium time of NiAl-$C250_{SC}$ is shorter than that of NiAl-$C250_{REF}$. This can be attributed to the small crystallite sizes of the samples synthesized by sonochemical methods. [54,55] Due to the smaller crystallite size, the diffusion resistance was reduced and a higher external surface area was obtained. Therefore, NiAl-LDH synthesized in the presence of ultrasonic irradiation gives higher removal efficiency for the reactive dye than those synthesized with regular reflux methods.

The adsorption capacity of the material is decreased upon increasing the pH. This may be due to the competitive binding of OH^- groups and sulfonate groups on the LDH material. The lower adsorption capacity at lower pH may be due to the dissolution of the LDH material in acidic medium. Therefore pH 6 can

be considered as the optimum pH value for the removal of RBV-5r from aqueous solutions.[1,56] Figure 2.14 shows the effect of the initial dye concentration on the removal efficiency of RBV-5r. According to the results, the percentage removal decreased with an increase in initial dye concentration. This may be due to the limited availability of the vacant active sites at higher dye concentration.[1,13] Higher adsorption capacity of the material was observed with increasing temperature, suggesting that the dye removal is an endothermic process. This could be due to the higher diffusion of dye molecules at higher temperatures. The results reveal that with higher kinetic energy, dye molecules were able to overcome the energy barrier restricting the bonding between dye molecules and the sorbent. Further increase in temperature did not show a significant effect on the adsorption process.[2,24]

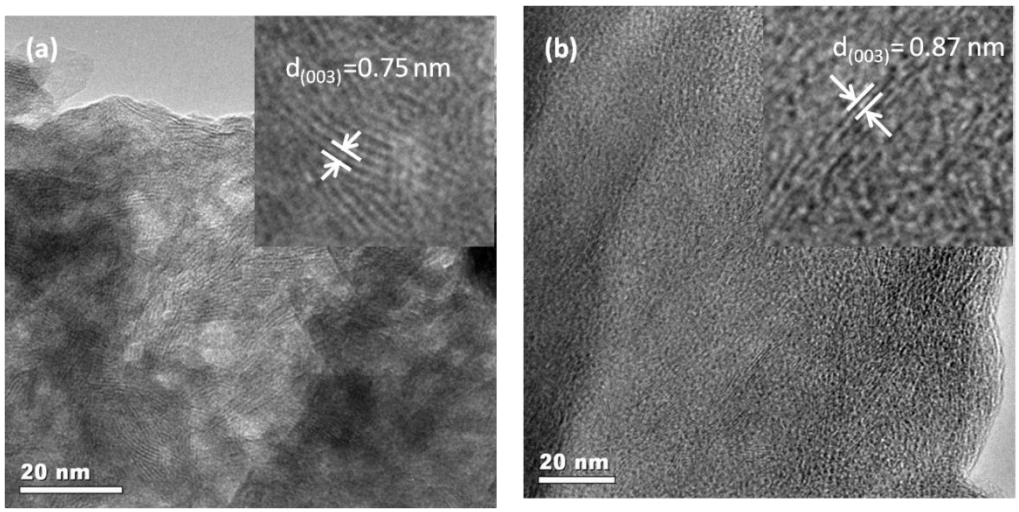

Figure 2.17. The d-spacing values of the NiAl-C250$_{SC}$ (a) before and (b) after RBV-5r intercalation.

The mechanism of the dye removal and the orientation of the dye molecule in between the layered structure were confirmed by the XRD data, FTIR analyses and MD simulation studies of LDH before and after the dye adsorption. According to the XRD patterns, the d-spacing values of the NiAl-$C250_{SC}$ before and after the adsorption of the dye were 7.48 Å and 8.71 Å, respectively. The net increase in the basal spacing from 7.48 Å to 8.71 Å strongly agrees with the intercalation of the organic dye molecule. As seen from TEM images in Figure 2.17, the d-spacing values of the NiAl-$C250_{SC}$ before and after the intercalation were 0.75 nm and 0.87 nm, respectively. The net increase in the basal spacing further confirms the intercalation of dye molecules into LDH material.

The results obtained from XRD and TEM were confirmed by FTIR spectroscopy data for the uptake of RBV-5r dye by Ni-Al LDH material calcined at 250˚C. After the dye intercalation, the material showed peaks at 1150 and 1050 cm^{-1} which correspond to the S=O stretching vibrations of SO_3^{2-} from the organic dye molecule and this resembles the intercalation of the RBV-5r molecule in the brucite-like sheets. Further evidence for the replacement of the interlayer NO_3^- anions by the dye molecule can be obtained by studying the absorption peak around 1386 cm^{-1}. Interlayer NO_3^- anions give a strong absorption peak around 1386 cm^{-1} due to the bending vibration of N-O. The ion-exchange between NO_3^- and SO_3^{2-} in the dye molecule was verified by the decrease in the intensity of the NO_3^- peak after the intercalation.[1,4,57]

Table 2.2. Comparison between experimental results and MD simulations

System	Basal d spacing (Å) - Experimental	Basal d spacing (Å) – MD simulations
NiAl-C250$_{SC}$	7.48	7.59
NiAl-C250$_{SC}$ + DYE	8.71	8.75

According to MD simulation data, the calculated d-spacing value d_{003} of the NiAl-C250$_{SC}$ material was 7.59 ($\pm$0.01) Å. The d-spacing value of the NiAl-C250$_{SC}$ material was increased from 7.59 ($\pm$0.01) Å to 8.75 ($\pm$0.02) Å after intercalation with the dye. This confirms the horizontal or the flat orientation of dye molecules in the dye adsorbed NiAl-C250$_{SC}$ material. The d-spacing values obtained from MD simulation studies were in good agreement with the experimental results. Experimental and MD simulation data for the d-spacing values are given in Table 2.2.[47,58,59]

Thermal decomposition of NiAl-LDH$_{sc}$ and the RBV-5r adsorbed NiAl-C250$_{SC}$ were studied up to 900˚C under dynamic nitrogen atmospheres. Figure 2.11 shows TGA analysis profiles for the sonochemically synthesized NiAl LDH (NiAl-LDH $_{SC}$) and the RBV-5r adsorbed NiAl-C250$_{SC}$. First weight loss for both the samples was observed in the temperature range lower than 200˚C which is due to the removal of physically absorbed and interlayer water molecules. NiAl-LDH$_{SC}$ and RBV-5r adsorbed NiAl-C250$_{SC}$ represent mass losses of 5% and 8.91% respectively.[1,57] The second weight loss for NiAl-LDH$_{SC}$ in the temperature

ranges between 150 and 350˚C could be attributed to the removal of water molecules from condensation of hydroxyl groups from brucite layers and NO_2 from the interlayer anions (9.63% loss mass). The second sharp weight loss of RBV-5r adsorbed NiAl-$C250_{SC}$ is about 35.89% which is a significantly high number compared to the material without the dye. This is due to the combined effect of dehydroxylation of the LDH matrix and the thermal decomposition of the intercalated anionic dye.

2.5. Conclusion

In summary, we have synthesized NiAl-LDH using ultrasound radiation and employed the resulting material successfully in adsorptive removal of RBV-5r from aqueous solutions. The effects of calcination temperature, initial dye concentration, contact time, solution temperature and the pH on the adsorption capacity of RBV-5r onto the NiAl-LDH material were studied. NiAl-LDH calcined at 250˚C gave the best dye removal efficiency (100 % removal in 6 min) with an adsorption capacity of 150 mg/g at pH=6. The intercalation of the dye molecule in the layered structure was observed by using XRD and FTIR and further clarified using MD simulation data of the material before and after the dye adsorption. Good agreement was found between the experimental and calculated d-spacing values confirming the horizontal orientation of the dye molecule in the interlayer gallery of the host structure. These data revealed that the removal of the reactive dye was mainly governed by ion-exchange between the dye and nitrate ions and coulombic attraction between the dye molecule and LDH surface. This can be

considered as a very reliable process among all the other dye removal techniques due to its simplicity, ease of operation, economic feasibility, high efficiency, and recyclability. Moreover, it removes the complete dye molecule from aqueous effluents unlike other methods, which destroy only the dye chromophore leaving the harmful residues. Therefore, calcined NiAl-LDH could be used as an excellent adsorbent for the removal of RBV-5r from aqueous solutions.

References

(1) Hameed, B. H.; Ahmad, A. A.; Aziz, N. Isotherms, Kinetics and Thermodynamics of Acid Dye Adsorption on Activated Palm Ash. *Chem. Eng. J.* **2007***, 133*, 195-203.

(2) Singh, V.; Sharma, A. K.; Sanghi, R. Poly(acrylamide) Functionalized Chitosan: An Efficient Adsorbent for Azo Dyes from Aqueous Solutions. *J. Hazard. Mater.* **2009***, 166*, 327-335.

(3) Gupta, V.K.; Suhas. Application of Low-cost Adsorbents for Dye Removal-A review. *J. Environ. Manage.* **2009,** *90,* 2313–2342.

(4) J Zhi, Y.; Li, Y.; Zhang, Q.; Wang, H. ZnO Nanoparticles Immobilized on Flaky Layered Double Hydroxides as Photocatalysts with Enhanced Adsorptivity for Removal of Acid Red G. *Langmuir* **2010**, *26,* 15546–15553.

(5) Tan, I. A. W.; Hameed, B. H.; Ahmad, A. L. Equilibrium and Kinetic Studies on Basic Dye Adsorption by Oil Palm Fibre Activated Carbon. *Chem. Eng. J.* **2007***, 127*, 111-119.

(6) Dizge, N.; Aydiner, C.; Demirbas, E.; Kobya, M.; Kara, S. Adsorption of Reactive Dyes from Aqueous Solutions by Fly Ash: Kinetic and Equilibrium Studies. *J. Hazard. Mater.* **2008***, 150*, 737-746.

(7) Kornaros, M.; Lyberatos, G. Biological Treatment of Wastewaters from a Dye Manufacturing Company using a Trickling Filter. *J. Hazard. Mater.* **2006***, 136*, 95-102.

(8) Lee, J.; Choi, S.; Thiruvenkatachari, R.; Shim, W.; Moon, H. Submerged Microfiltration Membrane Coupled with Alum Coagulation/powdered Activated Carbon Adsorption for Complete Decolorization of Reactive Dyes. *Water Res.* **2006***, 40*, 435-444.

(9) Dutta, K.; Mukhopadhyay, S.; Bhattacharjee, S.; Chaudhuri, B. Chemical Oxidation of Methylene Blue using a Fenton-like Reaction. *J. Hazard. Mater.* **2001***, 84*, 57-71.

(10) Forgacs, E.; Cserháti, T.; Oros, G. Removal of Synthetic Dyes from Wastewaters: a Review. *Environ. Int.* **2004***, 30*, 953-971.

(11) Selcuk, H. Decolorization and Detoxification of Textile Wastewater by Ozonation and Coagulation Processes. *Dyes Pigments* **2005***, 64*, 217-222.

(12) Buonomenna, M. G.; Gordano, A.; Golemme, G.; Drioli, E. Preparation, Characterization and Use of PEEKWC Nanofiltration Membranes for Removal of Azur B Dye from Aqueous Media. *React. Funct. Polym.* **2009***, 69*, 259-263.

(13) Han, R.; Zhang, J.; Han, P.; Wang, Y.; Zhao, Z.; Tang, M. Study of Equilibrium, Kinetic and Thermodynamic Parameters about Methylene Blue Adsorption onto Natural Zeolite. *Chem. Eng. J.* **2009***, 145*, 496-504.

(14) Liu, C.; Wu, J.; Chiu, H.; Suen, S.; Chu, K. H. Removal of Anionic Reactive Dyes from Water using Anion Exchange Membranes as Adsorbers. *Water Res.* **2007***, 41*, 1491-1500.

(15) Muruganandham, M.; Swaminathan, M. TiO2–UV Photocatalytic Oxidation of Reactive Yellow 14: Effect of Operational Parameters. *J. Hazard. Mater.* **2006***, 135*, 78-86.

(16) Arami, M.; Limaee, N. Y.; Mahmoodi, N. M.; Tabrizi, N. S. Equilibrium and Kinetics Studies for the Adsorption of Direct and Acid Dyes from Aqueous Solution by Soy Meal Hull. *J. Hazard. Mater.* **2006***, 135*, 171-179.

(17) Ghosh, D.; Bhattacharyya, K. G. Adsorption of Methylene Blue on Kaolinite. *Appl. Clay. Sci.* **2002***, 20*, 295-300.

(18) Pengthamkeerati, P.; Satapanajaru, T.; Singchan, O. Sorption of Reactive Dye from Aqueous Solution on Biomass Fly Ash. *J. Hazard. Mater.* **2008***, 153*, 1149-1156.

(19) Pendleton, P.; Wu, S. H. Kinetics of Dodecanoic Acid Adsorption from Caustic Solution by Activated Carbon. *J. Colloid Interface Sci.* **2003***, 266*, 245-250.

(20) Bi, B.; Xu, L.; Xu, B.; Liu, X. Heteropoly Blue-intercalated Layered Double Hydroxides for Cationic Dye Removal from Aqueous Media. *Appl. Clay. Sci.* **2011***, 54*, 242-247.

(21) Faki, A.; Turan, M.; Ozdemir, O.; Turan, A.Z. Analysis of Fixed - Bed Column Adsorption of Reactive Yellow 176 onto Surfactant-Modified Zeolite. *Ind. Eng. Chem. Res.* **2008**, *47,* 6999–7004.

(22) Ai, L.; Jiang, J.; Zhang, R. Uniform Polyaniline Microspheres: A Novel Adsorbent for Dye Removal from Aqueous Solution. *Synth. Met.* **2010***, 160*, 762-767.

(23) Ai, L.; Zhou, Y.; Jiang, J. Removal of Methylene Blue from Aqueous Solution by Montmorillonite/$CoFe_2O_4$ Composite with Magnetic Separation Performance. *Desalination* **2011***, 266*, 72-77.

(24) Ai, L.; Zhang, C.; Meng, L. Adsorption of Methyl Orange from Aqueous Solution on Hydrothermal Synthesized Mg_Al Layered Double Hydroxide. *J. Chem. Eng. Data* **2011**, *56*, 4217–4225.

(25) Cho, S.; Jung, S.; Jeong, S.; Bang, J.; Park, J.; Park, Y.; Kim, S. Strategy for Synthesizing Quantum Dot-Layered Double Hydroxide Nanocomposites and Their Enhanced Photoluminescence and Photostability. *Langmuir* **2013**, *29,* 441–447.

(26) Lei, X.; Jin, M.; Gareth, R. Layered Double Hydroxides in the Remediation and Prevention of Water Pollution. Energy and Environment Focus 2014, *3*, 4-22.

(27) Bontchev, R.P.; Liu, S.; Krumhansl, J.L.; Voigt, J.; Nenoff , T.M. Synthesis, Characterization, and Ion Exchange Properties of Hydrotalcite $Mg_6Al_2(OH)_{16}(A)_x(A')_{2-x}\cdot 4H_2O$ (A, A' = Cl^-, Br^-, I^-, and NO_3^-, $2 \geq x \geq 0$) Derivatives. *Chem. Mater.* **2003**, *15,* 3669–3675.

(28) Vaccari, A. Preparation and Catalytic Properties of Cationic and Anionic Clays. *Catal. Today* **1998***, 41*, 53-71.

(29) Kim, T.W.; Sahimi, M.; Tsotsis, T.T. The Preparation and Characterization of Hydrotalcite Thin Films. *Ind. Eng. Chem. Res.* **2009**, *48,* 5794–5801.

(30) Brito, A.; Borges, M.E.; Garı´n, M.; Herna´ndez, A. Biodiesel Production from Waste Oil Using Mg-Al Layered Double Hydroxide Catalysts. *Energy Fuels* **2009**, *23*, 2952–2958.

(31) Panda, H.S.; Srivastava, R.; Bahadur, D. In-Vitro Release Kinetics and Stability of Anticardiovascular Drugs-Intercalated Layered Double Hydroxide Nanohybrids. *J. Phys. Chem. B* **2009**, *113,* 15090-15100.

(32) Poznyak, S. K.; Tedim, J.; Rodrigues, L. M.; Salak, A. N.; Zheludkevich, M. L.; Dick, L. F. P.; Ferreira, M. G. S. Novel Inorganic Host Layered Double

Hydroxides Intercalated with Guest Organic Inhibitors for Anticorrosion Applications. *ACS Appl. Mater. Interfaces* **2009**, *1,* 2353–2362.

(33) Li, M.; Ni, F.; Wang, Y.; Xu, S.; Zhang, D.; Wang, L. LDH Modified Electrode for Sensitive and Facile Determination of Iodate. *Appl. Clay. Sci.* **2009***, 46*, 396-400.

(34) Ma, R.; Liang, J.; Liu, X.; Sasaki, T. J. General Insights into Structural Evolution of Layered Double Hydroxide: Underlying Aspects in Topochemical Transformation from Brucite to Layered Double Hydroxide. *J. Am. Chem. Soc.* **2012**, *134,* 19915-19921.

(35) Wang, C.J.; Wu, Y.A.; Jacobs, R.M.J.; Warner, J.H.; Williams, G.R.; O'Hare, D. Reverse Micelle Synthesis of Co-Al LDHs: Control of Particle Size and Magnetic Properties. *Chem. Mater.* **2011**, *23,* 171–180.

(36) Zhao, M.; Zhang, Q.; Huang, J.; Wei, F. Hierarchical Nanocomposites Derived from Nanocarbons and Layered Double Hydroxides - Properties, Synthesis, and Applications. *Adv. Funct.Mater.* **2012***, 22*, 675-694.

(37) Lopez, T.; Bosch, P.; Ramos, E.; Gomez, R.; Novaro, O.; Acosta, D.; Figueras, F. Synthesis and Characterization of Sol−Gel Hydrotalcites Structure and Texture. *Langmuir* **1996**, *12*, 189–192.

(38) Oh, J.; Hwang, S.; Choy, J. The Effect of Synthetic Conditions on Tailoring the Size of Hydrotalcite Particles. *Solid State Ionics* **2002***, 151*, 285-291.

(39) Morel-Desrosiers, N.; Pisson, J.; Israeli, Y.; Taviot-Gueho, C.; Besse, J.; Morel, J. Intercalation of Dicarboxylate Anions into a Zn-Al-Cl Layered Double Hydroxide: Microcalorimetric Determination of the Enthalpies of Anion Exchange. *J. Mater. Chem.* **2003**, 2582- 2585.

(40) Erickson, K. L.; Bostrom, T. E.; Frost, R. L. A Study of Structural Memory Effects in Synthetic Hydrotalcites using Environmental SEM. *Mater. Let.* **2005***, 59*, 226-229.

(41) Ogawa, M.; Asai, S. Hydrothermal Synthesis of Layered Double Hydroxide Deoxycholate Intercalation Compounds. *Chem. Mater.* **2000**, *12*, 3253–3255.

(42) Seida, Y.; Nakano, Y.; Nakamura, Y. Crystallization of Layered Double Hydroxides by Ultrasound and the Effect of Crystal Quality on their Surface Properties. *Clay Clay Miner.* **2002***, 50*, 525-532.

(43) Bang, J. H.; Suslick, K. S. Applications of Ultrasound to the Synthesis of Nanostructured Materials. *Adv. Mater.* **2010***, 22*, 1039-1059.

(44) Cabanas-Polo, S.; Suslick, K. S.; Sanchez-Herencia, A. J. Effect of Reaction Conditions on Size and Morphology of Ultrasonically Prepared $Ni(OH)_2$ Powders. *Ultrason. Sonochem.* **2011***, 18*, 901-906.

(45) Dharmarathna, S.; King'ondu, C.K.; Pedrick, W.; Pahalagedara, L.; Suib, S.L. Direct Sonochemical Synthesis of Manganese Octahedral Molecular Sieve (OMS-2) Nanomaterials Using Cosolvent Systems, Their Characterization, and Catalytic Applications. *Chem. Mater.* **2012**, *24*, 705–712.

(46) Zhang, J.; Du, J.; Han, B.; Liu, Z.; Jiang, T.; Zhang, Z. Sonochemical Formation of Single-Crystalline Gold Nanobelts. *Angew. Chem. Int. Edit.* **2006***, 45*, 1116-1119.

(47) Aguiar, J.E.; Bezerra, B.T.C.; Braga, B.M.; Lima, P.D.S.; Nogueira, R.E.; Lucena, S.M.P.; da Silva Jr. I.J. Adsorption of Anionic and Cationic Dyes from Aqueous Solution on Non-Calcined Mg-Al Layered Double Hydroxide: Experimental and Theoretical Study. *Separ. Sci. and Technol.* **2013**, *48,* 2307-2316.

(48) Smith, W.; Forester, T.; Todorov, I.; Cheshire, U., The DL POLY Classic user manual. *STFC, STFC Daresbury Laboratory, Daresbury, Warrington, Cheshire, WA4 4AD, United Kingdom,* **2010**.

(49) Cygan, R. T.; Liang, J.-J.; Kalinichev, A. G., Molecular Models of Hydroxide, Oxyhydroxide, and Clay Phases and the Development of a General Force Field. *J. Phys. Chem. B* **2004**, *108*, 1255-1266.

(50) Jorgensen, W. L.; Maxwell, D. S.; Tirado-Rives, J., Development and Testing of the OPLS All-Atom Force Field on Conformational Energetics and Properties of Organic Liquids. *J. Am. Chem. Soc.* **1996**, *118*, 11225-11236.

(51) Bayly, C. I.; Cieplak, P.; Cornell, W.; Kollman, P. A., A Well-behaved Electrostatic Potential Based Method using Charge Restraints for Deriving Atomic Charges: The RESP Model. *J. Phys.Chem.* **1993**, *97*, 10269-10280.

(52) Pahalagedara, L.; Sharma, H.; Kuo, C-H.; Dharmarathna, D.; Joshi, A.; Suib, S.L.; Mhadeshwar, A.B., Structure and Oxidation Activity Correlations for Carbon Blacks and Diesel Soot. *Energy Fuels* **2012**, 26, 6757–6764.

(53) Vieira, A.C.; Moreira, R.L.; Dias, A. Raman Scattering and Fourier Transform Infrared Spectroscopy of $Me_6Al_2(OH)_{16}C_{l2}\cdot 4H_2O$ (Me=Mg, Ni, Zn, Co, and Mn) and $Ca_2Al(OH)_6Cl\cdot 2H_2O$ Hydrotalcites. *J. Phys. Chem. C* **2009**, *113,* 13358–13368.

(54) Mdleleni, M.M.; Hyeon, T.; Suslick, K.S. Sonochemical Synthesis of Nanostructured Molybdenum Sulfide. *J. Am. Chem. Soc.* **1998**, *120*, 6189-6190.

(55) Xu, H.; Zeiger, B. W.; Suslick, K. S. Sonochemical Synthesis of Nanomaterials. *Chem. Soc. Rev.* **2013**, *42*, 2555-2567.

(56) Zhao, Q.; Chang, Z.; Lei, X.; Sun, X. Adsorption Behavior of Thiophene from Aqueous Solution on Carbonate- and Dodecylsulfate-Intercalated ZnAl Layered Double Hydroxides. *Ind. Eng. Chem. Res.* **2011**, *50*, 10253–10258.

(57) Saiah, F. B. D.; Su, B.; Bettahar, N. Nickel–iron Layered Double Hydroxide (LDH): Textural Properties upon Hydrothermal Treatments and Application on Dye Sorption. *J. Hazard. Mater.* **2009***, 165*, 206-217.

(58) Wang, J.; Kalinichev, A.G.; Kirkpatrick, R.J.; Hou, X. Molecular Modeling of the Structure and Energetics of Hydrotalcite Hydration. *Chem. Mater.* **2001**, *13*, 145–150.

(59) Zhang, P.; Qian, G.; Shi, H.; Ruan, X.; Yang, J.; Frost, R. L. Mechanism of Interaction of Hydrocalumites (Ca/Al-LDH) with Methyl Orange and Acidic Scarlet GR. *J. Colloid Interface Sci.* **2012***, 365*, 110-116.

CHAPTER III. COPPER ALUMINUM MIXED OXIDE (CUAL MO) CATALYST: A GREEN APPROACH FOR THE ONE-POT SYNTHESIS OF IMINES UNDER SOLVENT-FREE CONDITIONS

3.1. Introduction

The search for new environmentally benign reagents and catalysts with high efficiency and minimum waste production has become one of the most important goals in Chemistry. In this sense one-pot, tandem, or cascade reactions involving multiple catalytic transformations reduces the number of synthetic steps by leading sequential catalytic processes into one-synthetic operation with minimum workup, or change in conditions.[1] These processes have become an important area of research since they improve atom economy and decrease energy consumption and raw materials consumption by avoiding intermediate separation and purification steps.[2] Catalysis of two or more mechanically distinct processes by a single catalyst is known as auto tandem catalysis. Searching for such direct synthetic pathways are key for green and sustainable chemistry as they avoid side product formation, loss of starting material, separation and purification of intermediates therefore producing an economical as well as environmental benefits.[3,4]

Synthesis of imines is a very important reaction in chemistry as well as in biology as they are crucial intermediates in the synthesis of biologically active nitrogen compounds, nitrogen heterocycles, fine chemicals, and

pharmaceuticals.[5,6] In general, imines are synthesized by the condensation of primary amines with carbonyl compounds. However, several other synthetic strategies have been developed such as dimerization of primary amines under oxidative conditions, transition metal-promoted hydrogen transfer from secondary amines, oxidation of secondary amines, and the direct reaction of nitro arenes and primary alcohols in the presence of hetero bimetallic catalysts.[7,8,9]

The synthesis of imines through the cross-coupling between amines and alcohols is a very useful and appropriate preparation method due to their wide substrate scope. In this method, aldehydes and ketones are obtained from alcohols by stoichiometric oxidation. Compared to carbonyl compounds, alcohols are less toxic, readily available, more stable, inexpensive, and easier to handle and produce only hydrogen or water as a byproduct.[10] Therefore it can be considered as an environmentally attractive method for the synthesis of imines. Several catalytic systems have been reported for this reaction sequence based on precious metals such as platinum, iridium, palladium under homogeneous conditions[11,12,13] or other systems like graphene oxide[14] and copper.[15] But the pricing, limited availability, toxicities and non-recoverable nature have forbidden their large-scale usage.[5,16,17] Therefore it is highly desirable to develop mild, efficient, more environmentally and economically friendly alternatives for the synthesis of imines.[18,19] Furthermore, these processes require dehydrating agents, additional bases, activated aldehydes, prolonged reaction time, high temperatures and stoichiometric oxidants.[20] However, the use of oxidants such as chromate, permanganate or 2-iodoxybenzoic acid[21] has several drawbacks,

which are the difficulty in product separation and the formation of undesirable toxic waste products.

In the present study, we report the tandem synthesis of imines directly from alcohols and amines under mild conditions using an inexpensive CuAl mixed oxide (MO) catalyst and air as an oxidant. CuAl MO acts as a bifunctional catalyst in the process to oxidize the alcohol to the corresponding carbonyl compound and then acts as a Lewis acid to form the imine. Here, a urea hydrolysis method was used to synthesize the CuAl mixed hydroxide material in the presence of activated carbon which subsequently helps to tune the surface properties of the resultant metal oxide. The catalytic process is done under solvent free conditions and it does not form any harmful byproducts. In this reaction, air is used as the oxidant which is considered as the most economical and green oxidant among different oxidizing agents. Furthermore, this process does not require any base additives, dehydrating agents or any special apparatus.

3.2. Experimental Section

3.2.1 Synthesis of activated carbon/mixed hydroxide composites and corresponding metal oxide catalysts

Activated carbon/CuAl mixed hydroxide composite (Cu/Al molar ratio = 3) was synthesized through a urea hydrolysis process in the presence of activated

carbon. Synthesis was done by adding 1.5 × 10^{-3} mol of $Cu(NO_3)_2 \cdot 6H_2O$, 0.5× 10^{-3} mol of $Al(NO_3)_3 \cdot 9H_2O$, 4.0× 10^{-3} mol of urea and a known amount of activated carbon into 60 mL deionized water under vigorous stirring at room temperature. The mixture was refluxed 100°C for 15 h, then filtered and washed with deionized water several times. The resultant dark green colored solid was then dried under vacuum at 60°C for 12 h and calcined at 500°C for 3 h in air in order to remove activated carbon. The entire procedure was repeated, changing the amount of activated carbon (5%, 10% and 20%-% w/w) added while keeping other reaction conditions constant, to obtain a series of activated carbon/ mixed hydroxide composites. Controlled experiments were also carried out by repeating the whole process in the absence of activated carbon. The obtained calcined materials were denoted as CuAl $MO_{x\%C}$ (x = 0, 5, 10, 20) where x stands for the activated carbon amount.

3.2.2. Catalyst characterization

3.2.2.1. X-Ray Powder Diffraction Studies

Powder X-ray diffraction (XRD) analyses were performed on a Rigaku Ultima IV diffractometer with Cu Kα(λ = 0.15406 nm) radiation with a beam voltage of 40 kV and a beam current of 44 mA. Continuous scans were taken in a 2θ range of 5-60° with a scanning rate of 2.0 °/min, and the phases were identified using the International Center for Diffraction Data (ICDD) database.

3.2.2.2. Scanning Electron Microscopy and Energy Dispersive X-ray Spectroscopy

Surface morphologies of the synthesized materials were studied using field emission scanning electron microscopy (FE-SEM) on a Zeiss DSM 982 Gemini instrument with a Schottky emitter at an accelerating voltage of 2.0 kV with a beam current of 1.0 mA. The samples were ultrasonically suspended in absolute ethanol and dispersed on Au-coated silicon chips and then dried overnight under vacuum. The EDX analysis was done using an Oxford X-max80 EDX analyzer operating at an electron accelerating voltage of 10 kV.

3.2.2.3. Transmission Electron Microscopy

Transmission electron microscopy (TEM) was used to examine the surface morphologies and the crystalline structures of the materials using a JEOL 2010 instrument with an accelerating voltage of 200 kV. The samples were prepared by dispersing the material in ethanol. Then a drop of the dispersion was placed on a carbon coated copper grid and allowed to dry before analysis.

3.2.2.4. Fourier Transformation infra Red (FT-IR) Spectroscopy

Fourier transform infrared (FTIR) spectroscopy experiments were performed using a Thermo-Scientific Nicolet FT-IR Model 8700 (in the range 4000-400 cm^{-1}) equipped with a DTGS detector and a KBr beam splitter. Spectra were collected with a resolution of 4 cm^{-1} using 250 scans. Pyridine adsorption studies were performed with 13mm diameter self-supporting pellets. The pellets were cleaned in a tubular furnace at 250˚C for 2 h under dry air flow. A 1 M pyridine solution in methanol was dropped on pellets, and physisorbed pyridine was removed in a tubular furnace running at 200˚C for 90 min under dry air flow and FTIR spectra of the pellets were collected.[22]

3.2.2.5. N_2 Sorption Studies

The nitrogen sorption experiments were performed using Quantachrome Autosorb iQ_2 instrument instrument using N_2 gas as the adsorbate at 77 K by a multipoint method. The Brunauer- Emmett-Teller (BET) method was used to determine the specific surface area and the Barrett-Joyner-Halenda (BJH) desorption method was used to calculate the pore size distribution and pore volume. Prior to the analysis, all the samples were degassed at 150˚C for 12 h in order to remove any adsorbed species.

3.2.2.6. Thermogravimetric mass spectrometry

Thermogravimetric mass spectrometry (TG-MS) was studied using a Netzsch Libra TG209 F1 thermogravimetric analyzer coupled to a Netzsch Aëolos QMS 403C quadrupole mass spectrometer. Approximately 15 mg of sample was loaded into an alumina crucible. Argon was flowed through the sample chamber at 50 SCCM while the temperature was ramped from room temperature to 1000˚C at a rate of 20˚C/min.

3.2.3. Catalytic activity: One-Pot coupling of 4-Chlorobenzyl alcohol and Benzylamine

For catalytic studies, One-Pot coupling of 4-Chlorobenzyl alcohol and Benzylamine was carried out in a batch reactor. 4-Chlorobenzyl alcohol and Benzylamine were purchased from Sigma-Aldrich and used without further purification. A mixture of 1 mmol of 4-Chlorobenzyl alcohol, 1.2 mmol of Benzylamine, and 50 mg of catalyst were stirred under solvent free conditions and the reaction was conducted at 110˚C for 12 h in an oil bath under air atmosphere.

The spent catalyst was recovered by centrifuging the reaction mixture, washing with ethanol and drying in an oven at 120˚C for 12 h. The gas chromatography-mass spectroscopy (GC-MS) method was used for the quantitative analysis and identification of the reaction product. Analyses were performed using a HP 5971 mass selective detector coupled to a HP 5890 Series II gas chromatograph equipped with a thermal conductivity detector (TCD)

through an HP-1 (nonpolar cross-linked methyl siloxane) column with dimensions of 12.5 m × 0.2 mm ×0.33 μm.

3.3. Results

3.3.1. Structural characterization of activated carbon/mixed hydroxide composites and corresponding metal oxides

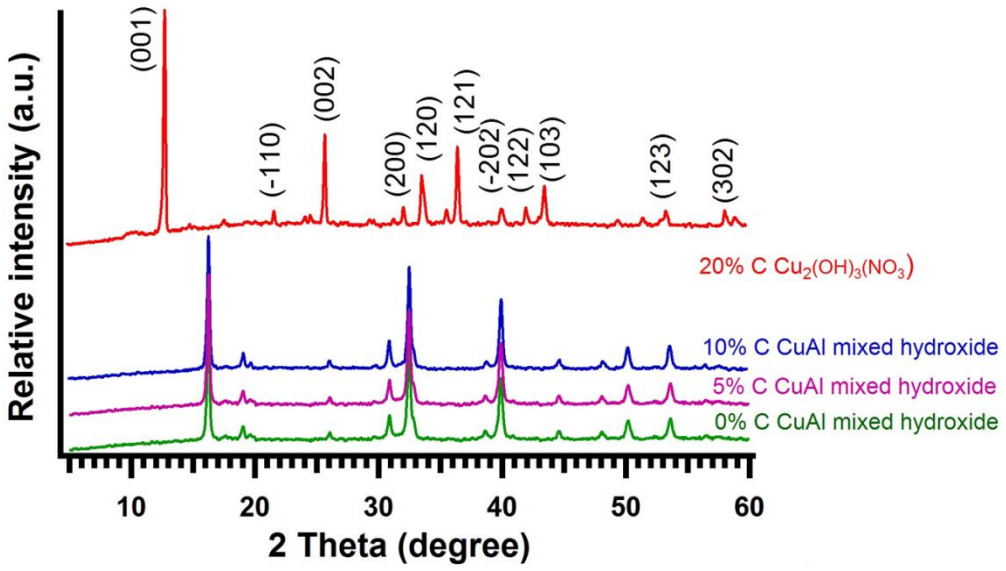

Figure 3.1. X-ray diffraction patterns of CuAl mixed hydroxide materials synthesized with different amounts of activated carbon

XRD patterns of as synthesized CuAl-$C_{x\%}$ mixed hydroxide materials are displayed in Figure 3.1. Samples synthesized with 0%, 5% and 10% activated carbon showed a CuAl mixed hydroxide phase while the XRD pattern of the sample with 20% activated carbon corresponded to copper nitrate hydroxide phase. Above 20%, activated carbon remains as a separate phase in the

reaction mixture, therefore the product obtained was not taken into consideration. When these materials were calcined to remove the template, the hydroxide phase is converted to the oxide phase and XRD peaks could be indexed to the tenorite CuO phase (Figure 3.2).

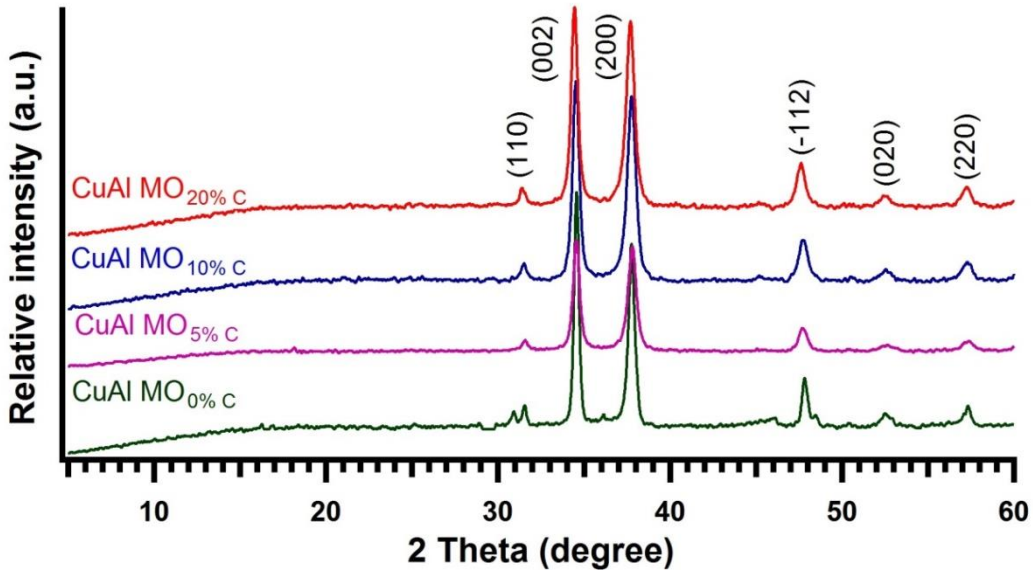

Figure 3.2. X-ray diffraction patterns of CuAl MOs synthesized with different amounts of activated carbon

The average crystallite sizes of calcined samples were calculated according to the Debye -Scherrer equation, $L = 0.89\lambda/\beta(\theta) \cos \theta$ where L is the crystallite size, λ is the wavelength of the radiation used, θ is the Bragg diffraction angle, and β(θ) is the full width at half maximum. Oxide material synthesized without any carbon gave the highest crystallite size which was 27.7 nm. When activated carbon was incorporated to the structure, a huge drop in crystallite size was observed (Table 3.1). 20% sample gave the smallest crystallite size among the series which was 1.1 nm.

Table 3.1. Structural parameters of CuAl MOs

Catalyst	Average crystallite size (nm)	BET SA (m^2/g)	BJH desorption pore volume (cm^3/g)	BJH desorption pore diameter (Å)
CuAl $MO_{0\%C}$	27.7	14	.093	33
CuAl $MO_{5\%C}$	4.1	24	.075	37
CuAl $MO_{10\%C}$	4.4	50	0.22	38
CuAl $MO_{20\%C}$	1.1	161	0.27	40

Porous MOs obtained by calcining the samples at 500˚C were analyzed by N_2 sorption measurements to study their textural properties and pore size distributions. N_2 adsorption/desorption isotherms and BJH pore size distributions of the obtained MOs are presented in (Figures 3.3a and 3.3b). All samples have a Type IV N_2 adsorption isotherm along with a type I hysteresis loop, indicating a regular cylindrical mesoporous structure (Figure 3.3a). CuAl $MO_{20\%C}$ sample gave the highest BET surface area (161 m^2/g), highest pore diameter (40 Å) and the highest pore volume (0.27 cm^3/g) among the compositions tested. Increasing the amount of activated carbon leads to an increase in the surface area and pore volume. Specific surface area values and pore parameters of CuAl MOs are given in Table 3.1. The CuAl $MO_{20\%C}$ sample has a larger N_2 uptake than other samples, which indicates a higher mesopore volume than other MO samples

(Figure 3.3a). All the samples display a late adsorption edge (P/P_0 > 0.8) suggesting an increase in pore size. BJH desorption pore diameters of all the samples lie in the same range and CuAl $MO_{20\%C}$ sample gave a uniform pore size distribution compared to other samples.

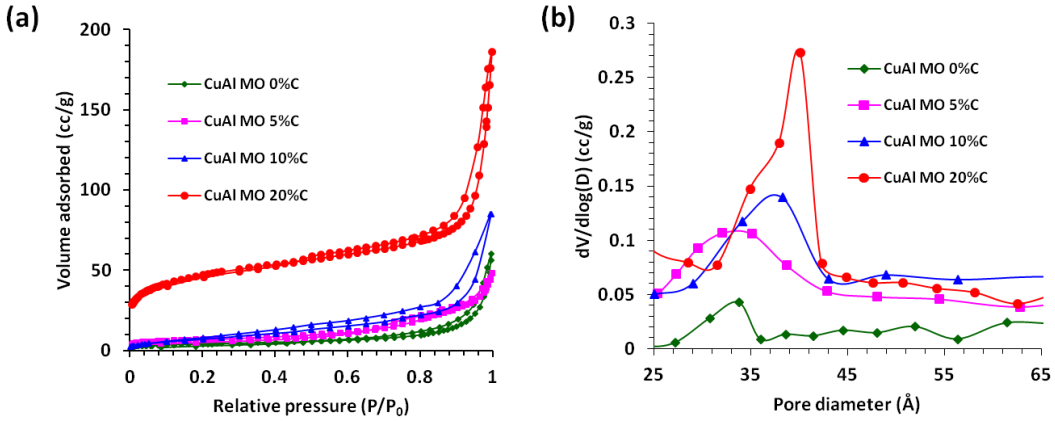

Figure 3.3. (a) N_2 adsorption/desorption isotherms and (b) BJH pore size distribution curves of CuAl MOs synthesized with different amounts of activated carbon

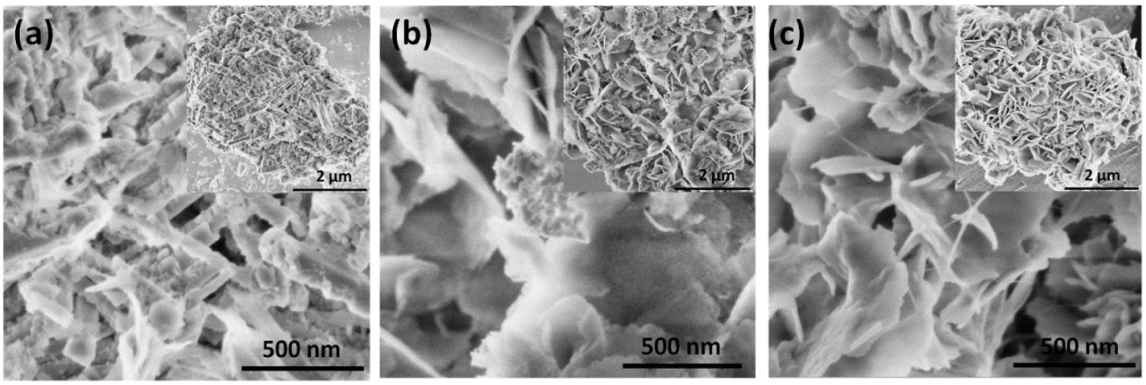

Figure 3.4. FE-SEM images of CuAl mixed hydroxide materials synthesized with (a) 0% activated carbon and (b) 20% activated carbon and (c) CuAl $MO_{20\%C}$ catalyst

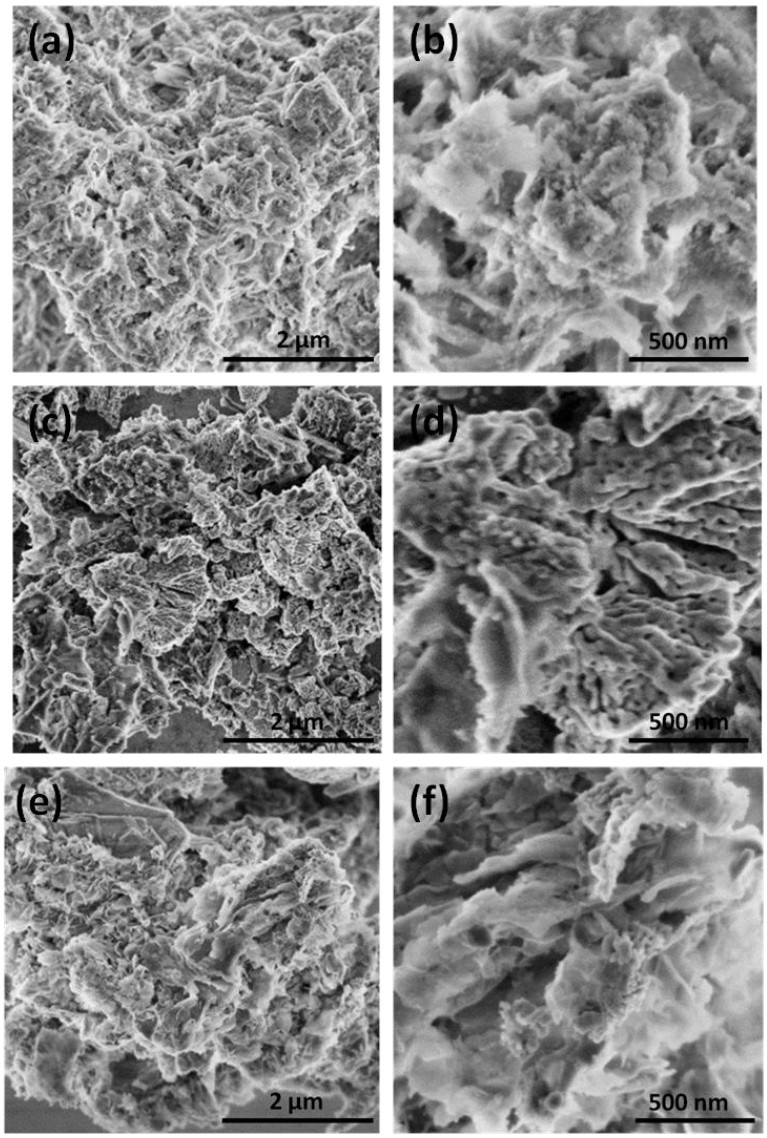

Figure 3.5. FE-SEM images of (a) (b) CuAl $MO_{0\%C}$ (c) (d) CuAl $MO_{5\%C}$ and (e) (f) CuAl $MO_{10\%C}$ catalysts

The surface morphology of mixed hydroxide samples and CuAl MO samples was observed by FE-SEM. As clearly observed in Figure 3.4a, mixed hydroxide material synthesized in the absence of activated carbon template

shows a rough plate like morphology. In contrast, the material prepared with 20% activated carbon, exhibits a nice flower like nanostructure (Figure 3.4b). Upon heat treatment, all the materials are converted to the MO and FE-SEM images of the CuAl MO samples synthesized with different amounts of activated carbon are given in Figure 3.4c and Figure 3.5. When increasing the amount of activated carbon, the surface of the material changes from an irregular shaped plate-like morphology to a nicely arranged flower-like morphology. In all MO samples, Cu and Al are uniformly dispersed and can be detected in all zones measured in a constant composition (Cu 21 %, Al 23 %, O 56 % EDS measures). TEM images of the CuAl $MO_{20\%C}$ catalyst is given in Figure 3.6. According to the TEM image the material is composed of irregular shaped crystalline nanosized particles.

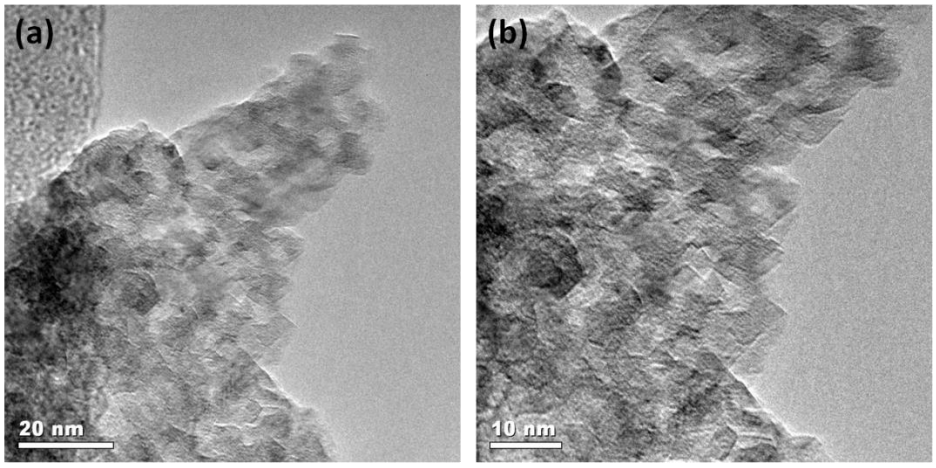

Figure 3.6. TEM images of fresh CuAl $MO_{20\%C}$ catalyst

The FTIR spectra of the as synthesized mixed hydroxide material (20%C) and the CuAl $MO_{20\%C}$ catalyst are given in Figure 3.7. Mixed hydroxide material gives a broad band between 3400 and 3600 cm^{-1} due to the stretching modes of OH groups.[23,24] The presence of NO_3^- in the as-prepared samples is evidenced

by the vibrational bands that occurred from middle to lower wavenumbers, suggesting the presence of mono- or polydentate nitrate ligands (1432, 1376, 1320, 1348, and 802 cm^{-1}).[25] However, after heat treatment (Figure 3.7b), peaks at 3400 - 3600 cm^{-1} and at 802 - 1432 cm^{-1} were decreased significantly. This means that most of the nitrate groups and hydroxyl groups were removed after the heat treatment of the mixed hydroxide phase in air at 500˚C. The bands below 700 cm^{-1} are attributed to the framework vibrations of mixed oxide material.[26,27]

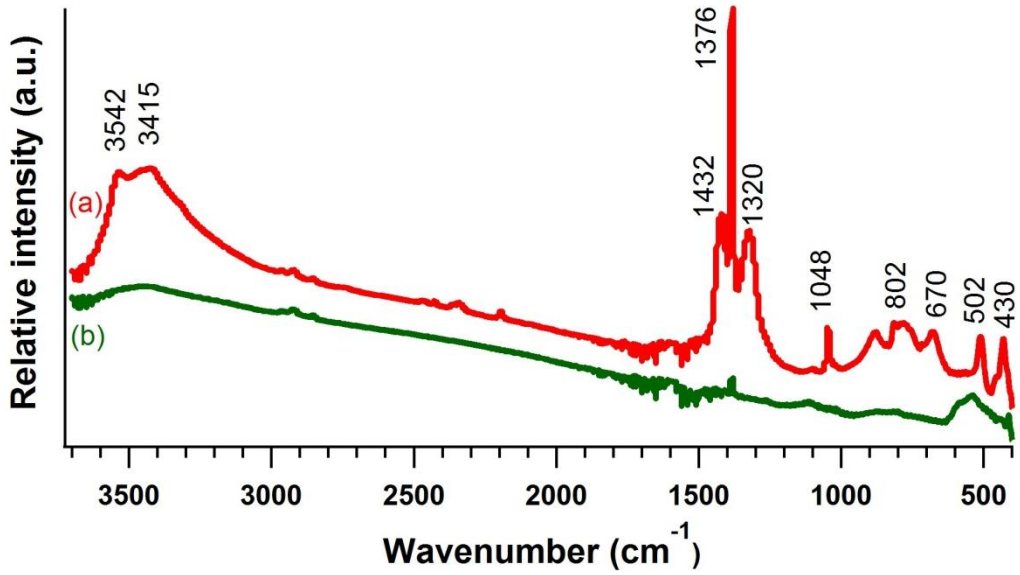

Figure 3.7. FTIR spectra of (a) CuAl mixed hydroxide material synthesized with 20% activated carbon and (b) CuAl $MO_{20\%C}$ catalyst

To rationalize the catalyst effects, the surface acidity was studied by pyridine adsorption experiments as imine formation from carbonyls is generally acid catalyzed. The obtained profiles are presented in Figure 3.8. These profiles represent FTIR spectra of pyridine adsorbed CuAl $MO_{0\%C,}$ CuAl $MO_{5\%C}$ and CuAl

$MO_{20\%C}$ samples in the region between 1400 – 1500 cm^{-1}. The CuAl $MO_{0\%C}$ sample did not show any detectable peaks. However, the other two samples (CuAl $MO_{5\%C}$ and CuAl $MO_{20\%C}$) gave three peaks at around 1450, 1490 and 1538 cm^{-1}. The intensities of the peaks are greatly enhanced when it goes from 5%C sample to 20%C sample (Figure 3.8 b,c). In the figure, pyridine adsorbed on Brønsted acid sites are labelled as B and pyridine adsorbed on Lewis acid sites are labelled as L.

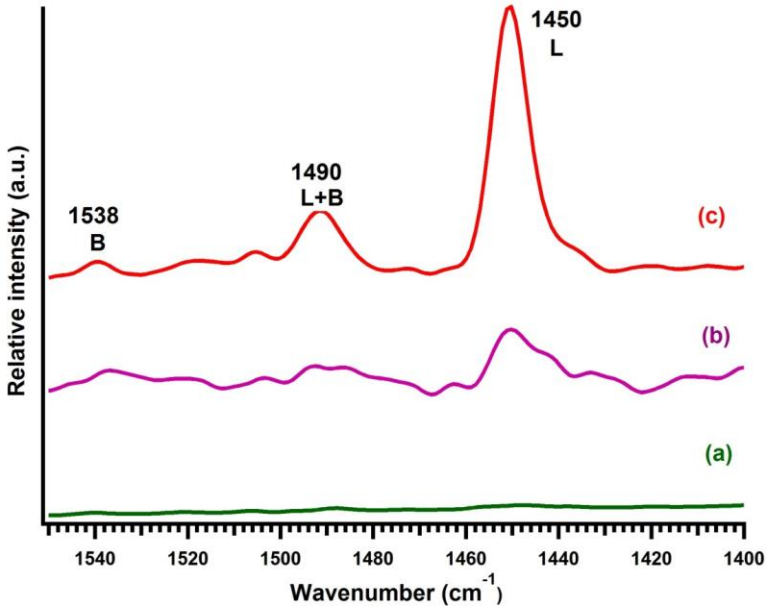

Figure 3.8. The pyridine adsorption IR spectra of (a) CuAl $MO_{0\%C}$ (b) CuAl $MO_{5\%C}$ and (c) CuAl $MO_{20\%C}$ catalysts

The thermogravimetric mass spectrometry (TG-MS) analysis profiles of CuAl $MO_{0\%C,}$ CuAl $MO_{5\%C}$ and CuAl $MO_{20\%C}$ samples are shown in Figure 3.9 . When CuAl $MO_{0\%C}$ material was heated, the TG curve revealed weight losses in four stages. The first weight loss was observed between 100 and 220˚C, second weight loss between 220 and 330˚C and another two weight losses between 350

and 600˚C and beyond 700˚C. Compared to CuAl $MO_{0\%C}$, CuAl $MO_{5\%C}$ and CuAl $MO_{20\%C}$ samples gave only two weight losses between 100 and 220˚C and beyond 700˚C.

In its O_2 evolution profile, CuAl $MO_{0\%C}$ shows three peaks between 220 and 330˚C, 350 and 600˚C and beyond 700˚C. On the other hand, CuAl $MO_{20\%C}$ evolves O_2 from room temperature to 400˚C and beyond 700˚C.

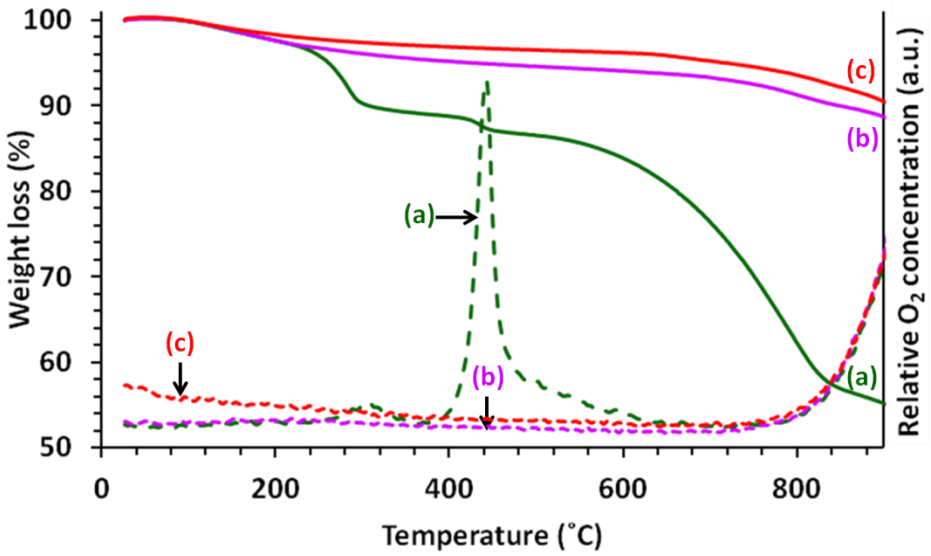

Figure 3.9. TGA (solid line) and O_2 evolution profiles (dash line) of (a) CuAl $MO_{0\%C}$ (b) CuAl $MO_{5\%C}$ and (c) CuAl $MO_{20\%C}$ catalysts

3.3.2. Catalytic activity

The intial imine synthesis was performed using 4-Chlorobenzyl alcohol and benzyl amine at 110 ˚C in the presence of air and the results are given in Table 3.2. All the reactions were carried out with CuAl MO samples under solvent

free conditions. Among the various catalysts tested, CuAl $MO_{20\%C}$ showed the best activity over others. The conversion was 95% in 6 hours, and the imine was the only product giving a100% selectivity. Other catalysts synthesized in the presence of activated carbon similarly gave an impressive conversion. The material synthesized without activated carbon gave a low conversion compared to carbon templated catalysts (Table 3.2, entry 1). Commercial CuO and $CuAl_2O_4$ could only give the imine product with the conversions of 8% and 2%, respectively.

Table 3.2. Synthesis of imines catalyzed by various CuAl MO catalysts

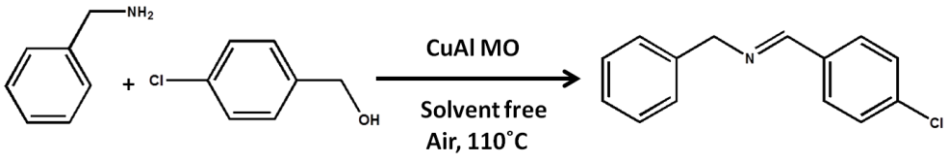

Entry	Catalyst	Conversion (%)	TON [e]	TOF (h^{-1}) [f]
1	CuAl $MO_{0\%C}$	41	8.44	0.70
2	CuAl $MO_{5\%C}$	72	14.82	1.235
3	CuAl $MO_{10\%C}$	78	16.06	1.338
4	CuAl $MO_{20\%C}$	100	20.59	1.716
5	CuAl $MO_{20\%C}$ (6h)	95	19.56	3.26
6	CuAl $MO_{20\%C}$ [a]	32	6.59	0.549
7	CuAl $MO_{20\%C}$ [b]	54	11.12	0.926
8	CuAl $MO_{20\%C}$ [c]	40	8.23	0.685
9	CuAl $MO_{20\%C}$ [d]	15	3.08	0.256
10	No catalyst	Trace	-	-

Reaction conditions: 4-Chlorobenzyl alcohol (1 mmol), benzylamine (1.2 mmol), catalyst (50 mg) 110˚C, 12 h. Conversion and selectivity determined and confirmed by GC-MS. The reaction temperatures were [a]60, [b]80, [c]140˚C respectively. [d] N_2 balloon. [e] Turnover number (TON) = [moles of converted substrate(4-Chlorobenzyl alcohol)] x (moles of catalyst)$^{-1}$. [f]Turnover frequency (TOF) = [moles of converted substrate(4-Chlorobenzyl alcohol)] x [(moles of catalyst) x (reaction time in h)]$^{-1}$

After confirming CuAl $MO_{20\%C}$ as the most effective catalyst, the reaction conditions were further optimized. The reaction was carried out at different temperatures to investigate the effect of temperature on the catalytic performance, and the results are given in Table 3.2 (entries 6-8). The percentage of conversion surged along with increasing reaction temperature from 32% at 60˚C to 95% at 110˚C with 100% selectivity for the imine product. Any further increase in the temperature decreases conversion of the reaction.

In order to confirm the effect of oxidant, which is air in this case, the reaction was performed under inert (N_2) atmosphere in the presence of the catalyst. According to the results, the reaction gave only 15% conversion without air. However, the blank experiment carried out with air in the absence of catalyst showed no conversion (Table 3.2, entry 10).

3.3.3. Reaction scope

Based on these results, the scope and limitations of CuAl $MO_{20\%C}$ catalyzed imine synthesis were explored using various structurally diverse amines and alcohols. First, various amines were tested with 4-Chlorobenzyl alcohol as the coupling partner (Table 3.3). Reaction rate was faster when butyl amine was used as the amine, giving 99% conversion with 100% selectivity in 6h. 4- Chlorobenzylamine, 2, 4-Dichlorobenzylamine and 4-Methoxybenzylamine gave 82%, 74% and 91% conversions under same reaction conditions (entries 2, 3, & 4). When the reaction was carried out with aniline, the conversion was only 64%; however the selectivity for imine was still 100%.

Table 3.3. CuAl $MO_{20\%C}$ catalyzed synthesis of imines from various alcohols and amines.[a]

Entry	Substrate	Product	Conversion	Selectivity
1[b]		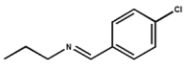	99	100
2[b]	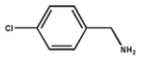	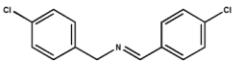	82	100
3[b, d]	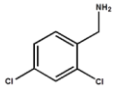	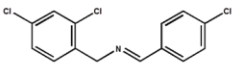	74	85
4[b, d]	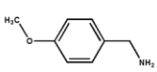	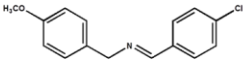	91	81
5[b]		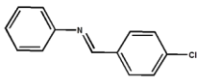	66	100
6[c]	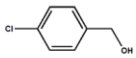	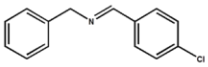	95	100
7[c]	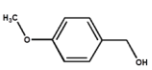	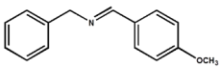	70	100
8[c, d]	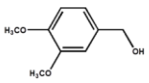	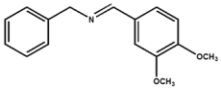	67	84
9[c]		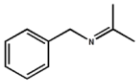	22	100
10[e]	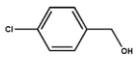	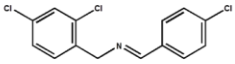	1	100
11[f]	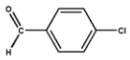	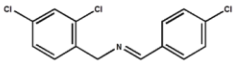	88	100
12[g]	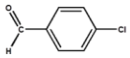	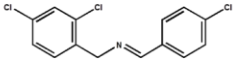	52	100

[a]Reaction conditions: alcohol (1 mmol), amine (1.2 mmol), [catalyst (50 mg) : except entry 10 & 11], 110˚C, 12 h. Conversion and selectivity determined and confirmed by GC-MS. [b] Reaction with 4-Chlorobenzyl alcohol. [c] Reaction with benzylamine. [d]The other product was the corresponding aldehyde of the alcohol. [e, f, g] Reaction with 2,4- Dichlorobenzylamine.

Next, the reactions between benzylamine and different alcohols were tested. 4-chlorobenzyl alcohol with benzylamine (entry 6) gave 95% conversion

and 100% selectivity for imine. 4-methoxy benzylalcohol (entry 7) gave 70% conversion and 100% selectivity for the corresponding imine. In contrast, when 3,4-Dimethoxy benzylalcohol was reacted the conversion was only 67% and selectivity was 84% (entry 8)**.** 2-propanol (entry 9) gave the lowest conversion among the series which was 22% but the selectivity was still 100%. The desired imine was obtained as the major product during the whole course of the reaction. In order to determine the role of the catalyst in the formation of the aldehyde in the first step and formation of imine in the second step, a series of reactions were carried out and the results are given in Table 3.3. When 4-Chlorobenzyl alcohol was reacted with 2,4- Dichlorobenzylamine in the absence of the catalyst, a trace amount of the imine product was observed with a 100% selectivity (entry 10). When the reaction was started with 4-Chlorobenzaldehyde (entry 11, 12), 88% and 52% conversions were observed with and without the catalyst respectively.

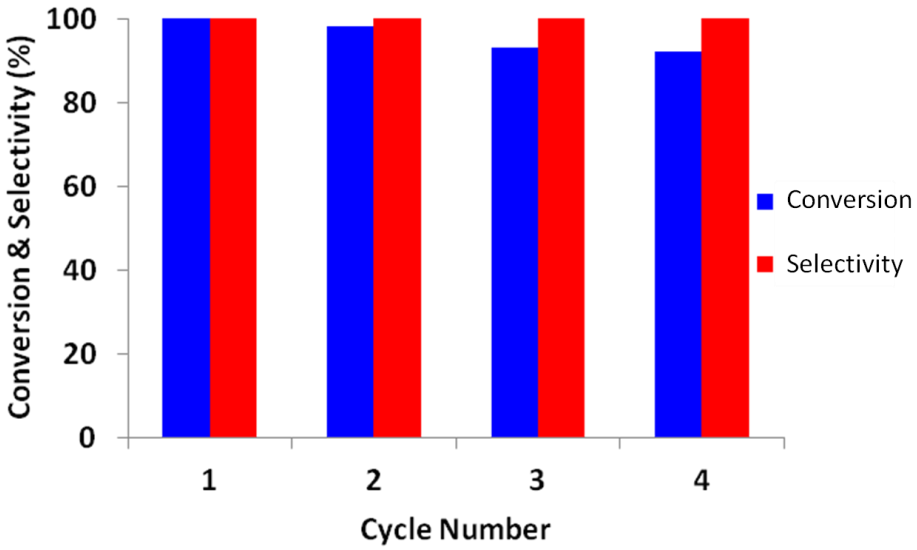

Figure 3.10. Reusability of CuAl $MO_{20\%C}$ catalyst in the imination reaction of 4-Chlorobenzyl alcohol and benzylamine.

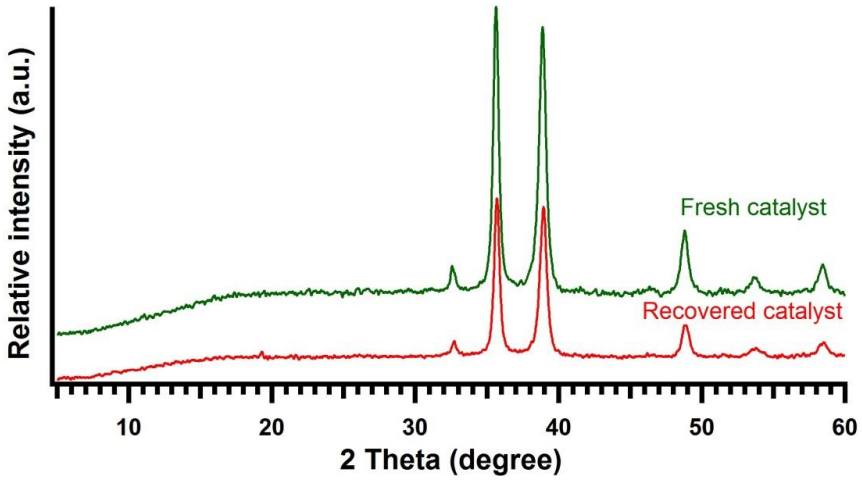

Figure 3.11. XRD patterns of the fresh CuAl $MO_{20\%C}$ catalyst and the recovered catalyst.

The reusability was tested by recycling the spent catalyst in consecutive runs. The catalyst was recovered by centrifuging the reaction mixture, washing with acetone and water and then drying at 200˚C for 12 h. The regenerated catalyst exhibited only a slight catalytic activity loss compared to the fresh catalyst (100% conversion, 100% selectivity) even after the 4^{th} reuse (92% conversion, 100% selectivity) (Figure 3.10). XRD patterns and SEM images of the catalyst before and after the reaction are given in Figure 3.11 and 3.12 and the catalyst did not show any obvious change. The catalytic reaction was performed for 4h and the catalyst was removed by centrifugation followed by filtration and the reaction was continued for an additional 8h to study the possible leaching of the catalyst. However, no considerable change in conversion was observed suggesting that no leaching of the catalyst is taking place under these

reaction conditions. XRD pattern of the catalyst after the reaction under N_2 atmosphere is given in Figure 3.13. The catalyst shows all the characteristic peaks of the CuAl MO catalyst. Apart from that, 3 peaks with relatively high intensity were observed at about 43.30˚, 50.41˚ and 74.10˚ which can be attributed to Cu (0) state.

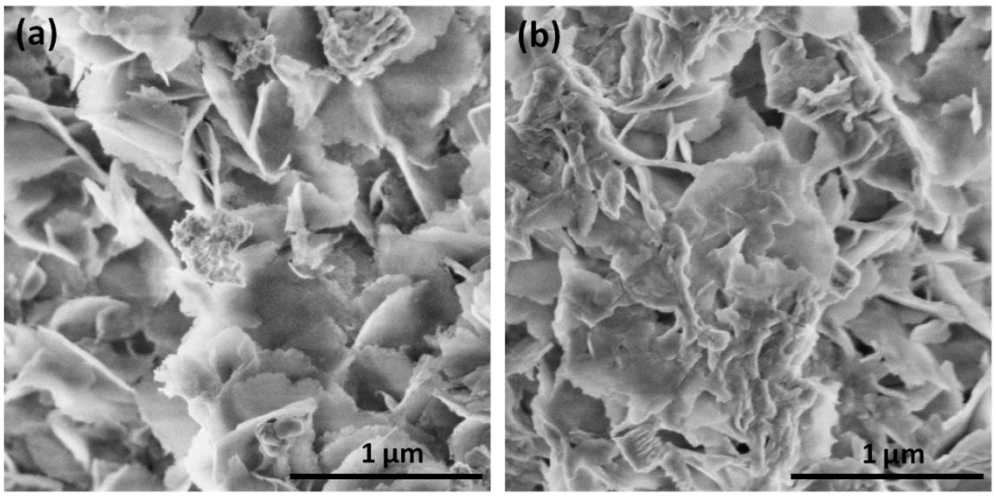

Figure 3.12. FE-SEM images of (a) fresh CuAl $MO_{20\%C}$ catalyst and (b) the recovered catalyst.

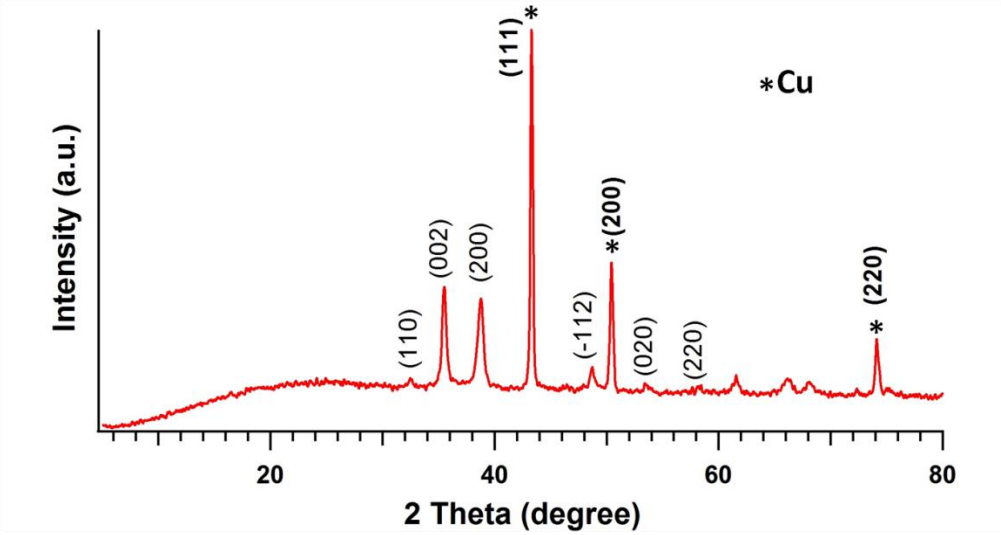

Figure 3.13. XRD pattern of the recovered CuAl $MO_{20\%C}$ catalyst (Reaction performed under N_2 atmosphere).

3.4. Discussion

The application of highly abundant, relatively cheap carbon materials as hard templates has been widely used to synthesize structurally ordered materials with enhanced performances.[28-31] In the current study, activated carbon has been used to alter surface properties of the material and acts as an efficient green catalyst for the synthesis of imines under solvent free conditions. Here, synthesis of mixed metal hydroxide/carbon composite has been achieved through co-precipitation under refluxing conditions from the metal salt solution, urea and activated carbon. The carbon template is removed by thermal treatment in order to obtain the corresponding metal oxide material. In this method, the carbon surface defects and active sites function as nucleation centers for the growth of

metal hydroxide crystallites during synthesis.[31] The crystal and surface structures of the final material (crystallinity, surface area, pore volume, pore diameter) can be modified by adjusting the activated carbon amount in the initial reaction mixture.

N_2 sorption analysis was used to compare the surface properties of materials synthesized in the presence and in the absence of activated carbon template. The CuAl $MO_{20\%C}$ material has the highest specific surface area, pore volume and pore diameter among the series. In this case, activated carbon function as a mold to cast the product and the structure obtained is reciprocal to that of the template. Pore parameters of the template will eventually direct the particle size and pore structure of the final material.[29] According to the current study, the amount of the template has also played a crucial role in determining the surface properties of the final product.

CuAl $MO_{20\%C}$ material showed the highest catalytic activity for the synthesis of imines. The surface properties and surface acidity studies might help to understand the differences in catalytic performance.[32] The superior catalytic activity of CuAl $MO_{20\%C}$ material may be associated with its surface properties.[33] According to FE-SEM images, CuAl MO material synthesized without the carbon template consisted of irregular shaped clusters of particles. However, CuAl $MO_{20\%C}$ sample is composed of a more uniform and organized flower-like microstructure compared to all the other samples. The unique surface morphology, high surface area, additional porosity and uniform pore size

distribution help in diffusion and transportation of reactant molecules in the mesoporous network and this may be the reason for the enhanced activity.[34]

According to the results obtained, it is clear that the alcohol gets oxidized to form the aldehyde and then condense with amine to form the imine product. When the reaction is done without the catalyst under atmospheric conditions, a trace amount of the product is obtained and the aldehyde product is not obtained. This confirms that the oxidation step requires the presence of the catalyst. When the reaction is done under N_2, a conversion of 15% was observed and the XRD pattern of the used catalyst gives peaks corresponding to metallic Cu. The structural oxygen has been used in the oxidation step. This confirms that the presence of the catalyst is essential to carry out the first step. The imine product was observed, when the reaction was started with the aldehyde. However, presence of the catalyst enhances the rate of the second step, giving a higher conversion compared to the uncatalyzed reaction. This second step involves a nucleophilic attack on the *in situ* generated carbonyl and it is generally acid catalyzed.[35] The acidic nature of the CuAl MO catalyst was determined by pyridine adsorption experiments, which is one of the excellent techniques for the characterization of acid sites on heterogeneous solid acid catalysts. According to pyridine adsorption-FTIR spectra (Figure 3.8), peaks observed in the region between 1400 -1550 cm^{-1} arise due to C-C stretching vibrations of pyridine. The peak at 1450 cm^{-1} can be assigned to pyridine adsorbed on Lewis acid sites; the peak at 1538 cm^{-1} is characteristic of pyridine adsorbed on Brønsted acid sites and the peak at 1490 cm^{-1} appears for pyridine adsorbed on both Brønsted and

Lewis acid sites. Adding activated carbon as a structure directing agent significantly enhance the surface area and the pore volume of the catalyst hence present much superior activity as compared with the catalyst synthesized without the carbon material. The key to obtain a high conversion and a high selectivity with the CuAl $MO_{20\%C}$ catalyst is the lower diffusion restrictions and the presence of a higher proportion Lewis acid sites that catalyze the nucleophilic attack step.[22,36]

When the reaction was performed under a N_2 atmosphere, only 15% conversion was obtained, confirming that air was essential as the oxidant. Moreover, obtaining a trace amount of the imine in the absence of the catalyst suggests that the reaction described herein is entirely catalytic in nature. The general applicability of this catalytic system was extended to study different alcohol and amine substrates (Table 3.3). First, the coupling between 4-Chlorobenzyl alcohol and various amine substrates was examined. According to the results, the nucleophilicity of the amine plays a significant role in the reaction process. Propyl amine, which is a primary aliphatic amine, is more basic than other amines hence shows enhanced reactivity. The same trend was observed with 2,4-Dichlorobenzylamine (Table 3.3 - entry 3, pKb = 5.28) , 4-Chlorobenzylamine (Table 3.3 - entry 2, pKb = 4.86) , and 4-Methoxybenzylamine (Table 3.3 - entry 4, pKb = 4.5) where more basic amine substrates give higher conversions. The low basicity of aniline also results in a relatively low rate of nucleophilic attack on the carbonyl carbon to form the imine.[14,37,38]

All the examined alcohol substrates: 2-Propyl alcohol, benzyl alcohol, 4-Mmethoxybenzyl alcohol and 3,4-Dimethoxybenzyl alcohol were oxidized and coupled with benzylamine to produce the desired imine products (Table 3.3 - entry 6-9) in high selectivity. According to the obtained results, the presence of electron donating or withdrawing groups in the aromatic ring plays an important role in determining the conversion. The presence of electron withdrawing groups in the *para* position of the aromatic alcohol results in enhanced conversion (Table 3.3 - entry 6) while the presence of electron donating groups results in lower conversion (Table 3.3 - entry 7, 8). Electron donating groups increase the electron density in the aromatic ring and this results in the difficulty in the oxidation process and the reduced electrophilicity in the formed carbonyl. In contrast, electron withdrawing groups can enhance oxidation and electrophilicity.[39] Compared to other alcohols, 2-Propyl alcohol (which is an aliphatic secondary alcohol) gave a very low conversion (22%) as it is difficult to oxidize them to the corresponding ketone with the current catalyst.

According to the TG-MS profile of CuAl $MO_{0\%C,}$ the weight loss between 100 and 220˚C can be attributed to decomposition of physisorbed water and adsorbed gasses.[40] Second and third weight losses occur due to evolution of surface oxygen and structural oxygen. The final weight loss beyond 700˚C can be attributed to the evolution of lattice oxygen.[41] In contrast to that, the CuAl $MO_{20\%C}$ catalyst shows evolution of surface oxygen starting at room temperature to 400˚C and lattice oxygen beyond 700˚C. These data along with the catalytic data obtained with and without catalyst and XRD studies before and after the

reaction under air and nitrogen atmosphere (Figure 3.11 and 3.13) collectively suggest that surface oxygen availability and facile reversibility of oxygen readsorption (Mars-van Krevelen mechanism) on the surface may account for the superior activity and high durability of the CuAl $MO_{20\%C}$ catalyst.[42,43]

When compared to literature reported studies, this approach involves several advantages. Most reported precious metal based catalysts are significantly more expensive and non-recoverable compared to the catalyst reported in this work. Here, imine synthesis is achieved starting from alcohols and amines and air is used as the environmentally benign terminal oxidant. From the point of view of green chemistry, removing the solvent from a chemical process is one of the most important steps in the reduction (energy,waste, *etc.*) and simplification in the work-up as well as the reaction. This catalyst gives very high conversions and selectivities for the synthesis of imine compounds under solvent free conditions. Due to all these reasons, this can be considered as a green catalyst superior to other reported heterogeneous catalytic systems.

3.5. Conclusions

In conclusion, an efficient and a green catalytic process to synthesize imines directly from alcohols and amines using CuAl MO catalyst has been reported. CuAl $MO_{20\%C}$ material exhibited a uniform pore size distribution (pore diameter 40 Å) with the highest surface area (161 m^2/g) and showed the best catalytic performance. CuAl MO catalyzes two distinct processes, oxidation

followed by imine formation in a single reaction vessel under the same reaction conditions. Diverse types of substituted imines can be obtained with 100% selectivity without any base additives or precious metal catalysts. The reaction is aerobic, environmentally benign and proceeds under solvent free conditions. The method has a versatile scope for various alcohols and amines and CuAl MO catalyst can be reused several times without remarkable loss of its catalytic activity. These types of mesoporous metal oxides are capable of acting as superior heterogeneous catalysts because of their intrinsic features of high surface area and tunable pore sizes and the high surface area provides a higher concentration of active sites per unit mass of substrate. Therefore, CuAl MO catalyst reported here can be applied in several other Lewis acid catalyzed reactions such as Diels-Alder reaction, Friedel-Crafts reaction, and aldol reaction.

References

(1) Robert, C.; Thomas, C. M. Tandem catalysis: a new approach to polymers. *Chem. Soc. Rev.* **2013**, *42*, 9392-9402.

(2) Climent, M. J.; Corma, A.; Iborra, S. Homogeneous and heterogeneous catalysts for multi component reactions. *RSC Adv.* **2012**, **2**, 16-58.

(3) Climent, M. J.; Corma, A.; Iborra, S. Heterogeneous Catalysts for the One-Pot Synthesis of Chemicals and Fine Chemicals. *Chem. Rev.* **2011**, *111,* 1072-1133.

(4) Climent, M. J.; Corma, A.; Iborra, S.; Sabater, M. J. Heterogeneous Catalysis for Tandem Reactions. *ACS Catal.* **2014**, *4*, 870-891.

(5) Pérez, J. M.; Cano, R.; Yus, M.; Ramón, D. J. Straightforward Synthesis of Aromatic Imines from Alcohols and Amines or Nitroarenes Using an Impregnated Copper Catalyst. *Eur. J. Org. Chem.* **2012**, *24*, 4548-4554.

(6) Patil, R. D.; Adimurthy, S. Copper-Catalyzed Aerobic Oxidation of Amines to Imines under Neat Conditions with Low Catalyst Loading. *Adv. Synth. Catal.* **2011***, 353*, 1695-1700.

(7) Tian, H.; Yu, X.; Li, Q.; Wang, J.; Xu, Q. General, Green, and Scalable Synthesis of Imines from Alcohols and Amines by a Mild and Efficient Copper-Catalyzed Aerobic Oxidative Reaction in Open Air at Room Temperature. *Adv. Synth. Catal.* ***2***0**12***, 354*, 2671-2677.

(8) Gnanaprakasam, B.; Zhang, J.; Milstein, D. Direct Synthesis of Imines from Alcohols and Amines with Liberation of H_2. *Angew. Chem. Int. Ed.* **2010***, 49*, 1468-1471.

(9) Soule, J.; Miyamura, H.; Kobayashi, S. Selective imine formation from alcohols and amines catalyzed by polymer incarcerated gold/palladium alloy nanoparticles with molecular oxygen as an oxidant. *Chem. Commun.*, **2013**, *49*, 355-357.

(10) Donthiri, R. R.; Patil, R. D.; Adimurthy, S. NaOH-Catalyzed Imine Synthesis: Aerobic Oxidative Coupling of Alcohols and Amines. *Eur. J. Org. Chem.* **2012***, 24*, 4457-4460.

(11) Grirrane, A.; Corma, A.; Garcia, H. Highly active and selective gold catalysts for the aerobic oxidative condensation of benzylamines to imines and one-pot, two-step synthesis of secondary benzylamines. *J. Catal.* **2009***, 264*, 138-144.

(12) Zhu, B.; Lazar, M.; Trewyna, B,J.; Angelici, R.J. Aerobic oxidation of amines to imines catalyzed by bulk gold powder and by alumina-supported gold. *J. Catal.* **2008**, *260*, 1-6.

(13) Yuan, H.; Yoo, W.; Miyamura, H.; Kobayashi, S. Discovery of a Metalloenzyme-like Cooperative Catalytic System of Metal Nanoclusters and Catechol Derivatives for the Aerobic Oxidation of Amines. *J. Am. Chem. Soc.* **2012**, *13*4, 13970-13973.

(14) Huang, H.; Huang, J.; Liu, Y.; He, H.; Cao, Y.; Fan, K. Graphite oxide as an efficient and durable metal-free catalyst for aerobic oxidative coupling of amines to imines. *Green Chem.*, **2012**, *14*, 930-934.

(15) Hu, Z.; Kerton, F. M. Simple copper/TEMPO catalyzed aerobic dehydrogenation of benzylic amines and anilines. *Org. Biomol. Chem.*, **2012**, *10*, 1618-1624.

(16) Liu, P.; Li, C.; Hensen, E. J. M. Efficient Tandem Synthesis of Methyl Esters and Imines by Using Versatile Hydrotalcite-Supported Gold Nanoparticles. *Chem. Eur. J.* **2012***, 18*, 12122-12129.

(17) Xu, J.; Zhuang, R.; Bao, L.; Tang, G.; Zhao, Y. KOH-mediated transition metal-free synthesis of imines from alcohols and amines. *Green Chem.*, **2012**, *14,* 2384-2387.

(18) Likhar, P. R.; Arundhathi, R.; Kantam, M. L.; Prathima, P. S. Amination of Alcohols Catalyzed by Copper-Aluminium Hydrotalcite: A Green Synthesis of Amines. *Eur. J. Org. Chem.* **2009***, 31,* 5383-5389.

(19) Kwon, M. S.; Kim, S.; Park, S.; Bosco, W.; Chidrala, R. K.; Park. J. One-Pot Synthesis of Imines and Secondary Amines by Pd-Catalyzed Coupling of Benzyl Alcohols and Primary Amines. *J. Org. Chem.* **2009**, *74*, 2877-2879.

(20) Ali, E.; Naimi-Jamal, M. R.; Dekamin, M. G. Highly efficient and rapid synthesis of imines in the presence of nano-ordered MCM-41- SO_3H heterogeneous catalyst. *Sci. Iranica* **2013***, 20*, 592-597.

(21) Nicolaou, K. C.; Mathison, C. J. N.; Montagnon, T. New Reactions of IBX: Oxidation of Nitrogen- and Sulfur-Containing Substrates to Afford Useful Synthetic Intermediates. *Angew. Chem. Int.Ed.* **2003***, 42*, 4077-4082.

(22) Poyraz , A. S.; Kuo, C-H.; Kim, E.; Meng, Y.; Seraji, M. S.; Suib, S. L. Tungsten-Promoted Mesoporous Group 4 (Ti, Zr, and Hf) Transition-Metal

Oxides for Room-Temperature Solvent-Free Acetalization and Ketalization Reactions. *Chem. Mater.*, **2014**, *26*, 2803-2813.

(23) Pahalagedara, M. N.; Samaraweera, M.; Dharmarathna, S.; Kuo, C-H.; Pahalagedara, L. R.; Gascon, J.A.; Suib, S.L. Removal of Azo Dyes: Intercalation into Sonochemically Synthesized NiAl Layered Double Hydroxide. *J. Phys. Chem. C.* **2014**, *118*, 17801-17809.

(24) Yu, Q.; Huang, H.; Chen, R.; Wang, P.; Yang, H.; Gao, M.; Peng, X.; Ye, Z. Synthesis of CuO nanowalnuts and nanoribbons from aqueous solution and their catalytic and electrochemical properties. *Nanoscale,* **2012***, 4,* 2613-2620.

(25) Liu, B. One-dimensional copper hydroxide nitrate nanorods and nanobelts for radiochemical applications. *Nanoscale*, **2012**, *4*, 7194-7198.

(26) Zhao, B.; Liu, P.; Zhuang, H.; Jiao, Z.; Fang, T.; Xu, W.; Lu, B.; Jiang, Y. Hierarchical self-assembly of microscale leaf-like CuO on graphene sheets for high-performance electrochemical capacitors. **J. Mater. Chem. A, 2013**,**1**, 367-373.

(27) Xia, H.; Yang, G. Facile synthesis of inorganic nanoparticles by a precipitation method in molten epsilon-caprolactam solvent. *J. Mater. Chem.*, **2012**, *22*, 18664-18670.

(28) Pahalagedara, L.; Sharma, H.; Kuo, C-H.; Dharmarathna, S.; Joshi, A.; Suib, S.L, Mhadeshwar, A.B. Structure and Oxidation Activity Correlations for Carbon Blacks and Diesel Soot. *Energy Fuels*, **2012**, *26*, 6757-6764.

(29) Zhu, K.; Sun, J.; Zhang, H.; Liu, J.; Wang, Y. Carbon as a hard template for nano material catalysts. *Journal of Natural Gas Chemistry* **2012***, 21*, 215-232.

(30) Goodman, M. D.; Arpin, K. A.; Mihi, A.; Tatsuda, N.; Yano, K.; Braun, P. V. Enabling New Classes of Templated Materials through Mesoporous Carbon Colloidal Crystals. *Adv.Optical Mater.* **2013***, 1*, 300-304.

(31) Malak-Polaczyk , A.; Vix-Guterl , C.; Frackowiak , E. Carbon/Layered Double Hydroxide (LDH) Composites for Supercapacitor Application. *Energy Fuels* **2010**, *24*, 3346-3351.

(32) Kuo, C.; Poyraz, A. S.; Jin, L.; Meng, Y.; Pahalagedara, L.; Chen, S.; Kriz, D. A.; Guild, C.; Gudz, A.; Suib, S. L. Heterogeneous acidic TiO_2 nanoparticles for efficient conversion of biomass derived carbohydrates. *Green Chem.***, 2014**, *16*, 785-791.

(33) Pahalagedara, M. N.; Pahalagedara, L. R.; Kuo, C-H.; Dharmarathna, S.; Suib, S. L. Ordered Mesoporous Mixed Metal Oxides: Remarkable Effect of Pore Size on Catalytic Activity. *Langmuir*, **2014**, *30,* 8228-8237.

(34) Xu, L.; Sithambaram, S.; Zhang, Y.; Chen, C-H.; Jin, L.; Joesten, R.; Suib, S. L. Novel Urchin-like CuO Synthesized by a Facile Reflux Method with Efficient Olefin Epoxidation Catalytic Performance. *Chem. Mater.* **2009**, *21*, 1253-1259.

(35) Sithambaram, S.; Kumar, R.; Son, Y.; Suib, S. L. Tandem catalysis: Direct catalytic synthesis of imines from alcohols using manganese octahedral molecular sieves. *J. Catal.* **2008***, 253*, 269-277.

(36) Mallesham, B.; Sudarsanam, P.; Raju, G.; Reddy, B. M. Design of highly efficient Mo and W-promoted SnO_2 solid acids for heterogeneous catalysis: acetalization of bio-glycerol. *Green Chem.* **2013, 15**, 478-489.

(37) Kegnaes, S.; Mielby, J.; Mentzel, U. V.; Christensen, C. H.; - Riisager, A. Formation of imines by selective gold-catalysed aerobic oxidative coupling of alcohols and amines under ambient conditions. *Green Chem.* **2010**, *12*, 1437-1441.

(38) Jiang, L.; Jin, L.; Tian, H.; Yuan, X.; Yu, X.; Xu, Q. Direct and mild palladium-catalyzed aerobic oxidative synthesis of imines from alcohols and amines under ambient conditions. *Chem. Commun.* **2011, 47**, 10833-10835.

(39) Chen, B.; Li, J.; Dai, W.; Wang, L.; Gao, S. Direct imine formation by oxidative coupling of alcohols and amines using supported manganese oxides under an air atmosphere. *Green Chem.* **2014, 16,** 3328-3334.

(40) Vijaya Kumar, R.; Elgamiel, R.; Diamant, Y.; Gedanken, A. Sonochemical Preparation and Characterization of Nanocrystalline Copper Oxide Embedded in Poly(vinyl alcohol) and Its Effect on Crystal Growth of Copper Oxide. *Langmuir,* **2001**, *17*, 1406-1410.

(41) Pahalagedara, L. R.; Poyraz , A. S.; Song, W.; Kuo, C-H.; Pahalagedara, M. N.; Meng, Y.; Suib, S. L. Low Temperature Desulfurization of H2S: High Sorption Capacities by Mesoporous Cobalt Oxide via Increased H_2S Diffusion. *Chem. Mater.* **2014**, *26*, 6613-6621.

(42) Doornkamp, C.; Ponec, V. The universal character of the Mars and Van Krevelen mechanism. *J. Mol. Catal. A: Chem.* **2000***, 162*, 19-32.

(43) Genuino, H. C.; Meng, Y.; Horvath, D. T.; Kuo, C.; Seraji, M. S.; Morey, A. M.; Joesten, R. L.; Suib, S. L. Enhancement of Catalytic Activities of Octahedral Molecular Sieve Manganese Oxide for Total and Preferential CO Oxidation through Vanadium Ion Framework Substitution. *Chem. Cat. Chem.* **2013***, 5*, 2306-2317.

CHAPTER IV. ROOM TEMPERATURE SELECTIVE REDUCTION OF NITROBENZENE TO AZOXYBENZENE OVER MAGNETICALLY SEPARABLE NI/GRAPHENE NANOCOMPOSITE CATALYST

4.1. Introduction

Selective catalytic reduction of nitrobenzene is an important reaction for the synthesis of intermediates and is a precursor to various industrially valuable products such as aniline, nitroso benzene, azo benzene and azoxy benzene.[1,2] Among them, azoxy benzene is one of the most important and essential building blocks of naturally occurring compounds and functional materials due to its conjugated system and polar functionality.[3-5] In addition, azoxy benzene is valuable both as an intermediate and high-value compound widely used in industry such as dyes, reducing agents, polymerization inhibitors and chemical stabilizers. Some azoxy benzene derivatives are used as liquid crystals in electronic displays and therapeutic medicines.[6,7] Moreover, these types of compounds are precursors for Wallach rearrangements, which offer a simple route to synthesize hydroxyazobenzene.[8,9]

Azoxy benzene is produced as an intermediate in the oxidation of aniline or the reduction of nitroarenes via the condensation of nitrosobenzene and hydroxylamine. These reaction steps are quite complex and lead to different intermediates. Therefore, manipulation of reaction conditions while controlling the

selectivity to the azoxy product in the midst of all possible reduction/oxidation products becomes an important research interest.[10]

Various methods have been reported for oxidative coupling of aniline using different oxidants like peraacetic acid, $Pb(OAc)_4$, [11] $Hg(OAc)_2$ and different types of molecular sieves. [12,13] Reducing nitroarenes by alkaline metal borohydrides and metals such as samarium and thallium were also reported in few studies.[14] However, most of these methods lack environmental benignity and the recyclability of the catalyst. Therefore, finding alternative, more benign catalysts that works under atmospheric pressure and comparatively low temperature for producing azoxy benzene with high conversion and selectivity is in high demand.

We report here the preparation of a Ni/Graphene (Ni/G) nanocomposite for the complete reduction of nitrobenzene to azoxybenzene with 100% selectivity under mild conditions. The nanosize of these materials leads to a high surface area to volume ratio and therefore, to an enhanced contact between reactants and catalyst, which increases the activity dramatically. Here, hydrazine hydrate ($N_2H_4.H_2O$) is used which can be considered as a very suitable reagent for the reduction of nitro groups, as it generates only N_2 and water as byproducts.[15] Graphene acts as a promising catalyst support with a high surface area on which the metal nanocatalyst can be stabilized. Graphene prevents metal nanoparticle aggregation and provides desired chemical interface between the catalyst and the reaction media thus results in enhanced catalytic performance. Moreover, the catalyst is magnetic and could be easily retrieved

from the reaction mixture and reused by simple magnetic separation after the completion of the reaction.

4.2. Experimental Section

4.2.1. Catalyst Preperation

4.2.1.1. Synthesis of Graphene oxides (GO)

GO was synthesized from natural graphite using a modified Hummers method. Briefly, graphite powder (1 g) and $NaNO_3$ (2 g) were mixed and added into concentrated H_2SO_4 (48 mL; 98%) in an ice bath. Under vigorous stirring, KMnO4 (4 g) was gradually added and the temperature of the mixture was kept below 20˚C. After removing the ice bath, the mixture was stirred at 35˚C in a water bath for 6 h. Then, 200 mL water was slowly added to the mixture in an ice bath. After the dilution, 15ml of 30% H_2O_2 was added to the mixture and stirred for another 2 h. The mixture was filtered and washed with distilled water and then re-dispersed in water by ultrasonication. Finally the product was separated by centrifugation and vacuum dried at 45˚C for 48 h.

4.2.1.2. Synthesis of Ni nanomaterial

First, $NiCl_2.6H_2O$ was dispersed in 10 mL of ethanol in order to prepare a 0.25 M solution. Then, 1 mL of KOH solution (0.2 M) and 1 mL of hydrazine

hydrate solution (85%) was added under vigorous stirring at 60˚C and the obtained mixture was refluxed at 100˚C for 2 h. The reaction was cooled to room temperature, and the resultant product was washed with distilled water and ethanol for three times and separated by centrifugation. Finally the product was dried in a vacuum oven at 60˚C for 12 h.

4.2.1.3. Synthesis of Ni/ Graphene nanocomposite

About 15 mL of 1 mg/mL GO suspension was prepared by ultrasonication and the resultant solution was added to the 0.25 M $NiCl_2.6H_2O$ solution and the same procedure was followed to synthesize of Ni/ Graphene nanocomposite.

4.2.2. Catalyst characterization

4.2.2.1. X-Ray Powder Diffraction Studies

Powder X-ray diffraction (XRD) analyses were performed on a Rigaku Ultima IV diffractometer with Cu Kα(λ = 0.15406 nm) radiation with a beam voltage of 40 kV and a beam current of 44 mA. Continuous scans were taken in a 2θ range of 5-80˚ with a scanning rate of 2.0 ˚/min, and the phases were identified using the International Center for Diffraction Data (ICDD) database.

4.2.2.2. Raman Spectroscopy

Raman measurements were taken at room temperature on a Renishaw 2000 Ramascope attached to a charge-coupled device (CCD) camera, with an

Ar^+ ion laser (514.4 nm) as the excitation source. Before each measurement was taken, the spectrometer was calibrated with a silicon wafer. Curve fitting for the determination of spectral parameters was performed with the software program GRAMS/32.

4.2.2.3. N_2 Sorption Studies

The nitrogen sorption experiments were performed using Quantachrome Autosorb iQ_2 instrument instrument using N_2 gas as the adsorbate at 77 K by a multipoint method. The Brunauer- Emmett-Teller (BET) method was used to determine the specific surface area and the Barrett-Joyner-Halenda (BJH) desorption method was used to calculate the pore size distribution and pore volume. Prior to the analysis, all the samples were degassed at 150˚C for 12 h in order to remove any adsorbed species.

4.2.3. Catalytic Activity Measurements

Liquid phase reduction of nitrobenzene was carried out at room temperature (25˚C) in a double neck round bottom flask in an oil bath using 0.025 g catalyst, 5 mL ethanol, 1.1 mL hydrazine and 1.5 mL nitrobenzene. Small aliquots of were collected from the reaction mixture at regular intervals for analysis. For the reusability test, the spent catalyst was recovered from the reaction mixture by magnetic separation and washed thoroughly with acetone and dried at 120˚C for 12 h. The gas chromatography-mass spectroscopy (GC-MS) method was used for the quantitative analysis and identification of the

reaction product. Analyses were performed using a HP 5971 mass selective detector coupled to a HP 5890 Series II gas chromatograph equipped with a thermal conductivity detector (TCD) through an HP-1 (nonpolar cross-linked methyl siloxane) column with dimensions of 12.5 m × 0.2 mm ×0.33 μm.

4.3. Results

4.3.1. Structure and characterization

XRD patterns of as synthesized Ni nanomaterial and Ni/G composite are displayed in Figure 4.1. Both samples exhibit three well-resolved peaks at 2θ = 44.5˚, 51.8˚, and 76.4˚, which coincide with the (111), (200), and (220) planes of pure face centered cubic structure. No other peaks were observed, indicating the high purity of as-prepared samples. XRD pattern of commercial Ni powder is also given as a reference (Figure 4.1a). Ni/G composite sample shows an additional small and low broad peak around 2θ = 26.5˚, which can be indexed into the disordered amorphous graphene sheets. This suggests that, graphene is successfully incorporated into the Ni nanomaterial.[16]

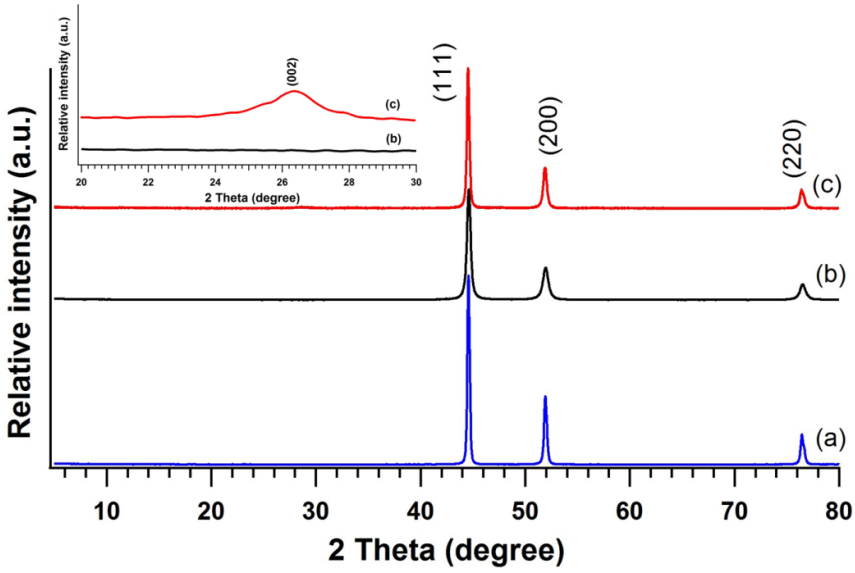

Figure 4.1. X-ray diffraction patterns of (a) commercial Ni powder (b) Ni nanomaterial and (c) Ni/G composite

Table 4.1. Structural parameters of Ni nanomaterial, Ni/G composite and GO sample

Catalyst	BET SA (m^2/g)	BJH desorption pore volume (cm^3/g)	BJH desorption pore diameter (nm)
Ni nanomaterial	16	0.08	3.4
Ni/G composite	93	0.17	3.6
GO	18	0.04	4.2

As synthesized Ni nanocomposite, Ni/G composite were analyzed by N_2 sorption measurements to study their textural properties and pore size distributions. N_2 adsorption/desorption isotherms and BJH pore size distributions

of the obtained materials are presented in Figures 4.2a and b. The BET surface areas of Ni nanomaterial and Ni/G composite are 16 and 93 m^2/g, respectively. Upon incorporation of graphene, pore volume also has been increased from 0.085 to 0.17 cm^3/g (Table 4.1). Ni/G composite shows a larger N_2 uptake than the Ni sample and it indicates a higher mesopore volume. The Ni/G composite resembles a type-H3 IUPAC classification, which may result from slit-shaped pores between parallel layers in graphene.[17,18] BJH pore diameter showed a slight increase upon graphene incorporation. However, Ni/G composite possesses a higher amount of pores in the mesoporous region, with a uniform size distribution (Figures 4.2a). N_2 adsorption/desorption isotherm and BJH pore size distribution curve of as synthesized GO sample is given in Figure 4.3.

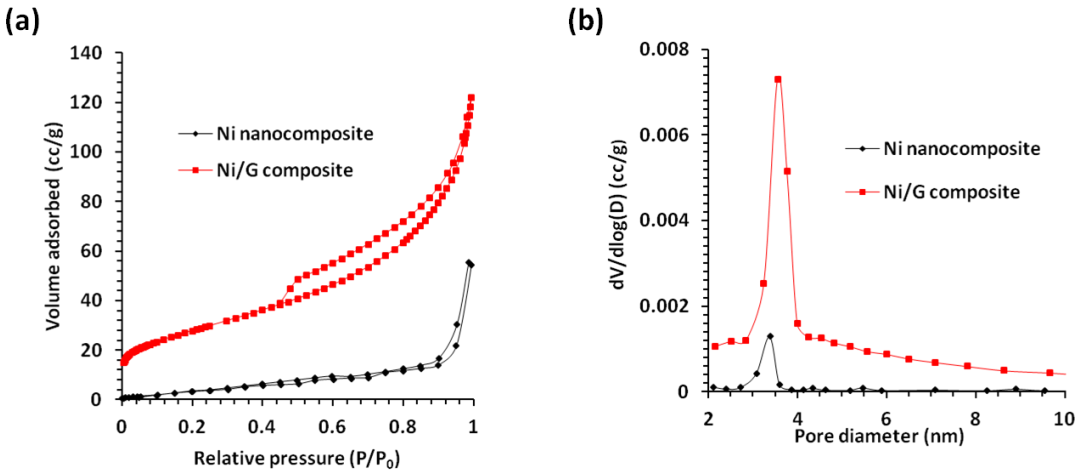

Figure 4.2. (a) N_2 adsorption/desorption isotherms and (b) BJH pore size distribution curves of Ni nanomaterial and Ni/Graphene composite

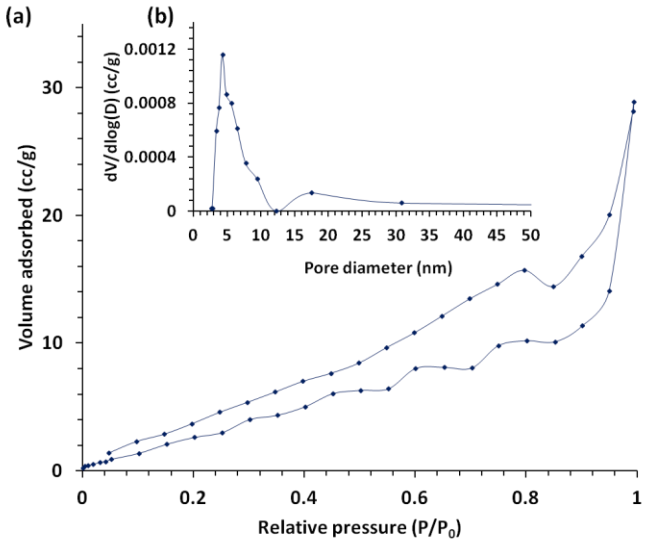

Figure 4.3. (a) N_2 adsorption/desorption isotherms and (b) BJH pore size distribution curves of as synthesized GO sample

As synthesized samples were examined by Raman spectroscopy and results are given in Figure 4.4. Ni nanomaterial did not show any detectable peaks in the region between 800 - 2000 cm^{-1}. Raman spectra of GO and Ni/Graphene nanocomposite give 2 intense peaks at 1350 and 1600 cm^{-1} (Figure 4b and c). The intensity ratio between the bands at 1600 and 1350 cm^{-1} has been decreased upon reduction with hydrazine.

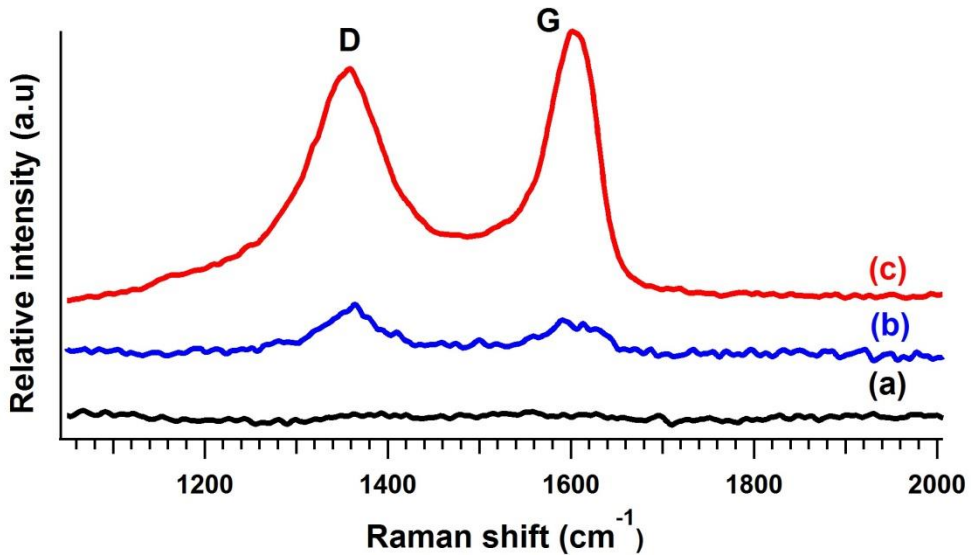

Figure 4.4. Raman spectra of (a) Ni nanomaterial (b) GO and (C) Ni/Graphene composite

4.3.2. Catalytic activity

The catalytic activity of Ni and Ni/G composite towards the reductive coupling of nitrobenzene to azoxybenzene was investigated at room temperature and at atmospheric pressure using ethanol as the solvent and hydrazine monohydrate as the reducing agent. Activities of as synthesized Ni nanomaterial and Ni/G composite in nitrobenzene and nitro cyclohexane reduction were tested and the obtained results are summarized in Table 4.2. Ni/Graphene composite gave 100% conversion with 100% selectivity towards the desired azoxy product in 2 h; therefore all the reactions were carried out for two hours under same experimental conditions. Ni nanomaterial gave a 73.3% nitrobenzene conversion with 80.9% selectivity towards azoxybenzene (entry 1). Commercial Ni could only

give the azoxy product with a conversion of 1.7% (17.6% selectivity) while aniline was the major product.

Table 4.2. Reductive coupling of nitrobenzene to azoxybenzene.[a]

Entry	Catalyst	Nitrobenzene conversion (%)[h]	Selectivity (%)[i]			Turnover number (TON)[j]	Turnover Frequency (TOF)[k]
			Aniline	Azo benzene	Azoxy benzene		
1	Ni nanomaterial	73	12	8	80	12.8	6.43
2	Ni nanomaterial [b]	100	12	0	88	17.6	-
3	Ni/G nanocomposite	100	0	0	100	36.2	18.10
4	Commercial Ni	2	82	0	18	0.30	0.15
5	Ni/G nanocomposite[c]	100	0	32	68	36.2	18.10
6	Ni/G nanocomposite[d]	100	0	44	56	36.2	18.10
7	Ni/G nanocomposite[e]	75	15	0	85	27.1	13.55
8	Ni/G nanocomposite[f]	100	30	0	70	36.2	18.10
9	Ni/G nanocomposite[g]	93	0	0	100	33.6	16.80
10	Graphene	5	100	0	0	-	-
11	No catalyst	1	100	0	0	-	-

[a] Reaction conditions : solvent (ethanol) = 5 mL, substrate (nitrobenzene) = 15 mmol, nitrobenzene: hydrazine (molar ratio) = 1:1.5, 0.025 g catalyst, room temperature, reaction time = 2 h. Conversion and selectivity determined and confirmed by GC-MS. [b] Reaction after 24 h (TOF was not calculated). The reaction temperatures were [c]50, [d]80˚C respectively. Nitrobenzene: hydrazine (molar ratio) = 1:0.5[e] and 1:2.5[f] respectively. [g] Catalyst after 4 cycles. [h]Nitrobenzene conversion = [moles of nitrobenzene converted/ moles of nitrobenzene used] x 100. [i]Selectivity = [Total moles of the product formed/ Total moles of nitrobenzene converted]. [j]Turnover number (TON) = [moles of converted substrate] x (moles of Nickel)$^{-1}$. [k]Turnover frequency (TOF) = [moles

of converted substrate] x [(moles of Nickel) x (reaction time in h)]$^{-1}$.(-) = not calculated.

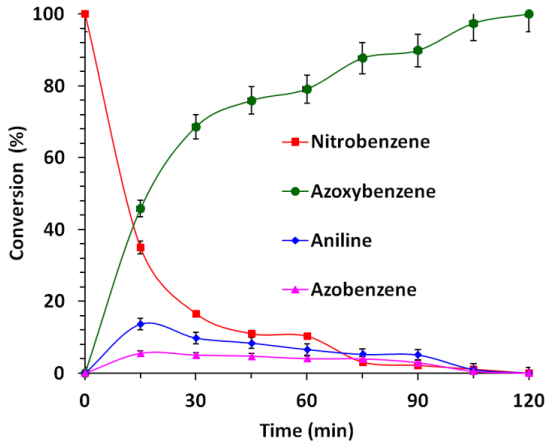

Figure 4.5. Time-conversion plot for nitrobenzene reduction by Ni/G composite at room temperature.

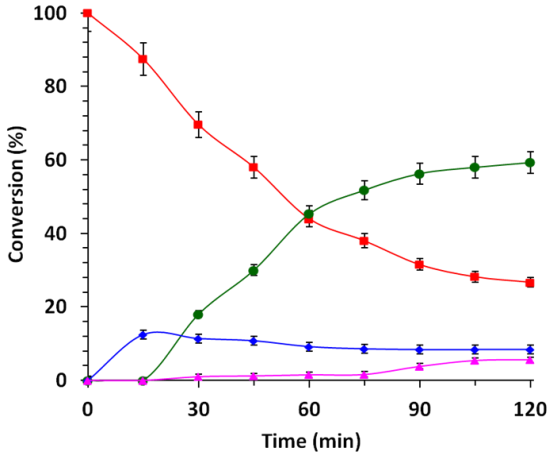

Figure 4.6. Time-conversion plot for nitrobenzene reduction by Ni nanomaterial at room temperature.

A series of catalytic experiments was carried out using Ni/Graphene composite in order to understand the variation of nitrobenzene to azoxybenzene as a function of time, temperature and nitrobenzene: hydrazine molar ratio.

Figure 4.5 gives the time-conversion plot for nitrobenzene reduction at room temperature. Here, aniline and azobenzene were formed as byproducts, however they were gradually converted to azoxybenzene with increasing time. Same trend was observed with Ni nanomaterial (Figure 4.6), but nitrobenzene conversion rate was low compared to the previous catalyst. After 24h of reaction, Ni nanomaterial exhibited 100% conversion with 88.4% azoxybenzene selectivity (Table 4.2, entry 2). Although the reactions performed at different temperatures (50˚C and 80˚C), gave 100% conversion, the selectivity drops due to the formation of azobenzene as the major side product (Figure 4.7).

Then, the effect of nitrobenzene to hydrazine molar ratio was studied at room temperature while keeping all the other experimental parameters constant. When nitrobenzene : hydrazine was adjusted to 1:0.5, the conversion was comparatively low (75%) with the azoxybenzene selectivity of 85% and aniline selectivity of 15%. 100% conversion and selectivity towards the desired azoxybenzene product was observed when the ratio was 1:1.5. With a further increase up to 1:2.5, although the conversion was 100%, azoxybenzene selectivity decreased significantly to 70%, owing to the formation of aniline as the major side product (Figure 4.8).

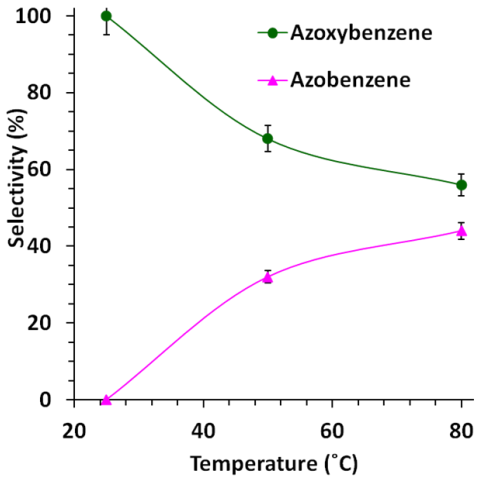

Figure 4.7. Effect of temperature on nitrobenzene reduction

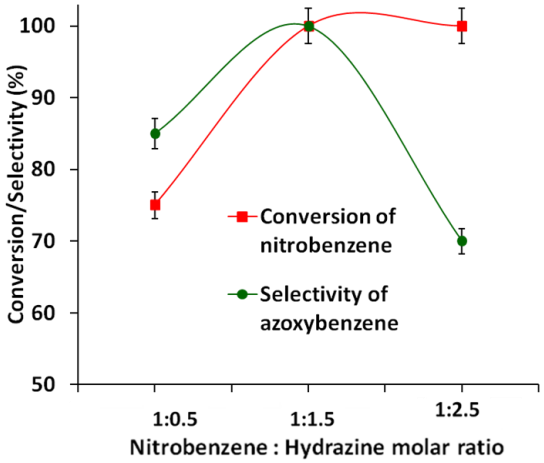

Figure 4.8. Effect of the nitrobenzene: hydrazine molar ratio on nitrobenzene reduction

Blank experiments were performed with graphene and in the absence of the catalyst in order to confirm the catalytic nature of the present catalyst. Graphene showed a 4.5% conversion after 2 h. Reaction carried out without the

catalyst gave a very small conversion (0.5%). In both reactions, aniline was the only product detected from GC (Table 4.2, entry 10 & 11).

The reusability was tested by recycling the spent catalyst in consecutive runs. The catalyst was recovered from the reaction mixture by magnetic separation and washed thoroughly with acetone and dried at 120˚C for 12 h. Over a period of four reaction cycles under the same conditions, no significant loss of activity was observed (93 % conversion, 100% selectivity after the 4^{th} reuse).

4.4. Discussion

This study reports the synthesis of magnetic Ni/G nanocomposite that acts as a promising catalyst in the selective reduction of nitrobenzene to azoxybenzene at room temperature and under atmospheric pressure. Here, the composite is synthesized via the reduction of Ni^{2+} and GO in a single step where hydrazine monohydrate is used as the reducing agent.[17,19] Oxygen containing groups in GO, such as –OH and –COOH facilitate the homogeneous dispersion of Ni^{2+}on its surface and both Ni^{2+} and GO are simultaneously reduced by hydrazine. Therefore, this can be considered as an insitu-reduction growth process. The decrease in the intensity ratio between G band (1600 cm^{-1}) and D band (1350 cm^{-1}) in Raman spectroscopy confirms the successful reduction of GO and it agrees with previous reports.[20,21]

Enhancement of the catalytic activity by graphene incorporation can be explained in two ways. As a catalyst support, there is inhibition of the aggregation

of active Ni nanoclusters by dispersing them on the surface and provides a desired chemical interface between the catalyst and the reaction media. On the other hand, graphene can absorb nitrobenzene via π-π stacking interactions, and again improves contact between the reactant and the catalyst surface and facilitates transportation of electrons from graphene to Ni nanomaterial.[1]

Ni/Graphene nanocomposite showed the highest catalytic activity for the synthesis of azoxybenzene with 100% selectivity. Although it takes 2 h to give a complete conversion, about 65% of nitrobenzene is converted within first 15 minutes. According to Figure 4.5, there is no induction period for this catalyst.Aniline and azobenzene were found as side products; however they were gradually transformed to azoxybenzene with time.

The mechanism of the catalyzed reduction of nitroarenes to azoxybenzene can be explained by a redox mechanism. As a reagent, hydrazine is oxidized generating electrons necessary for the reduction and N_2 gas and water is produced. These electrons reduce nitrobenzene to nitrosobenzene and further reduction results in the formation of phenylhydroxylamine. Condensation of nitrosobenzene and phenylhydroxylamine forms azoxybenzene as the major product in the reaction medium. Further reduction of phenylhydroxylamine and azoxybenzene may produce aniline and azobenzene as side products. According to catalytic data (Table 4.2), these side products are formed and promoted by higher temperatures and higher concentrations of hydrazine. Therefore, the process described here can be considered as a promising approach to obtain the

azoxy product with a high selectivity (100%) in the midst of all possible reduction products.

Another remarkable feature of the Ni/G nanocomposite is that this material can be readily isolated from the reaction medium due to its magnetic nature. Catalyst reusability is of major importance in heterogeneous catalysis and development of new technologies for catalyst separation and recycling to substitute traditional time- and solvent-consuming procedures is a challenge for green chemistry. Therefore, the catalyst described here can be considered as an environmentally friendly green catalyst which provides a convenient route for the catalyst recovery by the application of an external permanent magnet. [22,23]

4.5. Conclusions

In conclusion, an efficient catalytic process to selectively synthesize azoxybenzene under mild reaction conditions has been reported. Ni/G nanocomposite material exhibited the highest catalytic performance giving 100% conversion with 100% selectivity towards the desired product in 2 h at room temperature and under atmospheric pressure. This catalyst system can be applied to reduce diverse types of substituted nitroarenes into their corresponding azoxy products. Ni/G nanocomposite is magnetically separable and can be reused several times without any significant loss of its initial catalytic potential. Therefore, this catalytic system offers several advantages for the preparation of azoxybenzenes from the corresponding nitroarene such as mild

conditions, low catalyst loading, high conversions and selectivities, which yield an efficient and attractive methodology for organic synthesis.

References

(1) Grirrane, A.; Corma, A.; García, H. Gold-Catalyzed Synthesis of Aromatic Azo Compounds from Anilines and Nitroaromatics. *Science* **2008***, 322*, 1661-1664.

(2) Chang, C.-F.; Liu, S.-T. Catalytic oxidation of anilines into azoxybenzenes on mesoporous silicas containing cobalt oxide. *J. Mol. Catal. A: Chemical* , **2009**, *299*, 121-126.

(3) Hamon, F.; Djedaini-Pilard, F.; Barbot, F.; Len, C. Azobenzenes - synthesis and carbohydrate applications. *Tetrahedron* , **2009**, *65*, 10105-10123.

(4) Burkhardt, E.R.; Ma, K. Boron Reagents in Process Chemistry: Excellent Tools for Selective Reductions. *Chem. Rev.* **2006,** *106*, 2617-2650.

(5) Sakaue, S.; Tsubakino, T.; Nishiyam, Y.; Ishii, Y. Oxidation of aromatic amines with hydrogen peroxide catalyzed by cetylpyridinium heteropolyoxometalates. *J. Org. Chem.* **1993**, *58*, 3633-3638.

(6) Acharyya, S.; Ghosh, S.; Bal, R. Catalytic Oxidation of Aniline to Azoxybenzene Over $CuCr_2O_4$ Spinel Nanoparticle Catalyst. ACS Sustainable Chem. Eng. **201**4, *2*, 584-589.

(7) Buncel, E. 1999 R.U. Lemieux Award Lecture Adventures with azo-, azoxy-, and hydrazoarenes: from the Wallach to the benzidine rearrangement. Molecular electronics. - *Can. J. Chem*., **2000**, *78*, 1251-1271.

(8) Buncel, E. Catalysis in strongly acidic media and the Wallach rearrangement. *Acc. Chem. Res*, **1975**, *8*,132-139.

(9) Zhu, H.; Lu, Y.; Fan, F.; Yu, S. Selective hydrogenation of nitroaromatics by ceria nanorods. *Nanoscale* , **2013**, *5*, 7219-7223.

(10) Ghosh, S.; Acharyya, S. S.; Sasaki, T.; Bal, R. Room temperature selective oxidation of aniline to azoxybenzene over a silver supported tungsten oxide nanostructured catalyst. *Green Chem.*, **2015**, *17*, 1867-1876.

(11) Baumgar, H.E.; Stalk, A.; Miller, E.M. Reactions of Amines. XIII. The Oxidation of N-Acyl-N-arylhydroxylamines with Lead Tetraacetate1,2. *J. Org. Chem.*, **1965**, *30*, 1203-1206.

(12) Waghmode, S. B.; Sabne, S. M.; Sivasanker, S. Liquid phase oxidation of amines to azoxy compounds over ETS-10 molecular sieves. *Green Chem.*, **2001**, *3*, 285-288.

(13) Tuel, A.; Hubert-Pfalzgraf, L. G. Nanometric monodispersed titanium oxide particles on mesoporous silica: synthesis, characterization, and catalytic activity in oxidation reactions in the liquid phase. *J.Cat.* **2003***, 217*, 343-353.

(14) Liu, Y.; Liu, B.; Guo, A.; Dong, Z.; Jin, S.; Lu, Y. Reduction of Nitroarenes to Azoxybenzenes by NaOH-PEG 400. *Synthetic Commun* , **2012**, *42*, 2201-2206.

(15) Cantillo, D.; Moghaddam, M.M.; Kappe, C.O. Hydrazine-mediated Reduction of Nitro and Azide Functionalities Catalyzed by Highly Active and Reusable Magnetic Iron Oxide Nanocrystals. *J. Org. Chem.* **2013**, *78*, 4530-4542.

(16) Zhao, B.; Liu, P.; Zhuang, H.; Jiao, Z.; Fang, T.; Xu, W.; Lu, B.; Jiang, Y. Hierarchical self-assembly of microscale leaf-like CuO on graphene sheets for high-performance electrochemical capacitors. *J. Mater. Chem. A* , **2013**, *1*, 367-373.

(17) Paek, S-M.; Yoo, E.; Honma, I. Enhanced Photothermal Effect of Plasmonic Nanoparticles Coated with Reduced Graphene Oxide. *Nano Lett.*, **2008**, *9,* 4071-4075.

(18) Zhao, B.; Zhang, G.; Song, J.; Jiang, Y.; Zhuang, H.; Liu, P.; Fang, T. Bivalent tin ion assisted reduction for preparing graphene/SnO_2 composite with good cyclic performance and lithium storage capacity. *Electrochimica Acta* , **2011**, *56*, 7340-7346.

(19) Mai, Y. J.; Tu, J. P.; Gu, C. D.; Wang, X. L. Graphene anchored with nickel nanoparticles as a high-performance anode material for lithium ion batteries. *J. Power Sources* **2012***, 209*, 1-6.

(20) Zhu, J.; Zhu, T.; Zhou, X.; Zhang, Y.; Lou, X. W.; Chen, X.; Zhang, H.; Hng, H. H.; Yan, Q. Facile synthesis of metal oxide/reduced graphene oxide hybrids

with high lithium storage capacity and stable cyclability. *Nanoscale* , **2011**, *3*, 1084-1089.

(21) Stankovich, S.; Dikin, D. A.; Piner, R. D.; Kohlhaas, K. A.; Kleinhammes, A.; Jia, Y.; Wu, Y.; Nguyen, S. T.; Ruoff, R. S. Synthesis of graphene-based nanosheets via chemical reduction of exfoliated graphite oxide. *Carbon* **2007***, 45*, 1558-1565.

(22) Menini, L.; Pereira, M.C.; Ferreira, A.C.; Fabris, J.D.; Gusevskaya, E.V. Cobalt-iron magnetic composites as heterogeneous catalysts for the aerobic oxidation of thiols under alkali free conditions. *Applied Catalysis A: General* , **2011**, *392*,151-157.

(23) Jacinto, M.J.; Santos, O.H.C.F.; Jardim, R.F.; Landers, R.; Rossi, L.M. Preparation of recoverable Ru catalysts for liquid-phase oxidation and hydrogenation reactions. *Applied Catalysis A: General* , **2009**, *360*,177-182.

APPENDIX I: FUTURE WORK

This appendix present some ideas for future work with layered double hydroxides, mesoporous metal oxides and nanocomposites for sorption processes and heterogeneous catalysis. The use of different procedures such as microwave synthesis, co-precipitation, and hydrothermal methods for the synthesis of metal oxides and nanocomposites with very high surface areas, ultrafine particle sizes, and unique morphologies can be explored.

NiAl layered double hydroxides with different Ni^{2+}/Al^{3+} ratios can be synthesized with microwave and hydrothermal synthesis procedures at different temperatures. They can be applied as efficient sorbents for the removal of textiles dyes with diverse properties (e.g : anionic, cationic and nonionic dyes). The catalytic activity of NiAl and CuAl mixed oxides can be examined in other industrially important organic transformations such as Aldol condensation, lactone synthesis, oxime formation and Baeyer- Villiger oxidation. Noble metal catalyzed carbon-carbon coupling reactions of aryl halides, such as Suzuki–Miyaura and Ullmann reactions, are very important as versatile routes to constructing biaryl units in organic synthesis. These structures are found in a variety of compounds of interest in the agrochemical and pharmaceutical industry and many efforts continue to pay on the development of new dibenzyl structures. The catalytic activity of Ni/Graphene composite discussed in Chapter 4 can be tested in these coupling reactions to replace existing costly metal catalysts (e.g: Au and Pd).

APPENDIX II: PATENTS

1. **Pahalagedara, M. N.**; Dharmarathna, S.; Pahalagedara, L. R.; Suib, S. L. Adsorptive Desulfurization Method. United States Patent and Trademark Office, US Patent Application 65/077,535. Patent Pending, Nov. 2014

APPENDIX III: PUBLICATIONS

1. **Pahalagedara, M.N.;** Pahalagedara, L. R.; Kuo, C-H.; Dharmarathna, S.; Suib, S. L. Ordered Mesoporous Mixed Metal Oxides: Remarkable Effect of Pore Size on Catalytic Activity. *Langmuir* **2014**, *30*, 8228-8237.

2. **Pahalagedara, M.N.**; Samaraweera, M.; Dharmarathna, S.; Kuo, C-H.; Pahalagedara, L. R.; Gascon. J.; Suib, S. L. Removal of Azo Dyes: Intercalation into Sonochemically Synthesized NiAl Layered Double Hydroxide. *J. Phys. Chem. C*, **2014**, *118* (31), 17801–17809.

3. Pahalagedara, L. R.; Dharmarathna, S.; King'ondu.; C. K.; **Pahalagedara, M. N.;** Meng, Y.; Kuo, C-H.; Suib, S. L. Microwave-Assisted Hydrothermal Synthesis of α-MnO_2: Lattice Expansion via Rapid Temperature Ramping and Framework Substitution. *J. Phys. Chem. C* **2014**, *118* (35), 20363–20373.

4. Pahalagedara, L. R.; Poyraz, A. S.; Song, W.; Kuo, C-H.; **Pahalagedara, M. N.**; Meng, Y.; Suib, S. L. Low temperature Desulfurization of H_2S: High sorption capacities by mesoporous cobalt oxide via increased H_2S diffusion. *Chem. Mater.* **2014**, *26,* 6613-6621.

5. **Pahalagedara, M.N.**; Pahalagedara, L. R.; Kriz, D.; Chen, S-Y.; Beaulieu, F.; Thalgaspitiya, W.; Suib, S.L. Copper Aluminum Mixed Oxide (CuAl MO) Catalyst: A Green approach for the One-pot Synthesis of Imines under Solvent-free Conditions. (*Submitted to Applied Catalysis B: Environmental)*

6. **Pahalagedara, M.N.**; Pahalagedara, L. R.; He, J.; Miao, R.; Gottlieb, B.; Rathnayake, D.; Suib, S.L. Room Temperature Selective Reduction of Nitrobenzene to Azoxybenzene over Magnetically Separable Urchin-like Ni/Graphene nanocomposites. (*In preparation)*

7. Pahalagedara, L. R.; Dharmarathna, S.; Wasalathanthri, N.; **Pahalagedara, M. N.;** Kuo, C-H.; Garces, F.; Suib, S. L. Low temperature diesel soot oxidation by Pt and Co doped manganese oxide octahedral molecular sieves. (*In preparation)*

APPENDIX IV: PRESENTATIONS

1. **Pahalagedara, M. N.**; Pahalagedara, L. R.; Dharmarathna, S.; Kuo, C-H.; Suib, S. L. Ca-Al layered double hydroxides (LDH) as a potential sorbent for fuel desulfurization: Application to the removal of dibenzothiophene, 248th ACS National Meeting & Exposition, San Francisco, CA, August 10-14, 2014.

2. Pahalagedara, L. R.; Dharmarathna, S.; King'ondu.; C. K.; **Pahalagedara, M. N.**; Meng, Y.; Kuo, C-H.; Suib, S. L. α-MnO_2 lattice expansion by rapid temperature ramping: A case of Jahn-Teller distortion, 248th ACS National Meeting & Exposition, San Francisco, CA, August 10-14, 2014.

3. **Pahalagedara, M. N.**; Pahalagedara, L. R.; Dharmarathna, S.; Kuo, C-H.; Suib, S. L. Sonochemical synthesis of Ni-Al layered double hydroxides (LDH): Increased adsorptive capacity on dye removal, R.T.Major poster session, University of Connecticut, Storrs, CT, October, 2012.

APPENDIX V

Title:	Ordered Mesoporous Mixed Metal Oxides: Remarkable Effect of Pore Size on Catalytic Activity
Author:	Madhavi N. Pahalagedara, Lakshitha R. Pahalagedara, Chung-Hao Kuo, et al
Publication:	Langmuir
Publisher:	American Chemical Society
Date:	Jul 1, 2014

PERMISSION/LICENSE IS GRANTED FOR YOUR ORDER AT NO CHARGE

This type of permission/license, instead of the standard Terms & Conditions, is sent to you because no fee is being charged for your order. Please note the following:

- Permission is granted for your request in both print and electronic formats, and translations.
- If figures and/or tables were requested, they may be adapted or used in part.
- Please print this page for your records and send a copy of it to your publisher/graduate school.
- Appropriate credit for the requested material should be given as follows: "Reprinted with permission from *Langmuir* **2014**, *30*(27), 8228-8237. Copyright 2014 American Chemical Society."
- One-time permission is granted only for the use specified in your request. No additional uses are granted (such as derivative works or other editions). For any other uses, please submit a new request.